

Design optimization of the KATRIN transport section and investigation of related background contribution

Master's Thesis of

Rodolphe COMBE

at the Department of Physics
Institute for Experimental Nuclear Physics

| | |
|------------------|---------------------------|
| Reviewer: | Prof. Dr. Guido Drexlin |
| Second reviewer: | Prof. Dr. Ulrich Husemann |
| Advisor: | Dr. Kathrin Valerius |
| Second advisor: | Daniel Hilke |

14th March 2014 – 13th March 2015

Fakultät für Physik
Universität Karlsruhe (TH)
Wolfgang-Gaede-Str. 1
76131 Karlsruhe

Abstract

The KARlsruhe TRItium Neutrino (KATRIN) experiment aims to measure the mass of the electron anti-neutrino with a sensitivity of 200 meV. To achieve this goal, the background must be kept as low as possible. The components of KATRIN can be subdivided into two sections: the Source and Transport Section (STS) and the Spectrometer and Detector Section (SDS). In the context of this master's thesis, the investigation of the background induced by tritium ions inside the differential pumping section (DPS), as part of the STS, has been carried out by detailed simulations. Furthermore, flux tube margins have been computed and evaluated for two STS components, DPS and CPS (Cryogenic Pumping Section). The thesis starts with a brief introduction about neutrino physics (Ch. 1) and the KATRIN experiment (Ch. 2), and afterwards describes the steps of the calculation, the modeling of the simulation geometry (Ch. 3), the calculation of the electromagnetic fields (Ch. 4) and of the margin between the magnetic flux tube and the beamtube (Ch. 5), to finally unveil the result of the calculation of the reduction factor and of the residence time of tritium ions in the transport section of the KATRIN experiment (Ch. 6). Actually, every tritium ion that has not been eliminated by the end of the CPS will be able to create secondary electrons by ionization or would be able to decay further downstream in the experiment, and this may create background. If these ions cannot be removed fast enough, there is a significant risk that they will create space charges. These space charges within the DPS may modify the effective analysis potential, and hence influence the neutrino mass measurement.

Das KARlsruhe TRItium Neutrino (KATRIN) Experiment hat das Ziel, die Masse des Elektron-Antineutrinos mit einer Genauigkeit von 200 meV zu messen. Um dieses Ziel zu erreichen muss der Untergrund so niedrig wie möglich sein. Das KATRIN Experiment kann in zwei Abschnitte unterteilt werden: die Quelle- und Transportstrecke (STS) und die Spektrometer- und Detektorstrecke (SDS). Im Rahmen dieser Masterarbeit wird die Untersuchung des Tritium-induzierten Untergrunds in der differentiellen Pumpstrecke (DPS), als Teil der STS, durch detaillierte Simulationen durchgeführt. Außerdem werden Flussschlauchabstände für zwei der STS Komponenten, der DPS und der kryogenen Pumpstrecke (CPS), berechnet und bewertet. Die Arbeit fängt mit einer kurzen Einleitung in die Neutrinophysik (Kap. 1) und das KATRIN Experiment (Kap. 2) an. Danach folgt die schrittweise Beschreibung der Grundlagen der Simulation, dem Entwerfen der Geometrie (Kap. 3), der Berechnung des elektromagnetischen Feldes (Kap. 4) und des Abstands zwischen dem Flussschlauch und dem Strahlrohr (Kap. 5), um das Ergebnis der Berechnung des Reduktionsfaktors und der Verweilzeit der Tritiumionen in der Transportstrecke des KATRIN Experiments (Kap. 6) zu erhalten. Jedes Tritiumion, das nach der DPS im aktiven Volumen verbleibt, kann Sekundärelektronen durch Ionisation induzieren oder gleich durch Zerfall Untergrund erzeugen. Wenn diese Ionen nicht schnell genug eliminiert werden, können sie zudem Raumladungen induzieren, die das effektive Analysepotential modifizieren, und so die Messung der Neutrinomasse beeinträchtigen.

L'expérience KARlsruhe TRItium Neutrino (KATRIN) a pour but de mesurer la masse de l'antineutrino électronique avec une sensibilité de 200 meV. Dans ce but, le bruit de fond se doit d'être gardé au plus bas niveau possible. Les composants de KATRIN peuvent être subdivisés en deux parties : la Section Source et Transport (STS) et la Section Spectromètre et Détecteur (SDS). Dans le cadre de ce mémoire de master, la détermination du bruit de fond induit par les ions tritium à l'intérieur de la Section de Pompage Différentiel (DPS), en tant que partie de la STS, a été effectuée à l'aide de simulations détaillées. De plus, la marge des tubes de flux a été calculée et évaluée pour deux éléments de la STS que sont le DPS et le CPS (Section de Pompage Cryogénique). La thèse débute par une brève introduction à la physique des neutrinos (Ch. 1) et à l'expérience KATRIN (Ch. 2), par la suite décrit les étapes du calcul, la modélisation de la géométrie de la simulation (Ch. 3), le calcul des champs électromagnétiques (Ch. 4) et de la marge entre le tube de flux magnétique et le tube à faisceaux (Ch. 5), pour finalement dévoiler le résultat du calcul du facteur de réduction et du temps de persistance des ions tritium dans la section de transport de l'expérience KATRIN (Ch. 6). En effet, tout ion tritium qui n'aura pas été éliminé avant le bout du CPS pourra par la suite induire la production d'électrons secondaires par ionisation ou se désintégrer plus loin en aval de l'expérience, et serai donc une source de bruit de fond non négligeable. Si ces ions ne peuvent être supprimés assez rapidement, il existe aussi un risque significatif de création de charges d'espace. Ces charges d'espace à l'intérieur du DPS pourraient modifier le potentiel effectif d'analyse, et ainsi influencer la mesure de la masse du neutrino.

Contents

| | |
|---|-----------|
| 1. Introduction to Neutrino Physics | 1 |
| 1.1. Discovery | 1 |
| 1.2. Neutrino oscillations | 4 |
| 1.3. Neutrino mass | 5 |
| 2. The Karlsruhe Tritium Neutrino Experiment (KATRIN) | 9 |
| 2.1. Direct Measurement of the Neutrino Mass | 9 |
| 2.2. Experimental Setup | 11 |
| 2.3. The Source and Transport Section (STS) | 12 |
| 2.3.1. The Rear Section | 12 |
| 2.3.2. The Windowless Gaseous Tritium Source (WGTS) | 12 |
| 2.3.3. The Transport Section: DPS and CPS | 13 |
| 2.4. The Spectrometer and Detector Section (SDS) | 15 |
| 2.4.1. The Electrostatic Spectrometers | 15 |
| 2.4.2. The Detector | 16 |
| 2.4.3. The Monitor Spectrometer | 18 |
| 3. Implementation of a realistic DPS and CPS geometry in the simulation framework Kasper | 21 |
| 3.1. Modeling of arbitrary geometries with KGeoBag | 21 |
| 3.2. Presentation of the DPS Geometry | 24 |
| 3.2.1. The dipole electrodes and the shell surfaces | 26 |
| 3.3. Presentation of the CPS Geometry | 27 |
| 3.3.1. The Beam surface in the CPS geometry | 28 |
| 3.3.2. Cryogenic Temperature and Shrinking Factor | 30 |
| 4. Computation of Electromagnetic Fields in the DPS and CPS | 33 |
| 4.1. Computation of Electromagnetic Fields with KEMField | 33 |
| 4.1.1. Computation of Potentials with the Boundary Element Method | 33 |
| 4.1.2. The Robin Hood Algorithm for Charge Density Calculation | 35 |
| 4.1.3. Comparison between the Direct and the FFTM Field Solver | 37 |
| 4.1.4. Computation of Magnetic Fields with the Zonal Harmonic Expansion | 40 |
| 4.2. Electromagnetic Fields within the DPS | 43 |
| 4.2.1. Non-axial Electric Fields | 44 |
| 4.2.2. Magnetic Field | 44 |
| 4.3. Magnetic Field computation within the CPS | 46 |

| | |
|--|---------------|
| 5. Evaluation of flux tube margins in the CPS/DPS beamtubes | 49 |
| 5.1. Distance Testing and Margin Computation with Kassiopeia | 49 |
| 5.2. Approximations Used for the Distance Measurement in the DPS/CPS . . | 50 |
| 5.3. Margins for the DPS/CPS | 51 |
| 5.3.1. Margin for the DPS | 51 |
| 5.3.2. Margin for the CPS | 51 |
| 6. Reduction Factor of the Tritium Ions in the DPS | 55 |
| 6.1. Tracking of Ions with Kassiopeia | 55 |
| 6.2. Energy Spectrum of the Ions in the KATRIN Experiment | 62 |
| 6.3. Reduction Factor and Time of Elimination | 64 |
| 7. Summary and outlook | 67 |
| Appendix | 68 |
| A. The DPS Geometry | 71 |
| B. The CPS Geometry | 85 |
| C. Electromagnetic configuration | 107 |

1. Introduction to Neutrino Physics

1.1. Discovery

Postulation

Neutrinos are extremely light particles that form the second most abundant particle species in the universe after photons with a density of $\approx 340 \text{ cm}^{-3}$. As they interact only through the weak force, it is incredibly difficult to detect them and to measure their properties. Because of this, eighty years after they were postulated, amazingly few of their properties are known. They were first postulated by Wolfgang Pauli to explain how beta decay could conserve four-momentum. For this purpose, he imagined a particle he called *neutron*. Pauli supposed this particle to have the adequate properties to match the experimental data. To conserve electric charge, spin statistics and take into account its obvious low interacting ability, the particle had to be neutral, have negligible mass, and spin 1/2. In 1933-34, in analogy to quantum electrodynamics on which he wrote an encyclopedic review article two years earlier, Fermi postulated the existence of the fourth force of nature, later to become known as the weak interaction, which causes a nucleus of A nucleons and atomic number Z to change into its isobar of atomic number $Z+1$ while creating the beta electron and the Pauli neutron he renamed *neutrino*, *the small neutron* in Italian (${}^Z\text{A} \rightarrow {}^{Z+1}\text{A} + \bar{\nu} + e^-$). It was clear that the neutrino experiments needed only this peculiar kind of interaction and ever since the story of the neutrino overlaps with that of the weak interaction. The coupling constant of the interaction became known as the Fermi constant, G_F . Fermi's paper [Fer34] unified Pauli's neutrino with Paul Dirac's positron and Werner Heisenberg's neutron-proton model and gave a solid theoretical basis for future experimental work. In the same year, Bethe and Peierls estimated that the cross section for the neutrino to induce nuclear processes, e.g. to induce the reaction named the *inverse β -decay* ($\bar{\nu} + p \rightarrow e^+ + n$), should be so small that its mean free path in solid matter would be of the order of tens of light-years [BP34]. One year later, in 1935, Yukawa reduced all the elementary interactions to the exchange of virtual bosons, including the idea that even the Fermi point interaction might actually be realized by the exchange of an extremely heavy intermediate vector boson, which would manifest itself only at energies higher than the boson mass [Yuk35]. In 1937, Majorana elaborated a symmetrical theory of weak interaction, where the genuinely neutral neutrino, with no quantum numbers to conjugate, is indistinguishable from its anti-particle [Maj37]. It is still not clear whether the Standard Model (SM) is right in preferring the *Dirac neutrino*, which is genuinely different from its anti-particle, to the Majorana neutrino. In 1942, Fermi invented and constructed a nuclear reactor, the most powerful source of low energy electron anti-neutrinos on Earth. State-of-the-art in 1949 allowed Fermi to postulate the first attempt of a weak interaction

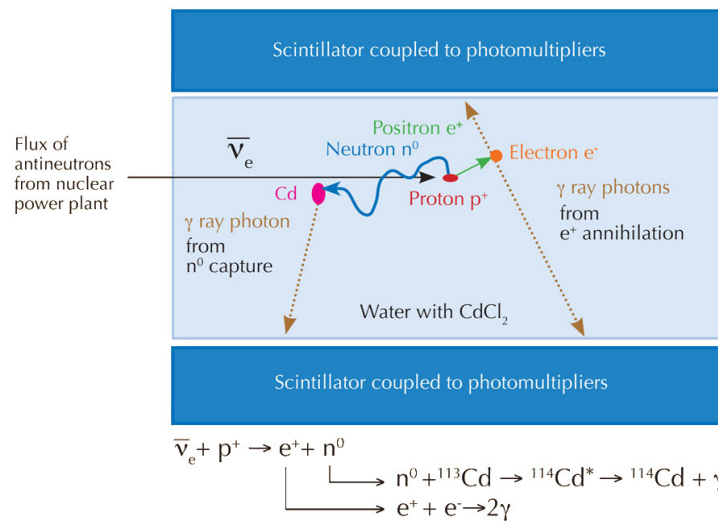


Figure 1.1.: Scheme of the Cowan-Reines experiment that detected an anti-neutrino for the first time [SC11]

theory, unifying the nuclear beta-decay, the muon decay and the capture of the muon by a nucleus as varieties of the same interaction.

In 1952, the half-life of the β -decay of the free neutron was measured [TI53], enabling a reliable estimate of the cross section for the capture of the (anti)neutrino by a proton (inverse β -decay). In 1953, Marx, Zeldovich, and Konopinski and Mahmoud formulated the law of lepton number conservation (the electron lepton number of today) [KM53], which for the first time introduced a clear-cut definition of the neutrino and the anti-neutrino.

First detection

The first experimental confirmation of the existence of an (anti-)neutrino was achieved with the Cowan-Reines experiment [CR+56] (figure 1.1), in 1956, using the capture of anti-neutrinos by protons. This result earned them the Nobel-Prize in 1995. The experiment opened the era of large, high efficiency, electronic detectors in particle physics. Everything seemed neat and the chapter of the neutrino seemed practically closed.

Parity violation

The unsuspected crucial change in our understanding of the weak interaction and the neutrino, which, up to this moment, came mostly from the study of nuclear beta decays, was induced by a problem encountered in the study of elementary particles, now called the $\theta - \tau$ puzzle. In 1956, even before dedicated tests of parity conservation in other weak processes, Lee and Yang, Landau, and Salam developed the so-called two-component theory of the neutrino [LY57], which does not conserve parity. Instead of the four states of the Dirac theory describing the neutrino and anti-neutrino of both helicities, the two-component theory considers only the massless neutrino of one helicity and the anti-neutrino of the opposite helicity as the physical states. This description of the neutrinos is still valid

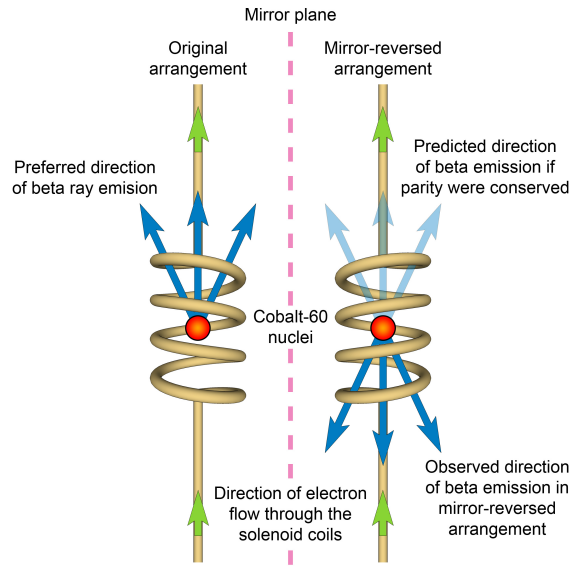


Figure 1.2.: Scheme of the Wu experiment establishing the maximum parity violation of the neutrinos [N13]

in the SM. All the experiments made then found maximum possible violation of parity conservation (figure 1.2). The main result of interest to us from this campaign is that the (electron) neutrinos emitted in all the charge-changing weak processes are invariably of negative helicity (or left-handed), while the anti-neutrinos are right-handed.

Muon neutrino

In 1937, the muon was discovered in cosmic rays [NA37]. In 1948, the electron spectrum from muon decay was found to be continuous in many experiments. It became then obvious that not one but two neutrinos are emitted along with the electron. The two neutrinos were named differently, the *neutrino* and the *neutretto*, but, with the time, the idea seemed to have been forgotten. First success in neutrino physics after the *parity furor* of 1956-58, was the discovery of the second neutrino, the ν_μ . Since then, the muon was being thought to have the same lepton number as the electron, and was thus considered merely a *heavy electron* (or, better still, an excited electron), which should, if the two neutrinos were identical, as well decay into an electron and a photon. If the neutrino which comes with the muon in both the muon and pion decay is indeed different from the one which accompanies the electron in beta decay, it would produce, in neutrino capture reaction, only muons and no electrons. This is exactly what was measured in 1962 by Lederman, Schwartz and Steinberger's experiment [DG+62], which earned them the Nobel Prize in 1988. The second generation of leptons was thus completed and the need for two lepton numbers was demonstrated, one for each family, which would most probably be independently conserved. In 1963, to save the universality of the weak interaction and account for the extremely slow decays of strange particles, Cabibbo introduced the fruitful concept of what is nowadays called the quark flavor mixing by the weak interaction [Cab67].

The electroweak theory

In 1967, a major theoretical breakthrough happened in the form of the Glashow- Weinberg- Salam unified electroweak interaction [Wei67]. After the Fermi theory of β -decay and the non-conservation of parity, this is probably the most important single achievement in our understanding of the weak interaction in general, and of the neutrino in particular. In 1973, muon neutrino reactions with no charge change were observed for the first time in the monstrous *Gargamelle* bubble chamber [Gar74]. They were supposed to be mediated by the Z^0 , the weak neutral intermediate boson of the electroweak theory, whose mass and coupling to the weak neutral currents are determined by the value of the Weinberg mixing angle. The electroweak theory was, with the result of this measurement, fully established and it only remained to discover the free intermediate bosons at the masses predicted by the value of the mixing angle. In 1975, comparisons of electron and neutrino scattering on nucleons, as well as the study of structure functions in neutrino and anti-neutrino scattering on nucleons, yielded quark electric charges.

Tau neutrino

In this era of eruptive proliferation of elementary particles, the search for a lepton heavier than the muon was only to be expected, though nothing in theory pointed to its existence. Until 1975, it was not found up to a mass of about 1 GeV, which, assuming weak interaction universality, by direct scaling of the muon half-life for the phase space factor, left no hope that it could be directly observed. The search in high energy electron-positron collisions, in which creation of the lepton-antilepton pair was expected, was thus based on the search for its assumed decay products, the lighter leptons. At the threshold energy of 3.56 GeV, the simultaneous occurrence of an electron and a muon started signaling the creation of a tau-antitau pair. This discovery immediately implied the existence of the third generation of fundamental particles, of the corresponding neutrino in the first place, as well as of the third quark doublet; the completion of which took another 25 years of hard work, the tau neutrino being observed last, in the year 2000.

1.2. Neutrino oscillations

The SM predicts three massless neutrinos. In 1938 Bethe formulated his theory of stellar thermonuclear synthesis [Bet39], based on the weak reaction:

$$p + p \rightarrow d + e^+ + \nu \quad (1.1)$$

This reaction describes the main source of solar neutrinos. In 1969, the electron neutrino was conclusively detected for the first time in an experiment on solar neutrinos. This experiment marks the beginning of the new field of physics, or of the neutrino physics - the neutrino astrophysics. The predicted reaction rates vary from 6 to 8 SNU (1 SNU is equal to the neutrino flux producing 10^{-36} captures per target atom per second), while the average measured rate, after some 30 years of measurement, still equals only 2.5 SNU, with an error of 10%. This constitutes the famous solar neutrino problem.

Fortunately, the year before had been developed by Pontecorvo [Pon68], starting from the work of Maki, Nakagawa, and Sakata in 1962 [MNS62], a theory claiming that, if neutrino had mass, they could oscillate between flavors. With this theory, the lack of electron neutrinos was explained by them oscillating to other neutrinos flavors. In the analogous case of quark mixing via the CKM matrix, the smallness of the off-diagonal terms (small mixing angles) permits a *dominant eigenstate* approximation. However, the results of neutrino oscillation searches show that the mixing matrix contains two large mixing angles and a third angle that is not exceedingly small. Neutrinos are produced in weak decays with a definite lepton flavor, and are typically detected by the charged current weak interaction again associated with a specific lepton flavor. Hence, the neutrino masses are separated into the three associated charged lepton categories. Most of the observables, in particular mass-squared, cannot distinguish between Dirac and Majorana neutrinos, and are unaffected by CP phases. So far solar, reactor, atmospheric and accelerator neutrino oscillation experiments can be consistently described using three active neutrino flavors, i.e. two mass splittings and three mixing angles. The results of many experiments developed since then supported the theory [T2K13].

1.3. Neutrino mass

On one hand, observation of neutrino oscillations implies neutrinos must have a non-zero rest mass, on the other hand, neutrino oscillation experiments do not tell us the absolute mass scale. As former experiments have not been able to measure the mass, we can expect to find that neutrinos have a pretty small mass.

Theory

In principle, the SM could be enhanced by introducing right-handed neutrinos and Yukawa couplings for the neutrino as well, but then the pattern of observed masses and mixings is even more obscure as the masses of the neutrinos are at least six orders of magnitude smaller than the masses of the charged fermions. Therefore, the experimental evidence for neutrino masses and mixing is seen as the first clear indication for physics beyond the SM. There are many theories beyond the SM which explore the origins of neutrino masses and mixings. In these theories, which often work within the framework of Supersymmetry, neutrinos naturally acquire mass. A large group of models makes use of the so-called see-saw effect to generate neutrino masses. Other classes of theories are based on completely different potential origins of neutrino masses. Interestingly, some of these models predict that the masses of the three different neutrino types should all be nearly the same. Other models predict that the observed mass variation between the non-neutrino members of the families is also present for the neutrinos, i.e. the neutrino eigenstates differ significantly in mass. Recently, it has been pointed out that the absolute mass scale of neutrinos may be even more significant and straightforward for the fundamental theory of fermion masses than the determination of the neutrino mixing angles and CP-violating phases. It will most probably be the absolute mass scale of neutrinos which will determine the scale of new physics.

Cosmology

Neutrinos and their properties also play an important role in astrophysics and cosmology. As there are about 1 billion times more neutrinos than baryons predicted to be left over from the Big Bang. These relic neutrinos could play an important role as neutrino hot dark matter (ν HDM) in the evolution of large scale structures (LSS). The imprint of ν HDM on LSS evolution is quite distinct from other dark matter candidates such as supersymmetric particles, which act as non-relativistic or Cold Dark Matter (CDM). Cosmological models of structure formation strongly depend on the relative amounts of CDM and ν HDM in the universe; hence a determination of the neutrino contribution Ω_ν to the total dark matter content Ω_{DM} of the universe is important for our understanding of structure formation. Constraint on the sum of the neutrino masses can be obtained from the analysis of the cosmic microwave background anisotropy, combined with the galaxy redshift surveys and other data. The last results from Planck and Galaxy clustering data give a sum of the neutrino mass $\sum m_\nu < 0.39$ eV at 95% C.L. [GdP+13].

Supernova

The spread of arrival times of the neutrinos from SN1987A, coupled with the measured neutrino energies, provided a time-of-flight limit on a quantity similar to $\langle m_\beta \rangle \equiv \sqrt{\langle m_\beta^2 \rangle}$. The resulting limits, however, are no longer competitive with the limits from tritium beta decay. The last results from the SN1987A data collected by Kamiokande-II, IMB and Baksan give a neutrino mass $m_\nu < 5.8$ eV at 95% CL [PRV10].

Neutrinoless double β -decay

Direct information on neutrino masses can also be obtained from neutrinoless double beta decay ($0\nu\beta\beta$) searches. Neutrinoless double-beta decay would signal violation of total lepton number conservation. If the neutrino is a Dirac particle, the ν_e field annihilates a neutrino state and creates an anti-neutrino state which are different. On the contrary, if ν_e is a Majorana particle, neutrino and anti-neutrino are the same state. Thus, in order to induce the $0\nu\beta\beta$ decay, ν_e must be a Majorana particle. The inverse also holds: if $0\nu\beta\beta$ decay is observed, neutrinos must be massive Majorana particles. In general, in models beyond the SM, there may be other sources of total lepton number violation which can induce $0\nu\beta\beta$ decay. As long as only a limit on the half-life of the decaying isotope is available, limits on the effective Majorana neutrino mass, on the lepton-number violating right-handed current or other possible mechanisms mediating $0\nu\beta\beta$ decay can be obtained, independently of the actual mechanism. There is tension between a claim by pairs of the Heidelberg-Moscow collaboration and several recent experiments which did not find evidence for $0\nu\beta\beta$ decay. Besides a dependence on the phase space and the nuclear matrix element, the observable $0\nu\beta\beta$ decay rate is proportional to the square of the effective Majorana mass $\langle m_{\beta\beta} \rangle$. Nuclear structure calculations are needed to deduce $\langle m_{\beta\beta} \rangle$ from the decay rate. Comparing different nuclear model evaluations indicates a factor ~ 2 - 3 spread in the calculated nuclear matrix elements. Given the present knowledge of the neutrino oscillation parameters, one can derive the relation between the effective

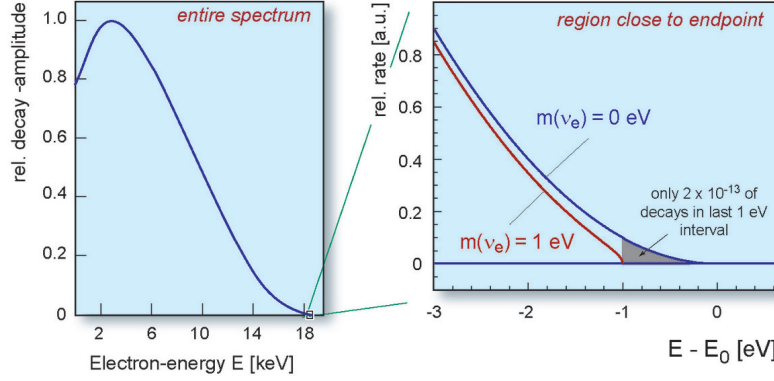


Figure 1.3.: Tritium Beta decay and neutrino mass [KAT05]

Majorana mass and the mass of the lightest neutrino. If the neutrinoless double-beta decay is observed, it will be possible to fix a range of absolute values of the masses m_{ν_i} . Unlike the direct neutrino mass measurements, however, a limit on $\langle m_{\beta\beta} \rangle$ does not allow to constrain the individual mass values m_{ν_i} even when the mass differences Δm^2 are known. The latest range for the upper limit on the effective electron neutrino mass $m_{\beta\beta}$ is 0.2 - 0.4 eV [GER13].

β -decay

The most sensitive neutrino mass measurement to date, involving electron-type anti-neutrinos, is based on fitting the shape of the beta spectrum near its kinematic endpoint (see 2.1). The analysis of the low-energy beta decay of tritium, combined with the oscillation results, limits all active neutrino masses. The last values given by the Troitsk experiment [Tro11] are a squared mass of $m_\nu^2 = -0.67 \pm 2.53 \text{ eV}^2$ and an upper sensitivity limit of $m_\nu < 2.2 \text{ eV}$, 95 % C.L.. The Mainz experiment gave $m_{\nu_e}^2 = -0.6 \pm 2.2_{\text{stat}} \pm 2.1_{\text{sys}} \text{ eV}^2$ and $m_{\nu_e} < 2.3 \text{ eV}$ at 95% C.L. [Mai05].

The measurement principle to derive the neutrino mass is the high precision measurement of the kinetic energy of beta electrons issued from the tritium beta decay: in the beta decay of tritium to helium, an electron and anti-neutrino are created. They share together the remaining transition energy, which is distributed to their kinetic energies and the rest mass of the electron and the neutrino. The subtle effect of the neutrino rest mass to the kinetic energy of the electron is larger when the neutrino is non-relativistic, i.e. at the endpoint of the electron energy spectrum (figure 1.3). Therefore, a precise measurement of the electron energy very close to its endpoint gives information on the neutrino mass.

In principle, every beta decaying isotope could be used. However, tritium is the premium candidate for this experiment: due to the very low endpoint energy of tritium decay, the effect of a massive neutrino on the electrons kinetic energy is more significant. Furthermore, tritium has a simple nuclear structure with one proton and two neutrons. It means no nuclear-energy-dependent corrections need to be applied to the beta spectrum. Finally, tritium has a suitable half-life of 12.3 years. This is the right range with regard

to the required amount of tritium and its activity (for KATRIN, 40 g throughput per day corresponding to a 1.7×10^{11} Bq activity).

2. The Karlsruhe Tritium Neutrino Experiment (KATRIN)

KATRIN is a next-generation tritium β -decay experiment which will improve the sensitivity of the measurement of the neutrino mass compared to the direct neutrino mass measurement experiments at Mainz and Troitsk, by one order of magnitude. With an estimated ν -mass sensitivity of 0.2 eV (90 % C.L.), KATRIN will allow the investigation of the sub-eV neutrino mass scale, which is of particular interest for particle physics, astrophysics and cosmology. In contrast to other methods such as the search for neutrinoless double beta decay ($0\nu\beta\beta$) or cosmological ν - mass studies using large scale structure (LSS) and cosmic microwave background radiation (CMBR) data, KATRIN will provide a completely model-independent measurement of the ν -mass. The KATRIN result will be based only on kinematic relations and energy momentum conservation. For these reasons, it will complement the other laboratory and cosmological methods to investigate neutrinos masses. The combination and comparison of results from tritium β -decay, $0\nu\beta\beta$ and cosmological studies will be essential for our understanding of the role of neutrinos in our physical world.

KATRIN will measure the neutrino mass via ultrahigh precision measurements of the kinematics of electrons from the beta-decay of tritium molecules. To detect the subtle effects of a massive neutrino on the kinematics of the beta electrons, KATRIN requires, on one hand, the provision of a strong gaseous windowless tritium source with well-known properties and precision control, and on the other hand, a high resolution spectrometer to analyze precisely the energy of the electrons.

2.1. Direct Measurement of the Neutrino Mass

The KATRIN experiment needs to analyze precisely the kinetic energy of the electrons. The high sensitivity of the experiment will be achieved thanks to a special type of spectrometer, called MAC-E-Filter (Magnetic Adiabatic Collimation combined with an Electrostatic Filter). It combines a high luminosity and intrinsic low background with a high energy resolution, all of them essential to measure the neutrino mass at the endpoint region of the beta decay spectrum.

The main features of the MAC-E-Filter are illustrated in figure 2.1(a). Two superconducting magnets produce a magnetic field that will guide the β -electrons, which start from the tritium source on the left, into the forward hemisphere and then around the magnetic field lines in the spectrometer in a cyclotron motion. On their way into the center of the spectrometer, the magnetic field B drops by many orders of magnitude. Therefore, the magnetic gradient force transforms most of the cyclotron energy E_{\perp} into

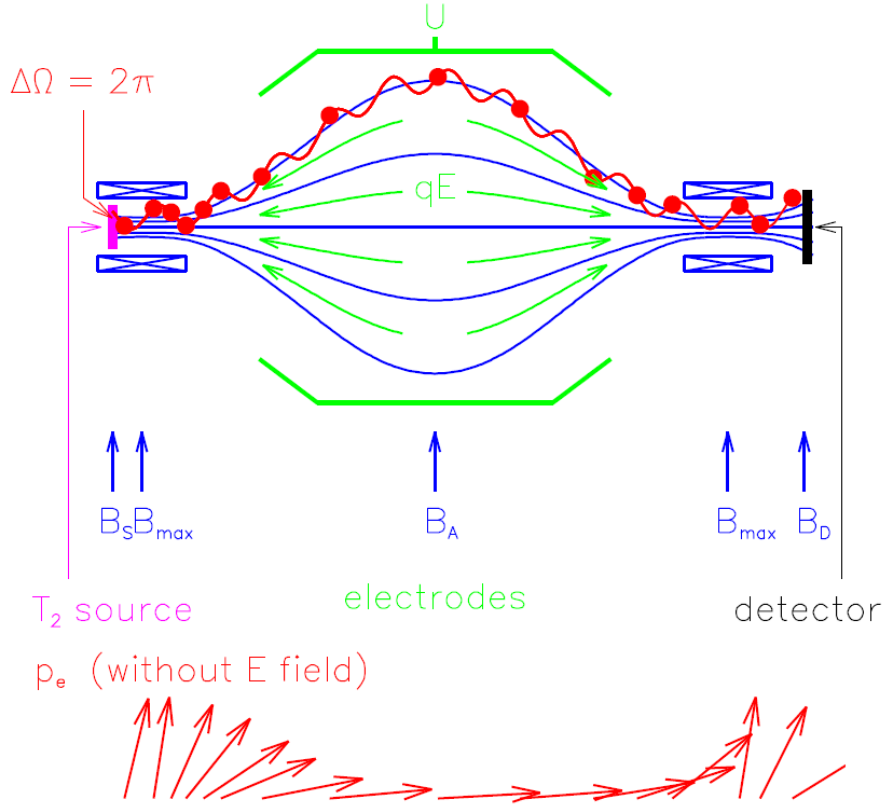


Figure 2.1.: Principle of the MAC-E-Filter [KAT05]. (a) Experimental setup, (b) Momentum transformation due to the adiabatic invariance of the magnetic orbit momentum μ in the inhomogeneous magnetic field.

longitudinal motion. This is illustrated in figure 2.1(b) by a momentum vector. Due to the slowly-varying magnetic field, the momentum transforms adiabatically. Therefore, the magnetic moment μ stays constant:

$$\mu = \frac{E_{\perp}}{B} = \text{const} \quad (2.1)$$

This transformation can be summarized as follows: the β -electrons, isotropically emitted at the source, are transformed into a broad beam of electrons flying almost parallel along the magnetic field lines. This parallel beam of electrons is running against an electrostatic potential formed by a complex wire electrode system. All electrons with enough energy to pass the electrostatic barrier are reaccelerated and collimated onto a detector; all the others are reflected. Therefore, the spectrometer acts as an integrating high-energy pass filter. From eq. (2.1) follows directly, that the relative sharpness $\Delta E/E$ of this filter is given only by the ratio of the minimum magnetic field B_A in the center plane and the maximum magnetic field B_{\max} between the β -electron source and the spectrometer:

$$\frac{\Delta E}{E} = \frac{B_A}{B_{\max}} \quad (2.2)$$

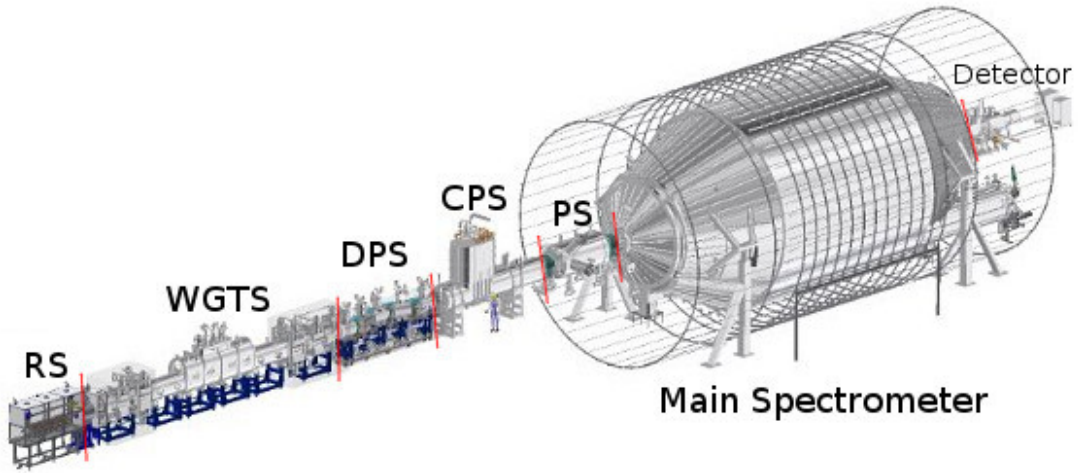


Figure 2.2.: The 70 m long KATRIN reference setup [Int]

Varying the electrostatic retarding potential allows the measurement of the β spectrum in an integrating mode. In order to suppress electrons which have a very long path within the tritium source and therefore exhibit a high scattering probability, the electron source is placed in a magnetic field B_S (see fig. 2.1), which is lower than the maximum magnetic field B_{\max} . This restricts the maximum accepted starting angle of the electrons θ_{\max} by the magnetic mirror effect to :

$$\sin(\theta_{\max}) = \sqrt{\frac{B_S}{B_{\max}}} \quad (2.3)$$

2.2. Experimental Setup

The KATRIN experiment is located on the site of the KIT, Campus North (former FZK (Forschungszentrum Karlsruhe)). The on-site Tritium Laboratory Karlsruhe (TLK), which is the only scientific laboratory equipped with a closed tritium cycle and licensed to handle the required amount of tritium (license: 40 g tritium $\approx 1.5 \times 10^{16}$ Bq), provides an excellent source for KATRIN. A further unique advantage of choosing TLK as host laboratory is the possibility to operate the tritium related parts of KATRIN (and in particular the tritium source) within the existing TLK building, close to the tritium handling facilities. The non-tritium related parts of KATRIN, in particular the electrostatic spectrometers, will be housed in the new buildings at the *green field* site, north of TLK.

The reference setup of KATRIN shown in fig. 2.2 corresponds to a 70 m long linear configuration with about 40 superconducting solenoids, which adiabatically guide β -decay electrons from the source to the detector. The experimental configuration of KATRIN can be grouped into four major functional units:

- a high luminosity Windowless Gaseous Tritium Source (WGTS), delivering 10^{11} β -decay electrons during the standard operation mode of the experiment

- an electron transport and tritium pumping section, comprising an active Differential Pumping Section (DPS) and a passive Cryogenic Pumping Section (CPS)
- a system of two electrostatic retarding filters, with a small pre-spectrometer for pre-filtering and a large main spectrometer, for the energy analysis of β -electrons
- a semi-conductor-based high-resolution low-background detector, to count the β -electrons transmitted through the electrostatic filters

2.3. The Source and Transport Section (STS)

2.3.1. The Rear Section

At the most upstream end of the beam line, a Rear Section will be installed, which consists of a multi-purpose electron gun to measure the overall KATRIN response function (transmission and inelastic scattering) and to investigate systematic effects, as well as of a rear detector to monitor the source activity and a rear plate to control the plasma effects within the source tube.

2.3.2. The Windowless Gaseous Tritium Source (WGTS)

The WGTS will be the β -electron source of KATRIN for the long-term tritium measurements since it offers the highest luminosity and smallest systematic uncertainties. Cold molecular tritium gas ($T = 27\text{ K}$) of high isotopic purity ($> 95\%$) will be injected through a set of capillaries in the middle of the 10 m-long WGTS tube. The gas injection pressure p_{in} allows an adjustment of the column density ρd of the WGTS. For a value of $p_{\text{in}} = 3.4 \times 10^{-3}\text{ mbar}$ and a source tube temperature $T = 27\text{ K}$, the column density of the WGTS is fixed to the reference value $\rho d = 5 \times 10^{17}\text{ molecules/cm}^2$. After injection, the T_2 molecules are transported over a length of 5 m to both tube ends by diffusion. This process leads to a non-linear decrease of the tritium density. At the first pumping port, this parameter is at least a factor of 20 smaller than at the injection point [KAT05]. The transport time of tritium molecules through the WGTS is of the order of 1 s. The decay probability of a single tritium molecule in the WGTS is thus about 10^{-9} . Electrons from the β -decay process are adiabatically guided by the WGTS magnetic field of $B_s = 3.6\text{ T}$ to both ends of the tube. The total β -luminosity is proportional to the area A_s of the WGTS tube. The WGTS will deliver a total (front and rear hemispheres) of $9.5 \times 10^{10}\beta$ -decays per second within the guided magnetic flux of 191 T cm^2 . The main systematic uncertainty of the WGTS is associated with the column density $\rho d = 5 \times 10^{17}\text{ molecules/cm}^2$ which has to be known to a precision of 0.1 % [KAT05]. This requires an appropriate stability of base parameters, such as tube temperature and gas inlet pressure. Technical solutions to meet these demands are the proposed WGTS tube cooling system by means of two-phase neon (with a temperature stability of 30 mK) and a pressure controlled tritium buffer vessel for stabilized tritium injection.

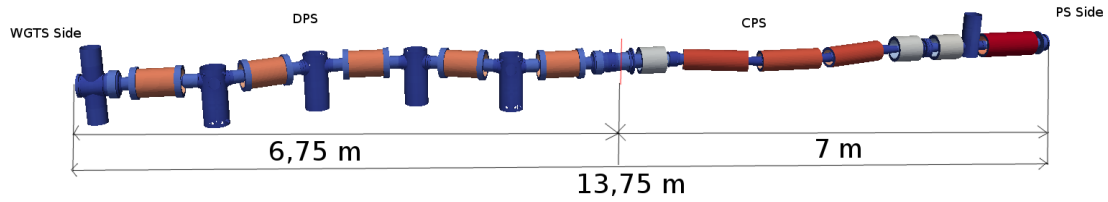


Figure 2.3.: 3D Geometry of the KATRIN Transport Section

2.3.3. The Transport Section: DPS and CPS

The background generated by tritium decay within the spectrometers must be less than 10^{-3} counts/s, which limits the amount of tritium permissible in the main spectrometer to a partial pressure of tritium of about 10^{-20} mbar. This leads to a maximal allowed tritium flow rate into the pre-spectrometer (depending on the detailed design of the vacuum system of the pre-spectrometer and the connecting tube between it and the main spectrometer) of the order of 10^{-14} mbar l/s, the tritium inlet rate being about 2 mbar l/s [KAT05]. This design criterion requires that the tritium flow is suppressed by about a factor of 10^{14} between the outlet of the WGTS tube and the entrance of the pre-spectrometer. This very large suppression factor will be achieved by an effective tritium pumping system based on a combination of differential (DPS, section 2.3.3.1) and cryogenic (CPS, section 2.3.3.2) pumping sections.

2.3.3.1. The Differential Pumping Section

The first part of the tritium flow suppression is based on differential pumping. A series of pumping ports, instrumented with turbomolecular pumps (TMP) with high pumping capacity, reduces the tritium flow both at the rear (DPS1-R) and front sides (DPS1-F, DPS2-F). The DPS2-F element, with four pumping ports, will reduce the tritium flow by more than a factor of 10^5 . The DPS also has to guarantee a stable operation mode of the WGTS. As the DPS elements adjacent to the WGTS (DPS1-F, DPS1-R) contribute in a non-negligible way to the total column density ρd , they have to be operated under (almost) identical parameter values (temperature, magnetic field) as the WGTS. The requirements for stabilization and monitoring of the DPS-1 parameters are however less stringent than for the WGTS.

The DPS2-F is a pumping section consisting of five 1 m-long beamtubes within a superconducting solenoid each. To block the line of sight towards the spectrometer for the diffusing, neutral tritium molecules, two sections are tilted by 20° . Between each section is placed a turbomolecular pump with a nominal pumping speed larger than 2000 l/s. Besides the tritium flow reduction, the beamtubes of the DPS host instrumentation to analyze and reduce the ion flow. Ions, mostly produced by the decay of tritium into positively charged helium, follow the magnetic field and are blind against the pumping measures. Still, the charged tritium is not allowed either to enter the spectrometers, in order to keep background levels for the neutrino mass search sufficiently low. One trick would be to bias the WGTS source and DPS by a little but known negative voltage. This would prevent the positively charged ions or molecules from leaving the source and DPS section. However,

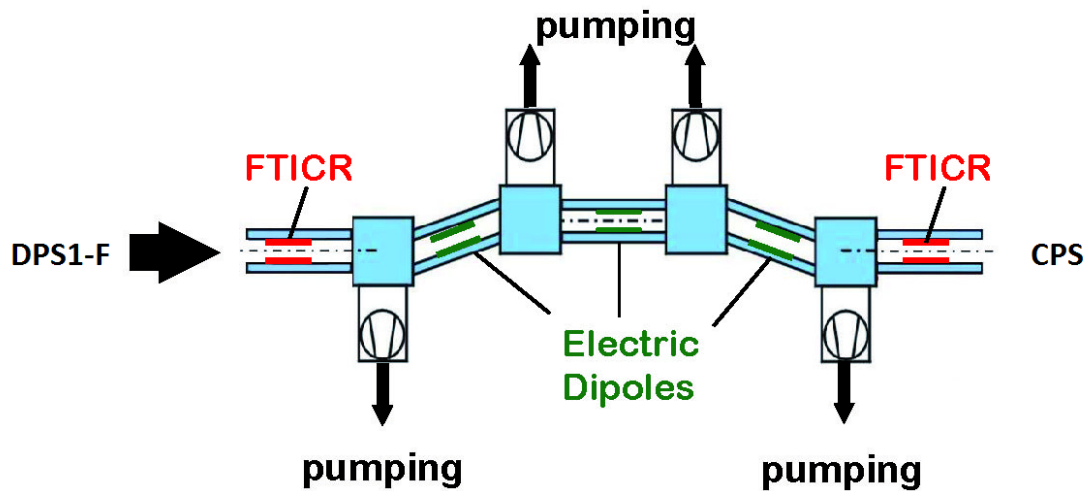


Figure 2.4.: Scheme of the KATRIN Differential Pumping Section [KIT]

one has to get rid of the positive ions that would create space charges, disturbing by the way the measurement of the neutrino mass through shifting the effective potential in the main spectrometer. To actively remove positive ions, the DPS hosts dipole electrodes and Fourier Transformation Ion Cyclotron Resonators, two kinds of instrumentation to analyze the ion species (FTI-CR) and sweep them out of the beamtubes (dipoles), respectively. The DPS cryostat is 6.96 m long and its operating temperature is 77 K. The turbo-pumps are operated at room temperature.

The DPS is composed of the following elements:

- five beamtubes, positioned with a relative angle of 20° in order to prevent a direct line of sight for the tritium molecules between the WGTS and the CPS
- four turbo-molecular pumps in cascade pumping, with six pump ports along the DPS (one between each individual beamtube segment, one at the beginning and one at the end)
- five super-conducting magnets, of a nominal magnetic field of 5.5 T, composed of a main solenoid and two compensation solenoids
- two Fourier Transform-Ion Cyclotron Resonance (FT-ICR) modules, to measure the ion concentrations in the DPS, in the first and last beamtube segments
- three pairs of dipole electrodes, consisting of a half cylinder with a half-cut cone at each end, in order to eliminate the tritium ions, in the three middle beamtube segments

2.3.3.2. The Cryogenic Pumping Section

The differential pumping system will reduce the tritium flow to such a low level that the subsequent passive cryotrapping system CPS will receive a tritium load of less than 1 Ci over a period of 60 days, which is equivalent to a standard tritium run cycle. The beam

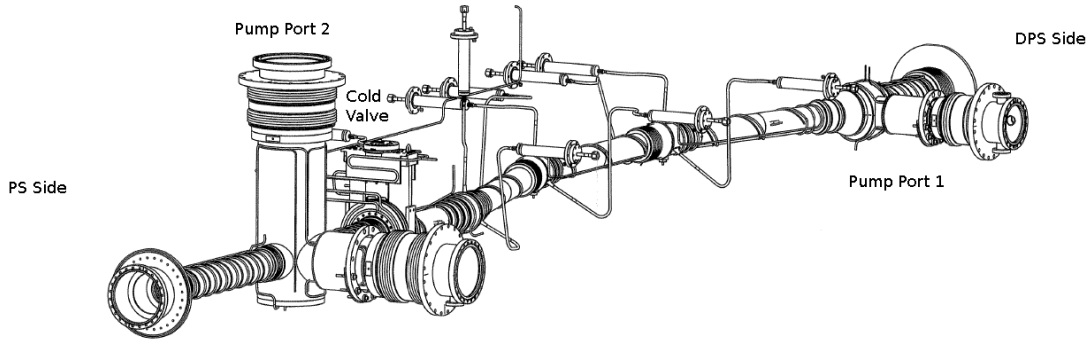


Figure 2.5.: Isometric View of the KATRIN Cryogenic Pumping Section [Int]

tube of the CPS is kept at a temperature of 4.5 K. At this temperature, tritium molecules are passively adsorbed onto the liquid-helium-cold inner tube surfaces.

The cryo-pumping section consists of seven individual transport elements, of again 1 m length and 75 mm diameter, within superconducting coils with a central maximum magnetic field of 5.6 T. The individual tubes are tilted by 15° with respect to each other, thus prohibiting a direct line of sight. In this section, all remaining traces of tritium will be trapped onto the liquid-helium-cold surface of the beamtubes. The tube's surface will be covered with a condensed argon polycrystal layer (snow) to increase the available capture area. The trap will accumulate less than 10^{17} molecules/day, which is negligible in view of its huge capacity. Under normal conditions, its leakage into the pre-spectrometer should be essentially zero according to measurements performed at the Troitsk experiment with such cryo-pumps. Safety valves will protect the system downstream (pre-spectrometer) in case of failure, e.g. a warm-up.

As mentioned above, the tritium flow into the pre-spectrometer should be smaller than 10^{14} mbar l/s. Since the overall reduction factor of the DPS is between 10^7 and $\approx 5 \times 10^7$, the required minimum tritium flow reduction for the CPS is of the order of 10^7 [Jan15].

2.4. The Spectrometer and Detector Section (SDS)

2.4.1. The Electrostatic Spectrometers

The electrons' energies from the WGTS, the krypton quench condensed source and the electron guns will be analyzed by a set of electrostatic retarding spectrometers of the MAC-E filter type. The design of the KATRIN spectrometers is based on a new electromagnetic concept: the retarding high voltage (HV) is directly connected to the hull of the spectrometer vessel itself. A nearly massless inner wire electrode, at slightly more negative potential than the vessel itself, suppresses low-energy electrons emanating from the inner surfaces of the spectrometer walls, representing a potential source of background. In addition, this inner electrode fine-tunes the electrostatic field to avoid the formation of Penning traps in corners, and to optimize the adiabatic transmission properties of the MAC-E filter. The spectrometer section of KATRIN (see fig. 2.6) consists of two electro-

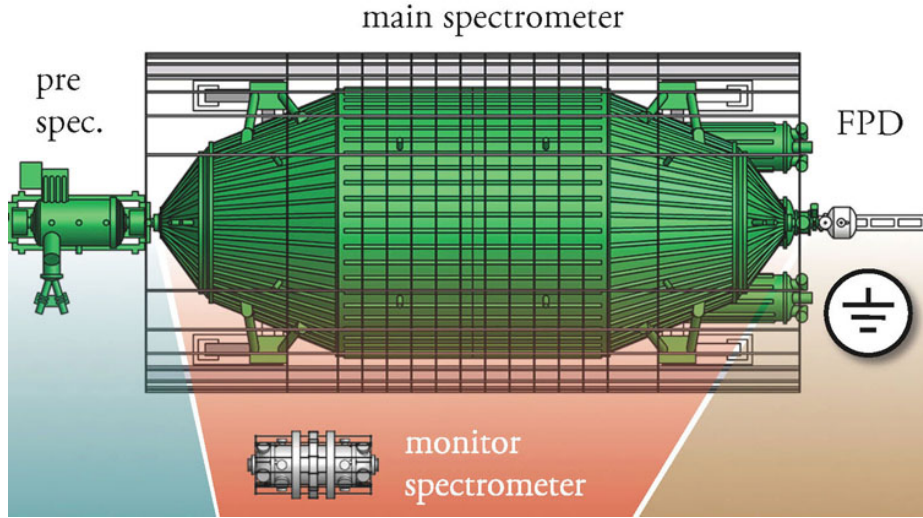


Figure 2.6.: The two electrostatic spectrometers of KATRIN [KIT]

static spectrometers in a *tandem setup*. Electrons have to pass the small pre-spectrometer first, which works at a fixed retarding potential, acting as a pre-filter. In the experiment's normal tritium mode, it will reject low-energy electrons below 18.3 keV, which do not carry any information on the neutrino mass. The remaining electrons enter the second, much larger spectrometer, where the energy spectrum close to the β -decay endpoint is scanned with an energy resolution of 0.93 eV. The advantage of this tandem setup is the reduction of the total flux of electrons from the tritium source into the pre-spectrometer by a factor of 10^6 . This will minimize the background from ionization of residual gas molecules in the main spectrometer. In addition, the pre-spectrometer has served as a test facility to validate the extreme high vacuum (XHV) and electro-magnetic design concepts for the large main spectrometer. In particular, the requirement to reach and to maintain XHV conditions with a pressure smaller than 10^{-11} mbar in both spectrometers constitute a major technological challenge for the KATRIN project.

2.4.2. The Detector

Downstream of the main spectrometer (figure 2.7) is placed within a detector solenoid which leaves enough room for an active and passive detector shielding to lower the detector background rate. The detector is a multi-pixel silicon semiconductor detector with ultra-high energy resolution and very thin entrance window. More information about the detector can be found in [Sch14] and [KAT14].

Those β -electrons, passing the retarding potential of the main spectrometer, are re-accelerated to their initial energy and magnetically guided to the Focal Plane Detector (FPD). The FPD is located inside the second magnet of a pair of superconducting magnets. To lower the detector background rate, the large-diameter warm bore of this solenoid magnet is wide enough to accommodate active and passive detector shielding. The detector is a multi-pixel silicon semiconductor detector with high energy resolution and thin entrance window.

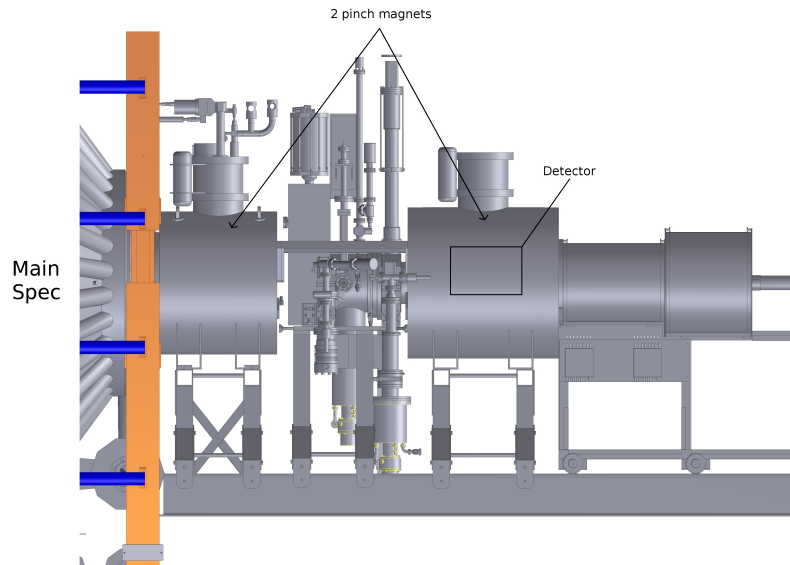


Figure 2.7.: The KATRIN Detector region [Int]

In principle, KATRIN would only require a simple electron counter to determine how many electrons have crossed the retarding potential. In practice, energy, spatial, and temporal information is very important in both understanding the operation of the apparatus and sources of background. The two main reasons we need more information than just counting of the electrons are:

- The electric potentials [e.g. at the source and at the analyzing plane of the main spectrometer] vary slightly depending on the radial position. These distortions can be calculated or measured. The position of the electron as it passes the analyzing plane is imaged onto the position at which it strikes the detector. A position-sensitive detector allows the varying electric potentials to be mapped and to apply corrections to each detected electron.
- There are various sources of background, mainly electrons produced by ionization in the residual gas, electrons from interactions of cosmic rays, and γ -rays from natural radioactivity emanating from material surrounding the detector and from the detector itself. Here, positional information also helps, but most important is the accurate determination of the energy of the electron. β -electrons of interest occur in a narrow energy window, whereas backgrounds vary over a large range of energies, thus, accurate energy determination improves the ability to separate β -electrons for backgrounds.

The detector is a monolithic PIN diode array on a 5"-wafer consisting of 148 pixels arranged in a *dart board* pattern which provides the spatial information. The typical energy resolution of an individual pixel is 1.4 keV (FWHM) [KAT14]. To suppress intrinsic backgrounds, the detector is surrounded by cylinders of lead and copper shielding. Backgrounds associated with cosmic rays are tagged using a cylindrical plastic scintillator veto

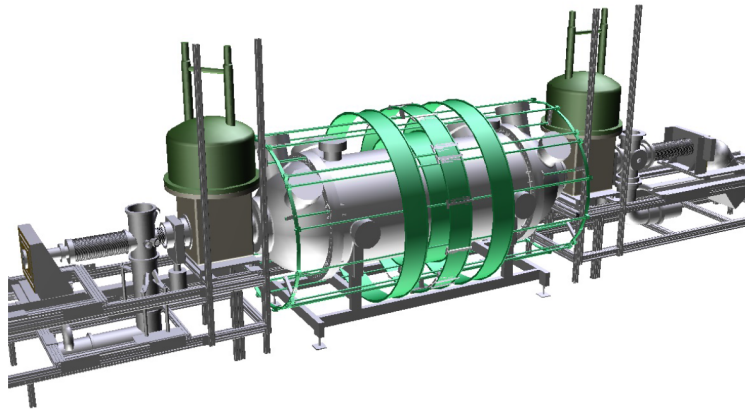


Figure 2.8.: The KATRIN Monitor Spectrometer [KA14]

surrounding the lead and copper shielding. Signals from the PIN diode array and the veto are read out using custom designed electronics, ranging from the front-end pre-amplifiers up to the end of signal processing by the data acquisition system, including read-out software and analysis tools.

To reduce backgrounds and to be compatible with extreme ultra-high vacuum requirements, special care had to be taken in the design and manufacture of the detector. Neither of these requirements is satisfied by standard industrial mounting and connection techniques for multi-pixel silicon detectors. Compatibility with up to 6 T magnetic fields and the need to mount the electronics close to the detector present additional design challenges. The solution involved the use of a custom vacuum feed-through with spring loaded pins contacting the individual pixels. The radioactively *hot* electronics, i.e. that could emit some radioactivity because of plastic parts, are placed on the other side of the vacuum flange where they can be shielded by high purity copper. As a further defense against backgrounds, the FPD system is able to provide up to 30 kV of *post acceleration* to the electrons coming from the main spectrometer, thereby raising them from regions of high activity to regions of lower activity. Post-acceleration presents a number of challenges. The detector and its readout electronics must be read out while being biased by up to +30 kV. The application of high acceleration voltages in the presence of magnetic fields of up to 6 T requires careful design in order to avoid discharges that may damage the detector and electronics.

2.4.3. The Monitor Spectrometer

The 70 m long KATRIN beam line is complemented by a second independent beam line for on-line monitoring of the actual retarding voltage at the main spectrometer [KA14]. This second 5 m long monitor beam line runs parallel to the main beam line. The monitor beam line has the following functional units:

- a monitor source which emits mono-energetic electrons in the energy range from 17.8 to 32 keV

- a high resolution MAC-E filter (the modified Mainz spectrometer), which is fed by the same retarding HV as the KATRIN main spectrometer and thus provides an on-line monitoring of the retarding HV of the main spectrometer
- a segmented silicon based PIN-diode array for β -counting (the modified detector system used for the pre-spectrometer measurements)

To minimize the stray fields of the monitor beam line at the KATRIN's one (and vice versa), the two setups are separated into two different buildings. The monitor spectrometer is used to monitor the stability of the high voltage of the main spectrometer. Like the main spectrometer, it is operated as a MAC-E-Filter. It measures the energy of conversion electrons from the Krypton-83 decay, which are mono-energetic with small line width. Basically, it is an almost 10 m long, very accurate voltmeter, using a nuclear standard as a reference.

3. Implementation of a realistic DPS and CPS geometry in the simulation framework Kasper

Kasper is the global analysis and simulation package for the KATRIN experiment. It is written primarily in C++ and contains semi-independent modules for both data analysis and simulation.

In order to be able to produce a realistic simulation of the behavior of tritium ions in the KATRIN transport section, we first have to implement a geometry, as close as possible to the real one, into the simulation framework. This chapter will introduce the submodule KGeoBag (see section 3.1), which deals with the geometry in Kasper, as well as the way the DPS (see section 3.2) and CPS geometries (see section 3.3) were reproduced in Kasper and the tools that were used and developed for this purpose (see section 3.2.1 and 3.3). It will also mention the way the geometry was transformed to follow the shrinking caused by cooling the components down to cryogenic temperatures (see section 3.3.2).

3.1. Modeling of arbitrary geometries with KGeoBag

KGeoBag is the geometry library for Kasper. It allows constructing and operating three dimensional models via an XML interface. The software translates the information written as XML code into C++ objects which are then available for rendering.

The construction of a geometry with KGeoBag relies on the proper usage of several basic geometry elements that will be combined in order to create a more complex geometry. These geometry elements are of two kinds:

- basic shapes, for example, polygons or circles, which may also be rotated or extruded (figures 3.2a-3.2b-3.2d-3.2e)
- pre-made templates of more complex shapes that cannot be built by assembling simple shapes (figure 3.2c)

The task of building a geometry with KGeoBag thus reduces to constructing a specific geometry from elements available in KGeoBag.

The XML configuration files are organized as follows. The part containing your geometry begins with `<geometry>` and ends with `</geometry>`. You can then add an element by writing its type within tags and as well as a name for it. You then have to define the parameters of your element and close the tag. For example:

```

1 <flattened_circle_surface name="flattened_circle_surface" z="0."
   flattened_mesh_count="10" flattened_mesh_power="4.">
2 <circle x="0.1" y="0.2" radius="0.5" circle_mesh_count="128"/>
3 </flattened_circle_surface>
4

```

will create a disk of 0.5 m radius, whose center is at <0.1 m,0.2 m> in the local coordinate system, composed of 10 elements in the radial direction times 128 elements in the azimuthal direction.

You can then organize your elements by putting them into a space and specifying their coordinates and rotations. For example:

```

1 <space name="dps2f_left_compensation_coil_1" node="
   dps2f_compensation_coil">
2 <transformation rotation_euler="0,0,0." displacement="0,0,-0.2748"/>
3 </space>
4

```

will place the element dps2f_compensation_coil, renamed dps2f_left_compensation_coil, by 0.2748 m to the left from the reference point without rotating it.

The angles used to rotate the element are Euler angles. To transform the usual angles α and β of axisymmetric elements into Euler angles ϕ and θ (figure 3.1), we used the following formulas:

$$\tan(\alpha) = \frac{Z_1}{Z_3} \quad (3.1)$$

$$\tan(\beta) = \frac{Z_2}{Z_3} \quad (3.2)$$

$$\tan(\phi) = \frac{Z_1}{Z_2} = \frac{\tan(\alpha)}{\tan(\beta)} \quad (3.3)$$

$$\cos(\phi) = \frac{Z_2}{Z_{xy}} \quad (3.4)$$

$$\sin(\phi) = \frac{Z_1}{Z_{xy}} \quad (3.5)$$

$$\tan(\theta) = \frac{Z_{xy}}{Z_3} = \frac{\tan(\alpha)}{\sin(\phi)} = \frac{\tan(\beta)}{\cos(\phi)} \quad (3.6)$$

The following elements have been used to model the STS:

- rotated poly loop surface: a polygon rotated around the z-axis (figure 3.2a)
- cylinder tube space: a cylinder defined by its inner and outer radius and its length (figure 3.2b)
- port housing surface: a complex surface consisting of a cylinder orthogonally pierced by cylindrical or rectangular port. The cylinder is defined by its radius and its length.

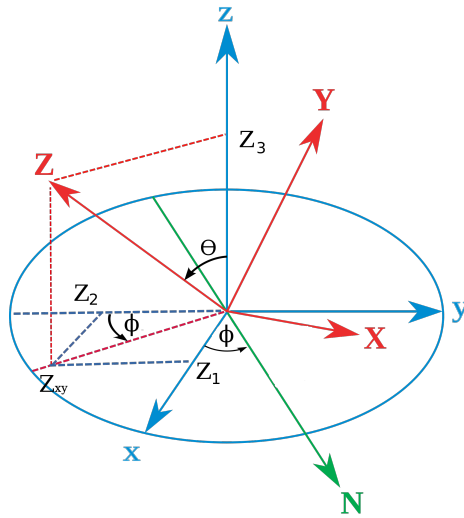


Figure 3.1.: Projection of the direction vector [JS10]

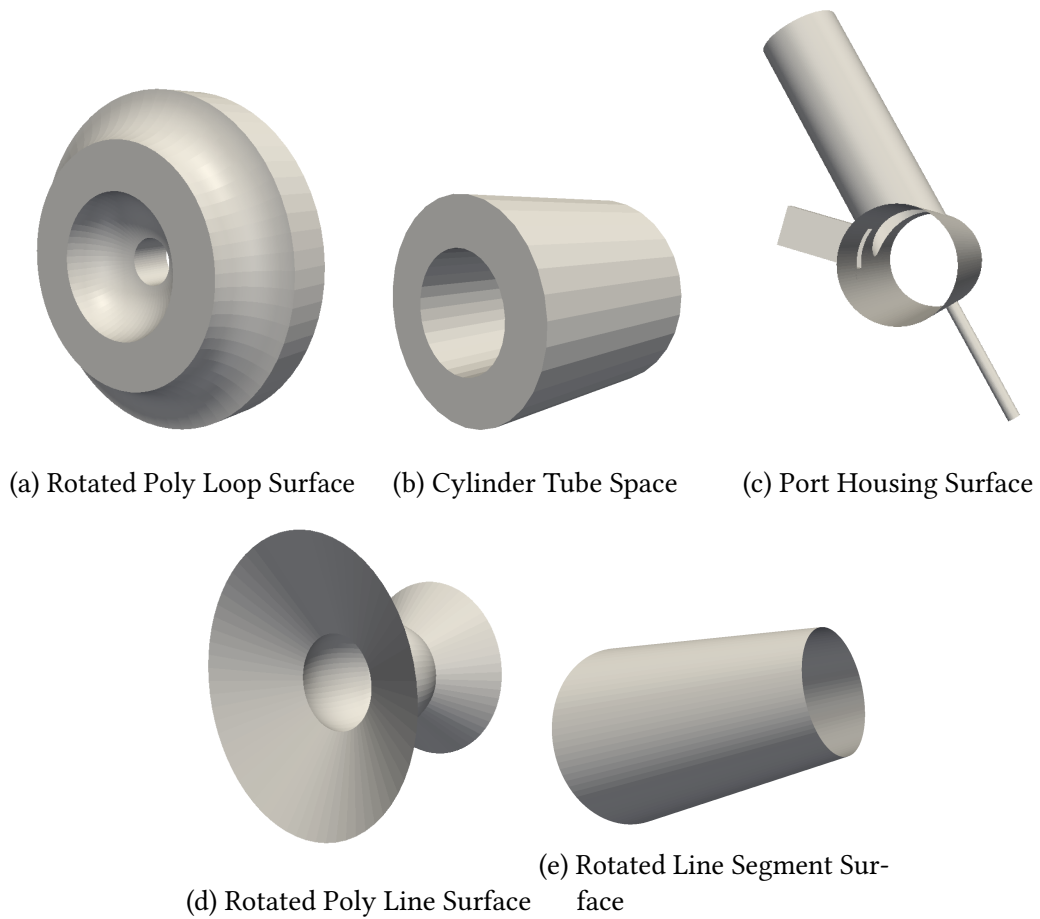
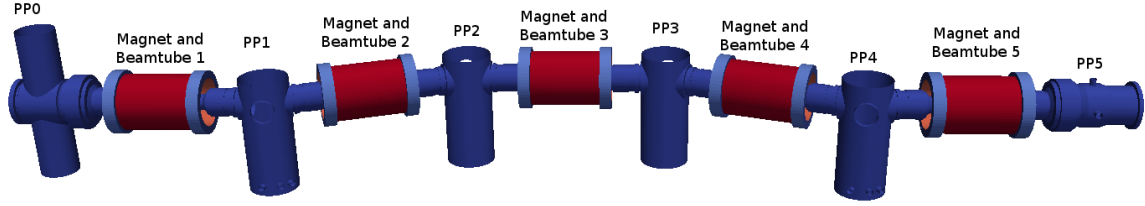
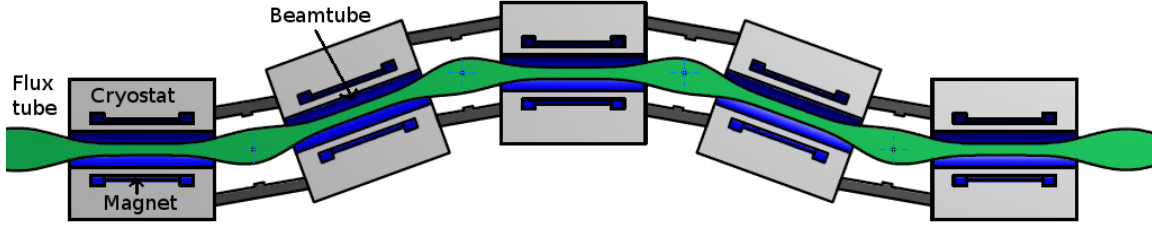


Figure 3.2.: Primitive elements of KGeoBag for the STS model



(a) DPS 3D Geometry including magnets



(b) Technical drawing of the DPS [Int]

Figure 3.3.: The DPS geometry

The ports are defined respectively by their end position and radius, and by their end position, length and width (figure 3.2c)

- rotated poly line surface: a polyline rotated around the z-axis (figure 3.2d)
- rotated line segment surface: a simple segment rotated around the z-axis (figure 3.2e)

3.2. Presentation of the DPS Geometry

As already mentioned in 2.3.3.1, the DPS is composed of several independent parts. Here is a review of how the DPS was built in KGeoBag from the technical drawings. These drawings, the XML code and an image of the corresponding 3D geometries can be found in the appendix.

The DPS Beamtubes

There are two different beamtube geometries for the DPS, for the central section and the end parts of the DPS, respectively. The beamtubes in the center are called `beamtube_middle` in the XML configuration file. They correspond to the drawing *316-DWG-0-0027-01* (figure A.2 in appendix). As they are symmetric, the reference point was chosen to be in the middle of the beamtube. The beamtubes at each end are the element called `beamtube_end` in the XML configuration file. They correspond to the beamtube of the drawing *316-DWG-0-0026-01*. As the part directed toward the center of the DPS is the exact reproduction of those of the middle beamtubes, the reference was chosen to be the same as the middle

beamtube. In order to avoid unnecessary complicated models, we gave up the *screws* that are asymmetric and not relevant to the computation. We also simplified the bellows by replacing them with a cylinder whose inner and outer radius are the maximum and minimum radius of the bellows. The two beamtubes have been modeled with rotated poly loop surface as they have a defined thickness and are now axisymmetric.

The DPS magnets

The DPS magnets are made of three coils of two different types: a main coil and two compensation coils at both ends. They are named `dps2f_main_coil` and `dps2f_compensation_coil`, respectively and were built according to dimensions calculated by F. Glück (figure A.2 in appendix). The reference point of each magnet is its center point. The magnets were modeled with cylinder tube space which suits perfectly their geometry.

The DPS Pump Ports

There are three different types of pump ports for the DPS. All of the pump ports placed between two DPS beamtubes are the same but the ones at the beginning and end of the DPS are different.

The pump port at the beginning has been named PP0 in the XML configuration file. There is no existing drawing of this pump port, so the dimensions have been extracted from the CAD file. The geometry was made using a pump port housing surface for the middle (`pump_port_middle` in the code) and rotated poly loop surfaces for the ends (respectively `pump_port_left` and `pump_port_right` in the code). The reference point was chosen to be in the middle of the port.

The four middle pump ports were separated in two pump port housing surfaces because of the restraint of those surfaces. Actually, the pump port housing surfaces do not allow building two ports in the same location. As the DPS pump ports have a port in their inside and in their outside at the same location, they were separated in an inner and an outer pump port housing surface. These surfaces are respectively named `pump_port_intern` and `pump_port_extern` in the code. They correspond to the drawing *316-DWG-0-0004-01* (figure A.4 in appendix). Because of the limitation of the pump port housing surface, the two ports close to the big lateral ports were not included in the geometry. As they are not relevant for the calculation the caps of the pump ports were not implemented, either. The flanges of the ports, connecting them to the beamtubes, were added to the beamtube elements as they cannot be built with the port housing surface.

The pump port at the end of the DPS was named PP5 in the XML code. It corresponds to the drawing *Chamber CPS*. The central part of the pump port was made with a pump port housing surface (`PP5_middle` in the code). The two ends as well as the ventilator were made with rotated poly loop surfaces (respectively `PP5_left`, `PP5_right` and `PP5_ventilator`). The reference point was once again chosen to be in the middle of the ports. As we do not have much information about it, the below was given up in the geometry.

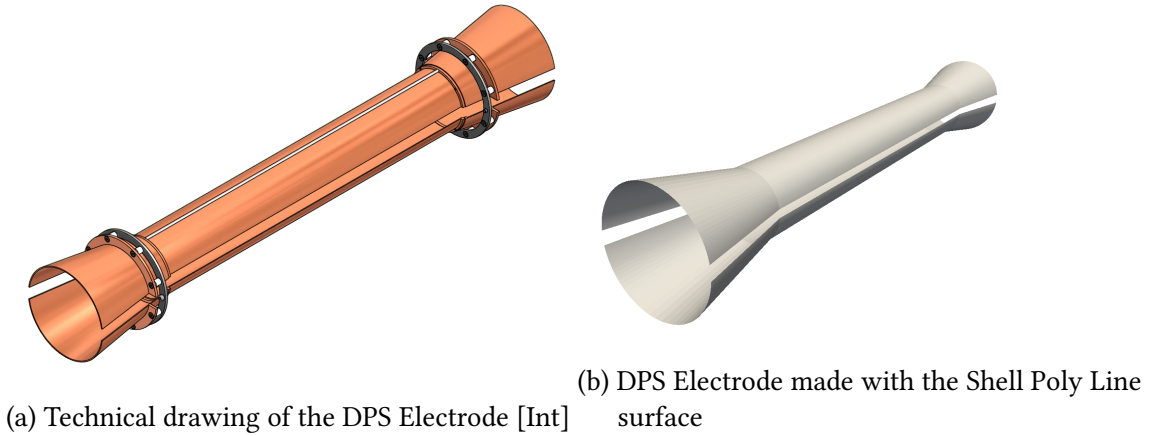


Figure 3.4.: Comparison between the design and the 3D geometry of the DPS electrodes

The FT-ICR modules

The FT-ICR modules geometry is pretty complicated. As we will only use them for the margin measurement, we can simplify them. The FT-ICR has two sets of dipole electrodes in the middle and a Penning-trap electrode at each end. They are here modeled by 3 ring-shaped electrodes. The FT-ICR tube is the element named `fticr_tube`. As the electrodes have the same length and diameter, we built the element `fticr_electrode` to model them all. The dimensions come from the Drawing *Trap-drawings-2-01* (figure A.7 in appendix). The reference point was chosen to be the middle of the measurement electrode. As the flux tube must be contained inside the FT-ICR modules, we gave up the bellow and the fine external structure of the FT-ICR that are not relevant to our simulation. The tube was also modeled as two cylinders with the rotated poly line surface and the electrodes were built using a rotated line segment surface.

3.2.1. The dipole electrodes and the shell surfaces

As said in section 2.3.3.1, the DPS was conceived with three sets of dipole electrodes placed in the three middle beamtubes. Each set of electrodes is composed of two half shells facing each other, one at the top, one at the bottom (figure 3.4a). The dimensions of the electrode come from the drawing *Muster* (figure A.9 in appendix).

The purpose of these electrodes is to induce a dipolar electric field in the DPS beamtubes, forcing the tritium ions to drift according to the well-known $\vec{E} \times \vec{B}$ drift effect, to eliminate them on the beamtubes surface. The inner diameter of the electrodes was conceived big enough to prevent a collision with the 191 T cm² flux tube.

As can be seen in figure 3.4a, the design of the electrodes is quite simple. Unfortunately, as they are asymmetric, no combination of basic elements from KGeoBag allows in recreating this geometry. We then had two choices: we could try to create a geometry as close as possible to real one with the available elements or we could implement new geometry elements to KGeoBag. In the first four month of this thesis, we worked with the first solution. The calculation made with these electrodes suffered a lack of precision so we

decided to move to the second option. We thus had to implement a new geometry element into KGeoBag: the shell surfaces.

The shell surfaces are basic elements of KGeoBag (polygon, circle, etc.) rotated between two angles. It means, instead of having a 3D object created by the *full* rotation of a 2D object, one obtains it by rotating the 2D object only partially. It then allows you to create surfaces that are not rotationally symmetric but still inherit from a simple 2D object.

With the help of this new element, we could now build the dipole electrode, named *electrode* in the code, with the Shell Poly Line surface (figure 3.4b).

Our DPS Geometry is now complete, as can be seen on the figure 3.3a.

3.3. Presentation of the CPS Geometry

The CPS geometry is much more complex than the DPS geometry. It contains many asymmetric elements as well as two different types of pump ports and a cold gate (figure 3.5a). To realize this geometry, we had to divide it in symmetric and asymmetric parts. All the bellows were simplified as usual. The heating and cooling system were not implemented as they are not relevant to the simulation.

The CPS Magnets

The CPS Magnets are as simple as the DPS ones. There were thus made with the same geometry element. The reference is the same. The main difference with the DPS is that each magnet has his own dimensions. We also had to build seven geometry elements named `cps_coils_x_space` with x varying between 1 and 7. The dimensions of the magnets come from calculations made by F. Glück (figure B.1 in appendix).

The DPS Flange

The DPS Flange is the element connecting the PP5 ventilator to the CPS. It corresponds to the element `DPS_flange_surface` in the code and the drawing 688RM12427 (figure B.10 in appendix). The reference point was chosen to be the left end of the flange. The screwing holes were not implemented in the geometry as they are not relevant to the simulation.

The Cold Valve

The cold valve is a complex element. But, as we only need it for distance measurement, we do not need the big vertical part of the valve, and as the only asymmetric part is in the middle, we realized a symmetric geometry with, in the middle, a rotated surface with diameters corresponding to the smallest distance to the beam line. As for the other elements, the bellows were given up to be replaced by cylinders. The cold valve is also the rotated poly loop surface called `cold_gate_surface` in the code. Its reference is in the center of the valve. The dimensions come from drawings 333460 and 394903 (figure B.3 in appendix).

The Second Pump Port

The second pump port is quite simple, but, unfortunately, the code does not allow us to build the lateral port because of the overlapping of mesh elements. As for the other pump ports, we did not implement the caps. The pump port is so the `pump_port_surface` in the code. It corresponds to the drawing *688RM12491* (figure B.7 in appendix). The reference point was chosen to be in the middle of the pump port. The ports were included in the beamtube geometry in order to improve the distance calculation.

At this point, we still have not made most of the asymmetric parts of the CPS: the first pump port and the cones at the end of the beamtubes. As the pump port cylinder is asymmetric, we could not make it with a pump port housing surface. We had to give up the lateral port in order to be able to build the first pump port with a beam surface. The cut cones at the end of the beamtubes were also made with beam surfaces.

The PS Flange

The PS Flange is the element connecting the CPS to the Pre-Spectrometer. It corresponds to the element `PS_flange` in the code and to the drawing *688RM12745* (figure B.12 in appendix). The reference point was chosen to be on the laser reflection stand of the flange.

3.3.1. The Beam surface in the CPS geometry

The beam surface is a surface created by positioning an assembly of quadrilateral as the sides of a 3D surface. It allows us to build highly asymmetric surfaces but is still some kind of sampled surfaces and can also lead to imprecision in results.

With this geometry element, we can build the remaining CPS elements.

The First Pump Port

As the first pump port is asymmetric, we have to build it with a beam surface. This then does not allow us to build the lateral port. The pump port corresponds to the `pump_port` element in the code and to the drawing *688RM12430* (figure B.4 in appendix). The reference point was chosen to be in the middle of the *uncut* pump port. The flanges connecting it to the beamtubes were added to their respective codes and symmetrized.

The CPS beamtubes

The CPS has seven different beamtubes. We so have to build each beamtube independently. The beamtubes were separated into three elements as their ends have to be built with beam surfaces. The middle of the beamtubes are rotated poly loop surfaces named `beam_tube_x_surface`, x varying between 1 and 7. The left ends of the beamtubes are named `beamtube_x_begin` and the right ends `beamtube_x_end`. They are both beam surfaces. As the middle of the 3rd and 4th beamtubes are the same, we built a `beamtube_3and4_surface` for both.

First Beamtube

The first beamtube is totally axisymmetric. It is hence composed of only one element corresponding to the drawing *688RM12437*. The reference point is in the middle of the cylindrical part of the beamtube. The holes of the shield were not implemented. The empty space comprised between the outside of the shield and the inside of the beamtube was considered full as it will not interact with anything in the simulation.

Second Beamtube

The second beamtube corresponds to the drawing *688RM12421*. The reference point of the symmetric part of the beamtube is the junction of the two parts of the cryotrap. The teeth of the cryotrap were modeled as a smooth surface following the dimensions of the technical drawing. The asymmetric part is a cone cut at both ends with two different angles. The reference point is the middle of the uncut cone. The connecting flange was given up as it can be built with the beam surface and is of no interest.

Third Beamtube

The third beamtube corresponds to the drawing *688RM12422* (figure B.9 in appendix). The left asymmetric part is a cut cylinder. Its reference point is its middle before the cut. The connecting flange was given up. The middle part is symmetric. Its reference point is the junction of the two parts of the cryotrap. The teeth of the cryotrap were modeled as a smooth surface following the dimensions of the technical drawing. The right part is a cone cut at both ends with two different angles. The reference point is the middle of the uncut cone. The connecting flange was omitted in the model.

Fourth Beamtube

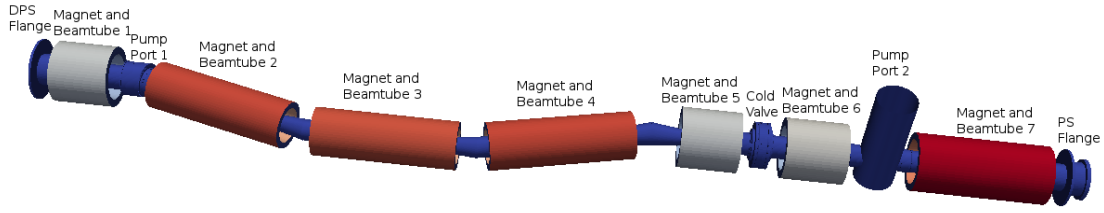
The only difference between the beamtube 3 and 4 are the dimensions. The drawing corresponding to this beamtube is the drawing *688RM12423*.

Fifth Beamtube

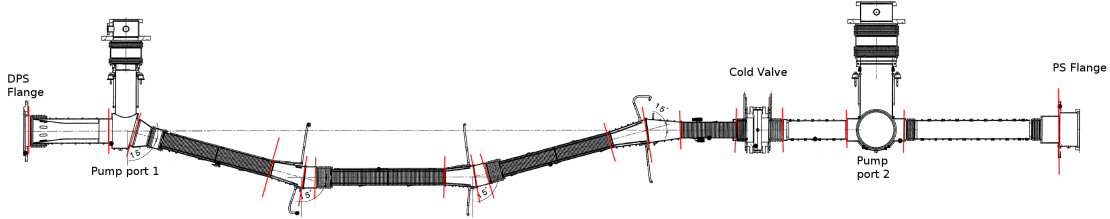
The fifth beamtube begins with the same kind of cone as there is at the end of the third and fourth beamtubes. The reference point of the middle part is in the middle of the cylindrical part of the cryotrap. The teeth of the cryotrap were modeled as a smooth surface following the dimensions of the technical drawing. This beamtube corresponds to the drawing *688RM12424*.

Sixth Beamtube

The sixth beamtube is totally symmetric. It corresponds to the drawing *688RM12425*. The reference point is the middle of the beamtube.



(a) 3D Geometry of the CPS as built



(b) Technical drawing of the CPS [Int]

Figure 3.5.: The CPS geometry

Seventh Beamtube

The seventh beamtube is symmetric, too. As there will be NEG pumps in its center, they were implemented in the code although they are not in the drawing 688RM12482. the reference point is in the middle of the cylindrical part.

3.3.2. Cryogenic Temperature and Shrinking Factor

The working temperature of the center of the CPS is 4.5 K. Due to the thermal contraction of the metal, we have to recalculate the dimensions of the CPS as well as the positions of the elements. The calculation was made by the manufacturer of the CPS, the company ASG, and the results can be found in [ASG14]. The relative position of the intersection of the axis of the beamtubes (figure 3.5b) was computed by considering the shrinking to be linear. It allows us to calculate the new length of the bellows that are the only elements with a free length. The coordinates of the intersection points after shrinking are presented in table 3.1.

These values allow us to implement the new dimensions and positions of the geometry elements for each axis. As the shrinking calculation was only made for the as-built CPS, we have to assume that the results would have been the same for the design CPS.

We finally have our CPS geometry completed (figure 3.5a). As we have the position of the CPS magnets as built, we also made an as-built geometry beside the design geometry. The difference between the as-built and the design geometry is that the elements of the CPS are not perfect. There can be a small difference in the dimensions of the element as well as in the position and angle relatively to each other. It is of great importance for us, because these differences can cause a shift of the flux tube big enough to make the electrons collide with the beamtube, causing thus a dramatic loss of statistics.

Table 3.1.: Coordinates of the intersection points in the CPS after the shrinking due to cooling

| Intersection | x (mm) | y (mm) | z (mm) |
|------------------------|---------------|---------------|---------------|
| DPS flange/Beamtube 1 | 0.5 | -0.6 | 204.0 |
| Beamtube 1/Beamtube 2 | 0.0 | 0.2 | 859.1 |
| Beamtube 2/Beamtube 3 | -289.8 | -0.1 | 1940.1 |
| Beamtube 3/Beamtube 4 | -289.7 | 0.0 | 3005.3 |
| Beamtube 4/Beamtube 5 | -0.2 | 0.2 | 4088.1 |
| Beamtube 5/Cold Valve | 0.0 | 0.4 | 4771.6 |
| Pump Port 2/Beamtube 6 | 0.7 | 0.1 | 5506.8 |
| Beamtube 7/PS Flange | 0.3 | 0.7 | 6779.9 |

4. Computation of Electromagnetic Fields in the DPS and CPS

After the geometry has been constructed with KGeoBag, we can now start to calculate electromagnetic (EM) fields. The computation of EM fields with KEMField relies on the numerical solution of Maxwell's equations applied to our system. The algorithms will be introduced in 4.1 and the results of the computations of the electric and magnetic fields for the DPS and the CPS will be presented in section 4.2 and 4.3, respectively.

4.1. Computation of Electromagnetic Fields with KEMField

KEMField is the electrostatic and magnetostatic simulation library for Kasper. It is a toolkit written in C++ for solving electrostatic and magnetostatic fields from user-defined electrode and magnet configurations [Cor14]. It includes KGeoBag bindings to allow the usage of geometry elements in that library. Furthermore, the code execution can be parallelized by using OpenCL¹ and MPI² libraries. KEMField takes advantage of the Boundary Element Method (BEM) (4.1.1), which is used to compute discretized charge densities from user-defined potential distributions along electrodes. The field is computed using a combination of zonal harmonic expansions (4.1.4), fast Fourier transform on multipole and direct calculations (4.1.3) from geometry primitives using the principle of superposition. In addition, adaptive-refinement field maps can be generated for commonly accessed regions with computationally complex electric fields. The techniques employed are adapted from the routines of Dr. Ferenc Glück [Glü11][FL*12].

4.1.1. Computation of Potentials with the Boundary Element Method

The BEM [PB05] is a technique for numerically solving linear partial differential equations that can be represented as an integral over the domain boundary.

BEM has become more popular since the 1980s. Because it requires calculating only boundary values, rather than values throughout the space, it is significantly more efficient in terms of computational resources for problems with a small surface/volume ratio. This restricts the applicability of the technique to a subset of PDEs, but also reduces the dimensionality of the problem and facilitates the calculation of fields for regions that extend out to infinity. Conceptually, it works by constructing a *mesh* over the modeled surface. Boundary element formulations typically give rise to fully populated matrices. This means

¹www.khronos.org/opencv

²www.open-mpi.org

that the storage requirements and computational time will tend to grow according to the square of the problem size.

BEM is applicable to problems for which Green's functions can be calculated. These usually involve fields in linear homogeneous media. This places considerable restrictions on the range and generality of problems suitable for boundary elements. Non-linearities can be included in the formulation, although they generally introduce volume integrals which require the volume to be discretized before solution, removing an advantage of BEM.

The method involves taking an integral equation that describes a field as a function of its boundaries, and feeding the boundary conditions to the equation in order to construct a profile for the unknown function in the integrand. Many variants of the BEM exist. The version used in KEMField is known as an indirect Boundary Element Method.

The point of the BEM in KEMField is to resolve the Laplace equation of our potential function for our system Ω :

$$\nabla^2 u(\vec{x}) = 0, \quad \vec{x} \in \Omega. \quad (4.1)$$

On our system boundary, our potential ϕ has been defined in the XML code. We then know

$$u(\vec{x}) = \phi(\vec{x}), \quad \vec{x} \in d\Omega \quad (4.2)$$

with $d\Omega$ our boundary.

By applying Green's second identity, we obtain

$$u(\vec{x}) = \int_{d\Omega} \frac{1}{4\pi\epsilon_0|\vec{x} - \vec{y}|} \sigma(\vec{y}) dS_y, \quad \vec{x} \in \Omega \quad (4.3)$$

$$= \int_{d\Omega} G(\vec{x}, \vec{y}) \sigma(\vec{y}) dS_y \quad (4.4)$$

with $\sigma(\vec{x})$ the charge density function we want to compute. We then discretize our boundary into a *mesh*

$$d\Omega = \bigcup_{i=1}^N \Delta_i \quad (4.5)$$

with the Δ_i being small elements easy to compute as triangles or rectangles, with σ supposed constant over the element. Our discretization gives us the equation

$$\phi(\vec{x}_i) = u(\vec{x}_i) = \sum_{j=1}^N \sigma_j \int_{\Delta_j} G(\vec{x}_i, \vec{y}) dS_y \quad (4.6)$$

$$b_i = \sum_{j=1}^N \sigma_j A_{ij} \quad (4.7)$$

with x_i the center of Δ_i and b_i the potential in x_i . To obtain our charge density vector, we could then invert the matrix A

$$A\vec{\sigma} = \vec{b} \quad (4.8)$$

$$\vec{\sigma} = A^{-1}\vec{b} \quad (4.9)$$

but it is very time-consuming. This calculation of the charge density vector is performed with the methods presented in the next section.

Once all charge densities σ_i are known, we can obtain the potential of each point of our system with

$$u(\vec{y}) = \sum_{\Delta_i} G(\vec{y}, \vec{x}_i) \sigma(\vec{x}_i), \quad \vec{y} \in \Omega. \quad (4.10)$$

4.1.2. The Robin Hood Algorithm for Charge Density Calculation

The Robin Hood algorithm [FL*12][LSA06] is close to the boundary element methods, although significant conceptual differences exist with respect to this class of methods. Its goal is to achieve equipotentiality of conducting surfaces by iterative non-local charge transfer. For each of the conducting surfaces, non-local charge transfers are performed between surface elements which differ the most from the targeted equipotentiality of the surface.

As for the BEM method, the Robin Hood method generates a charge density vector σ_i . At the beginning of the algorithm, the charge density is chosen to be uniform on the surface for its charge neutrality. The potential of every mesh element is then computed and two of the elements with respectively the lower and the higher potential are chosen. A charge transfer is operated between these two elements so that their potentials become equal. The algorithm earns its name because of this *taking from the maximum and giving to the minimum* technique. The new potentials are then recomputed and the method is iterated until the surface achieves equipotentiality. Figure 4.1 shows a flow chart of the algorithm.

As for the BEM method, the goal is to solve the equation

$$u(\vec{x}) = \int_{d\Omega} G(\vec{x}, \vec{y}) \sigma(\vec{y}) dS_y \quad (4.11)$$

$$u(\vec{x}_i) = \sum_j I_{ij} q_j \quad (4.12)$$

$$\text{with } q_i = \sigma_i \Delta S_i \quad (4.13)$$

ΔS_i being the area of the element Δ_i .

We have to separate the resolution for insulators and conductors because of the difference in the neutrality of the elements.

Insulator

For the element to stay neutral the charge received must be the same as the charge sent. The new potentials after the transfer of a charge q_T from the elements Δ_m to the element Δ_n are

$$U'_m = U_m - I_{mm} q_T + I_{mn} q_T \quad (4.14)$$

$$U'_n = U_n + I_{nn} q_T - I_{nm} q_T, \quad (4.15)$$

$$\text{with } U'_m = U'_n : \quad q_T = \frac{U_m - U_n}{I_{mm} + I_{nn} - I_{mn} - I_{nm}}. \quad (4.16)$$

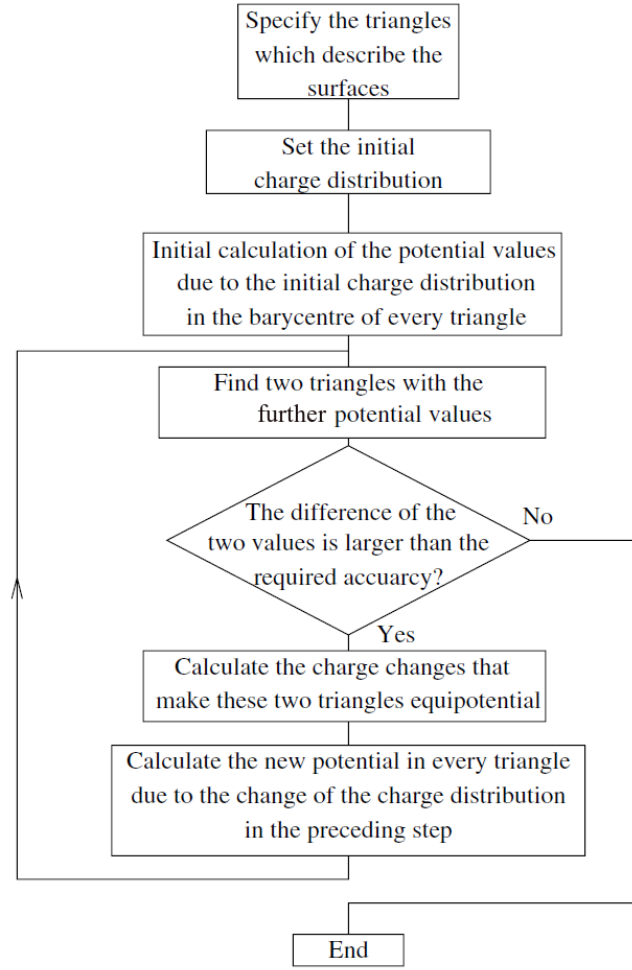


Figure 4.1.: Flow chart of the Robin Hood algorithm [LSA06]

Conductor

With an exterior power supply, the number of charge received can be different from the charge sent. The new potentials after the reception of respectively q_{Tm} and q_{Tn} by the elements Δ_m and Δ_n are

$$U'_m = U_m + I_{mm}q_{Tm} + I_{mn}q_{Tn} \quad (4.17)$$

$$U'_n = U_n + I_{nn}q_{Tn} + I_{nm}q_{Tm} \quad (4.18)$$

With $U'_m = U'_n$,

$$q_{Tm} = \frac{(U_{ext} - U_m)I_{nn} - (U_{ext} - U_n)I_{mn}}{I_{mm}I_{nn} - I_{mn}I_{nm}} \quad (4.19)$$

$$q_{Tn} = \frac{(U_{ext} - U_n)I_{mm} - (U_{ext} - U_m)I_{nm}}{I_{mm}I_{nn} - I_{mn}I_{nm}}. \quad (4.20)$$

As can be seen in the chart, the algorithm will iterate its charge exchange until the difference between the further potentials is smaller than a user-defined value. At the end, we obtain the charge density vector σ_i by reversing the equation (4.13), and with it the potential at every point of our system.

4.1.3. Comparison between the Direct and the FFTM Field Solver

The previous algorithm allows us to obtain a vector containing the charge density for each mesh element. It allows us to compute both the potential and the electric field at each point of our system. The two most important algorithms to do this in KEMField are the integrating field and the Fast Multipole solver. Both are using the precomputed charge density vector to compute the field at every point of our system.

The integrating field solver is a direct method that will compute the electric field by integrating the charge density gradient.

$$E_i(x) = \sum_j \int_{\Delta_j} \partial_i G(x, y) dy \cdot \sigma_j \quad (4.21)$$

The integral are analytically computed for each Δ_j . This solver is a bit slower as the number of mesh elements can be quite large.

The Fast Multipole solver of KEMField is a hybrid of a fast Fourier Transform on Multipoles Method (FFTM) [OLL04] and a Fast Multipole Method (FMM) [CGR99]. It proceeds by calculating the far contribution with a multipole expansion to compute only the closer contribution directly.

Given a localized distribution of charges $q(y)$, the potential $u(x)$ can be approximated by the following multipole expansion of degree p :

$$\tilde{u}(x) \approx \sum_{n=0}^p \sum_{m=-n}^n M_n^m \frac{Y_n^m(\theta, \phi)}{r^{n+1}}, \quad (4.22)$$

where M_n^m are the multipole moments, which are associated with their corresponding spherical harmonics $Y_n^m(\theta, \phi)$.

$$M_n^m = \int q(y) Y_n^{-m}(\theta', \phi') r'^l d^3 y \quad (4.23)$$

There is also a Taylor series analog to the multipole expansion, called the local coefficient expansion. This local coefficient expansion is given by:

$$\tilde{u}(x) \approx \sum_{n=0}^p \sum_{m=-n}^n r^n L_m^n Y_m^n(\theta, \phi), \quad (4.24)$$

where L_m^n are the local coefficients.

The algorithm works as follows:

- The algorithm discretizes the system in cubes V_i .
- The multipole moments are calculated analytically and used to compute the local coefficients.
- As the *near* charges are inaccurately represented by multipole expansions, we use them to compute only the *distant* contribution:

$$E_{i,\text{far}}(x) = \sum_{n=0}^p \sum_{m=-n}^n L_m^n \partial_i (r^n Y_m^n(\theta, \phi)). \quad (4.25)$$

Table 4.1.: Time of computation for charge densities and local coefficients

| Mesh elements | Time (CPU) | Time (GPU) |
|---------------------------|------------|------------|
| Charge densities | | |
| 5000 | 47'28" | 00'45" |
| 20000 | 61'12" | 04'13" |
| Local Coefficients | | |
| 5000 | 00'29" | 00'33" |
| 20000 | 02'37" | 00'42" |

Table 4.2.: Time of computation for the direct solver and the fast multipole solver

| Field Solver | CPU | GPU |
|----------------|---------|--------|
| Direct Solver | 110'12" | 40'20" |
| Fast Multipole | 1'40" | 00'44" |

- The *near* contribution is computed analytically as follows:

$$E_{i,near}(x) = \sum_{\substack{neighbor \\ j}} \int_{\Delta_j} \partial_i G(x, y) dy \cdot \sigma_i \quad (4.26)$$

This method is faster than the direct solver as it computes analytically only the contribution from the neighbors. As the local coefficients are saved in a file, it is a bit slower the first time it runs, but it allows being faster afterwards.

A few tests were made to show the difference between the two algorithms. We first computed the charge densities for a 10^{-6} tolerance and the local coefficients of the fast multipole solver for different numbers of mesh elements on a CPU and a GPU (table 4.1). The second test was a computation of the potential and electric field at 10000 points for a geometry of 103,522 mesh elements (table 4.2).

As it can be seen, the direct solver is more efficient for a very small number of calculations as the FFTM solver has to compute all the local coefficients no matter how much calculation it has to perform later on. However, as it only does it once, it becomes faster as the number of calculation increases.

After confirming the speed advantage of the FFTM method, we will now investigate the precision compared against the direct solver. We first computed the potential and field for a plate capacitor with a 1 cm gap at ± 100 V, in order to be able to unveil the precision of the two algorithms. The results are presented in the table 4.3. We then computed the potential and with at some well-chosen points of the DPS with both algorithms to compare the values. The results are presented in table 4.4.

As can be seen in table 4.3, the results given by the direct solver are both accurate and precise. As the charge density calculation was made with a 10^{-5} tolerance, the 2.5×10^{-5} accuracy of this solver is very satisfying. Although it has a good precision, with its 6.5×10^{-5} accuracy, the fast multipole solver tends to lose in accuracy what it wins in computation time.

Table 4.3.: Comparison of the results for the plate capacitor

| Coordinates | | | Analytic Calculation | | Direct Field Solver | | Fast Multipole Solver | |
|-------------|--------|--------|----------------------|----------------------|----------------------|----------------------|---------------------------|----------------|
| X (m) | Y (m) | Z (m) | Potential (V) | E _x (V/m) | Potential (V) | E _x (V/m) | Potential (V) | E _x |
| 0.000 | 0.000 | 0.000 | 0 | 10000 | 2.5×10^{-5} | 10000 | -6.5587×10^{-5} | 9998.52 |
| 0.000 | 0.000 | 0.010 | -100 | 10000 | -100 | 10000 | -99.9615 | 9992.79 |
| 0.000 | 0.000 | -0.010 | 100 | 10000 | 100 | 10000 | 99.8722 | 9993.00 |
| 0.001 | 0.000 | 0.000 | 0 | 10000 | 2.6×10^{-5} | 10000 | -6.4771×10^{-5} | 9998.53 |
| -0.001 | 0.000 | 0.000 | 0 | 10000 | 2.4×10^{-5} | 10000 | -6.5960×10^{-5} | 9998.53 |
| 0.000 | 0.001 | 0.000 | 0 | 10000 | 2.5×10^{-5} | 10000 | -6.5275×10^{-5} | 9998.52 |
| 0.000 | -0.001 | 0.000 | 0 | 10000 | 2.5×10^{-5} | 10000 | -6.58247×10^{-5} | 9998.51 |
| 0.000 | 0.000 | 0.005 | -500 | 10000 | -50 | 10000 | -49.9918 | 9997.89 |
| 0.000 | 0.000 | -0.005 | 500 | 10000 | 50 | 10000 | 49.9916 | 9997.86 |
| -0.001 | 0.000 | 0.010 | -100 | 10000 | -100 | 10000 | -99.9631 | 9993.24 |
| -0.001 | 0.000 | -0.010 | 100 | 10000 | 100 | 10000 | 99.9625 | 9993.05 |
| 0.001 | 0.000 | 0.010 | -100 | 10000 | -100 | 10000 | -99.9631 | 9993.24 |
| 0.001 | 0.000 | -0.010 | 100 | 10000 | 100 | 10000 | 99.9625 | 9993.05 |
| 0.000 | -0.001 | 0.010 | -100 | 10000 | -100 | 10000 | -99.9615 | 9992.81 |
| 0.000 | -0.001 | -0.010 | 100 | 10000 | 100 | 10000 | 99.9608 | 9992.62 |
| 0.000 | 0.001 | 0.010 | -100 | 10000 | -100 | 10000 | -99.9627 | 9993.13 |
| 0.000 | 0.001 | -0.010 | 100 | 10000 | 100 | 10000 | 99.9621 | 9992.94 |

Table 4.4.: Comparison of the results of FFTM and direct solver

| Coordinates | | | Direct Solver | | Fast Multipole Solver | |
|-------------|-------|-------|-------------------------|-------------------------|-----------------------|-------------------|
| X (m) | Y (m) | Z (m) | Potential (V) | $ \vec{E} $ (V/m) | Potential (V) | $ \vec{E} $ (V/m) |
| 0.4665 | 0 | 0.00 | -48.7695 | 1425.18 | -49.7134 | 1344.29 |
| 0.4665 | 0 | -0.65 | -0.4057 | 2.0560 | -0.7876 | 3.6189 |
| 0.4665 | 0 | 0.65 | -0.4031 | 1.9661 | -0.7855 | 3.7957 |
| 0.2415 | 0 | -1.3 | -48.7695 | 1425.19 | -49.6847 | 1339.16 |
| 0.2415 | 0 | 1.3 | -48.7695 | 1425.19 | -50.7262 | 1329.75 |
| 0.0000 | 0 | -2.5 | 7.1992×10^{-5} | 2.5039×10^{-3} | -0.03211 | 0.08453 |
| 0.0000 | 0 | 2.5 | 8.3056×10^{-5} | 2.6406×10^{-3} | -0.03294 | 0.08570 |
| 0.1325 | 0 | -1.6 | -49.1113 | 1342.70 | -49.5311 | 1330.65 |
| 0.1325 | 0 | 1.6 | -49.0822 | 1336.61 | -49.5455 | 1322.34 |
| 0.3325 | 0 | -1.05 | -49.0751 | 1352.97 | -49.6051 | 1330.62 |
| 0.3325 | 0 | 1.05 | -49.0991 | 1357.98 | -49.5915 | 1337.72 |
| 0.4665 | 0 | -0.3 | -49.1128 | 1323.86 | -49.3854 | 1311.65 |
| 0.4665 | 0 | 0.3 | -49.0768 | 1316.47 | -49.3498 | 1304.21 |
| 0.0850 | 0 | -1.73 | -24.7573 | 636.05 | -24.8956 | 634.47 |
| 0.0850 | 0 | 1.73 | -24.2528 | 617.92 | -24.3947 | 617.14 |
| 0.0380 | 0 | -0.92 | -0.05121 | 0.04634 | -0.04534 | 0.07134 |
| 0.0380 | 0 | 0.92 | -0.05009 | 0.03389 | -0.03212 | 0.1621 |
| 0.0000 | 0 | -0.43 | -0.05053 | 0.05529 | 0.02407 | 0.5449 |
| 0.0000 | 0 | 0.43 | -0.05095 | 0.05687 | 0.03075 | 0.5806 |

As can be seen in table 4.4, the value calculated with the fast multipole solver can differ up to 5% in the high field region and can even be 40 times higher in the low field region. The effect of this inaccuracy on the trajectory of the ions will have to be investigated in the future.

4.1.4. Computation of Magnetic Fields with the Zonal Harmonic Expansion

The magnetic field of an axially symmetric coil or magnetic material system can be computed by expansion of the central and remote zonal harmonics, using the Legendre polynomials [Glü11]. This method can be 100-1,000 times faster than the more widely known elliptic integral method and is more general than the similar radial series expansion.

Let us take as an example a simple cylindrical magnet with radii R_{\min} and R_{\max} beginning in Z_{\min} and ending in Z_{\max} . Taking an arbitrary source point z_0 on the symmetry axis, we can define the central zone as the sphere of radius ρ_{cen} defined as the minimal distance to the ends of the magnet. We can as well define the remote zone as the sphere of radius ρ_{rem} defined as the maximal distance the ends of the magnet (figure 4.2). The magnetic field between the two regions will be computed with the elliptic integral method.

In the central region, we can express the magnetic field in term of a zonal harmonic expansion:

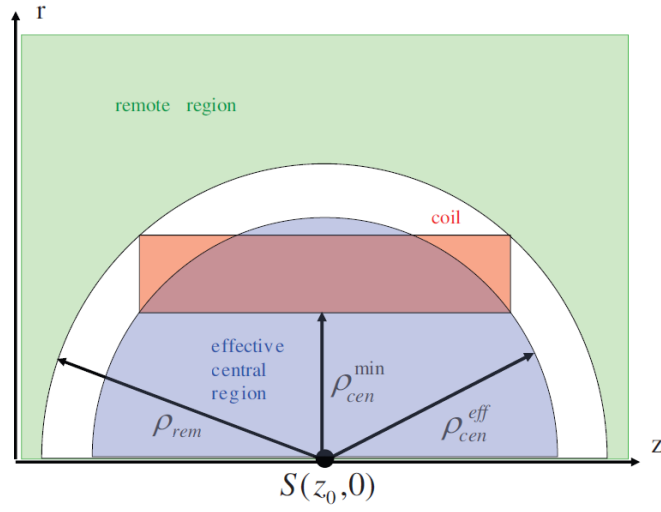


Figure 4.2.: The central and remote region of a coil for the zonal harmonic expansion [Glü11]

$$B_z = \sum_{n=0}^{\infty} B_n^{cen} \left(\frac{\rho}{\rho_{cen}} \right)^n P_n(\cos(\theta)), \quad (4.27)$$

$$B_r = -\sin(\theta) \sum_{n=1}^{\infty} \frac{B_n^{cen}}{n+1} \left(\frac{\rho}{\rho_{cen}} \right)^n P'_n(\cos(\theta)). \quad (4.28)$$

In the remote region, we can express the magnetic field in term of zonal harmonic expansion as follows:

$$B_z = \sum_{n=2}^{\infty} B_n^{rem} \left(\frac{\rho}{\rho_{rem}} \right)^{n+1} P_n(\cos(\theta)) \quad (4.29)$$

$$B_r = \sin(\theta) \sum_{n=2}^{\infty} \frac{B_n^{rem}}{n} \left(\frac{\rho}{\rho_{cen}} \right)^{n+1} P'_n(\cos(\theta)) \quad (4.30)$$

The coefficients B_n^{cen} and B_n^{rem} are called the expansion coefficients.

For a simple current loop of radius R and coordinate Z (figure 4.3), we know from the Biot-Savart's law that the magnetic field along the symmetry axis is:

$$B_0(z) = \frac{\mu_0 I R^2}{2d_z^3} \quad \text{with } d_z = \sqrt{R^2 + (z - Z)^2} \quad (4.31)$$

The corresponding expansion coefficients are:

$$B_n^{cen} = \frac{\mu_0 I R^2}{2\rho_s^3} \left(\frac{\rho_{cen}}{\rho_s} \right)^n P'_{n+1}(\cos(\theta)), \quad (4.32)$$

$$B_n^{rem} = \frac{\mu_0 I R^2}{2\rho_{rem}^3} \left(\frac{\rho_s}{\rho_{rem}} \right)^{n-2} P'_{n-1}(\cos(\theta)). \quad (4.33)$$

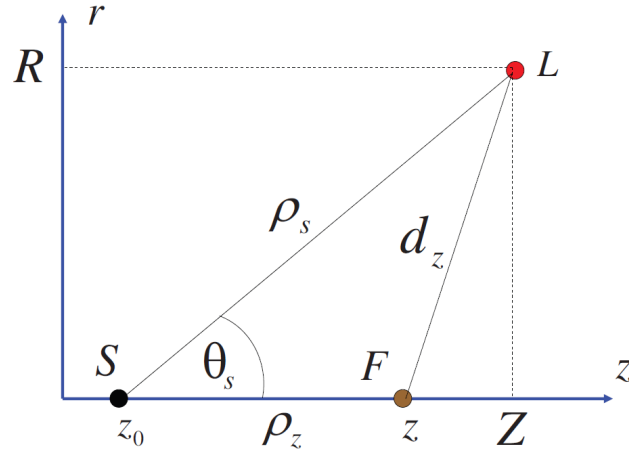


Figure 4.3.: Zonal Harmonic expansion for a simple loop [Glü11]

In order to calculate the coefficients for a cylindrical magnet, we then only have to interpret it as a sum of the current loops. It allows us to define the expansion coefficient as an integral of the coefficient of each loop over the whole magnet:

$$B_n^{cen} = \int_{R_{min}}^{R_{max}} \int_{Z_{min}}^{Z_{max}} b_n^{cen}(Z, R) dR dZ \quad (4.34)$$

$$b_n^{cen}(Z, R) = \frac{\mu_0 J R^2}{2 \rho_s^3} \left(\frac{\rho_{cen}}{\rho_s} \right)^n P'_{n+1}(\cos(\theta)) \quad (4.35)$$

$$B_n^{rem} = \int_{R_{min}}^{R_{max}} \int_{Z_{min}}^{Z_{max}} b_n^{rem}(Z, R) dR dZ \quad (4.36)$$

$$b_n^{rem}(Z, R) = \frac{\mu_0 J R^2}{2 \rho_{rem}^3} \left(\frac{\rho_s}{\rho_{rem}} \right)^{n-2} P'_{n-1}(\cos(\theta)). \quad (4.37)$$

For a system composed of several magnets, we define the central zone as the sphere of radius ρ_{cen} defined as the minimal distance to the ends of the magnets. We define as well the remote zone as the sphere of radius ρ_{rem} defined as the maximal distance the ends of the magnets (figure 4.4).

In order to minimize the regions where the magnetic field will be calculated with the elliptic integral method, we can define several source points to cover the system with several central and remote regions.

With the Zonal Harmonics Expansion method, we are even able to compute magnetic fields for systems composed of magnets that do not have the same symmetry axis. We only have to divide our system into symmetry groups, compute the magnetic field for each group in its own coordinate system using the Zonal Harmonics method and then make the sum of the contribution of each group using appropriate coordinate transformations.

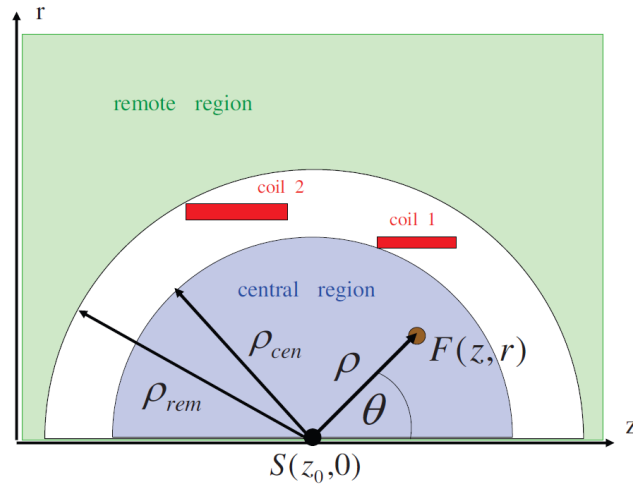


Figure 4.4.: Zonal Harmonic expansion for a 2 magnets [Glü11]

4.2. Electromagnetic Fields within the DPS

The potential and electromagnetic fields in the DPS were calculated with the previously presented program KEMField. The results were computed thanks to two routines derived from the *SimpleElectricFieldCalculator* and *SimpleMagneticFieldCalculator* programs. These programs only use the *field* part of the Kassiopeia configuration file (see 6.1) to work.

In order to compute the electromagnetic field of our system, we have to precise the electromagnetic configuration of our system. This can be made in the geometry file or a separated file. In every case, the following commands have to be put inside the <geometry> tags.

```

1 <electrostatic_dirichlet
2   name="reflexion_electrode"
3   surfaces="DPS/FT-ICR_right/FT-ICR_end_electrode"
4   value="{100.}"
5 />
6

```

This command set a 100 V potential to the geometry element FT-ICR_end_electrode.

```

1 <electromagnet
2   spaces="dps2f_magnet_assembly/dps2f_left_compensation_coil_1"
3   current="82"
4   scaling_factor="4287"
5   direction="counter_clockwise"
6 />
7

```

This command set an 82 A current going in the counter clockwise direction within the 4287-turn wire corresponding to the dps2f_compensation_coil_1 geometry element.

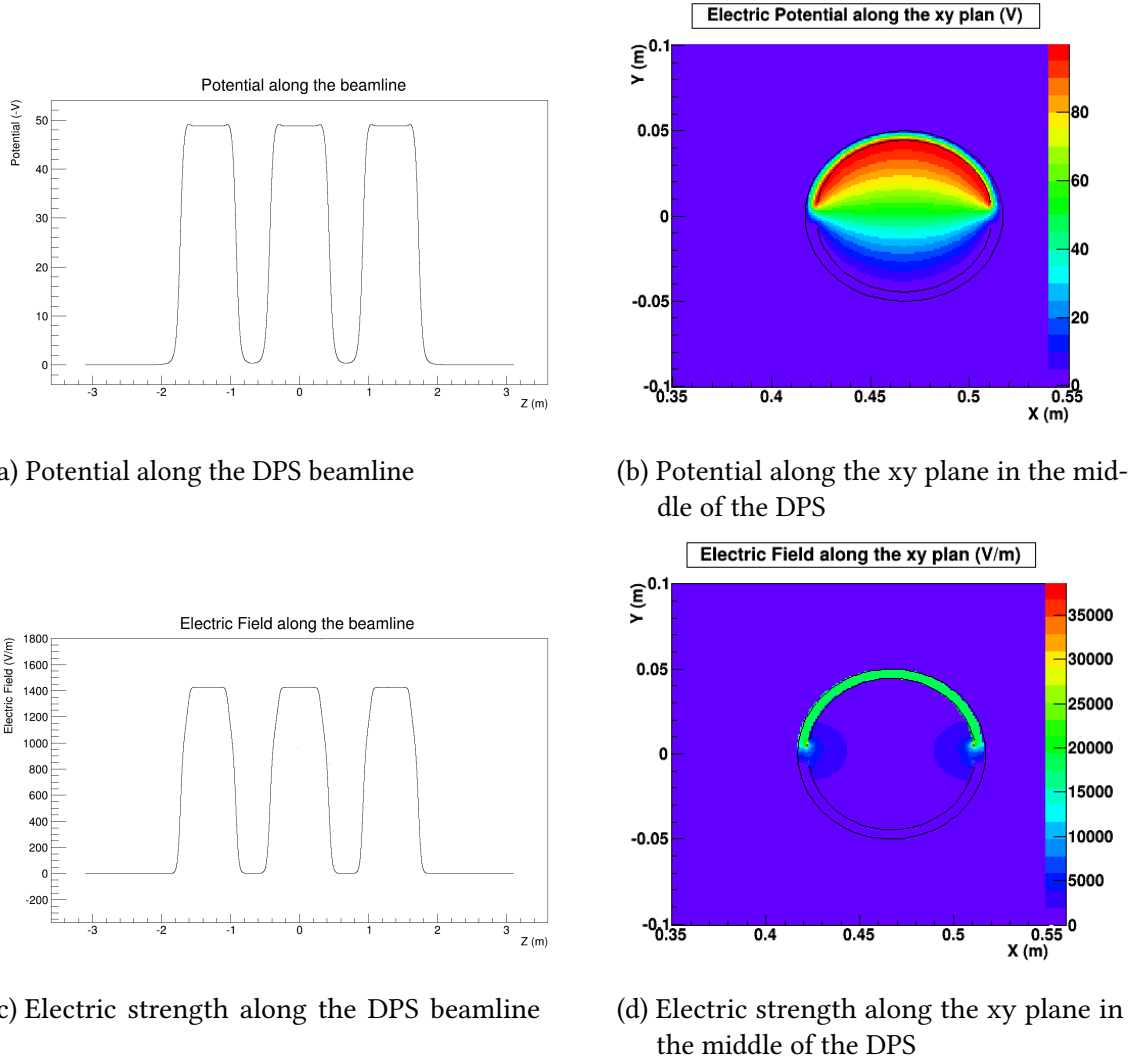


Figure 4.5.: Potential and electric field in the DPS

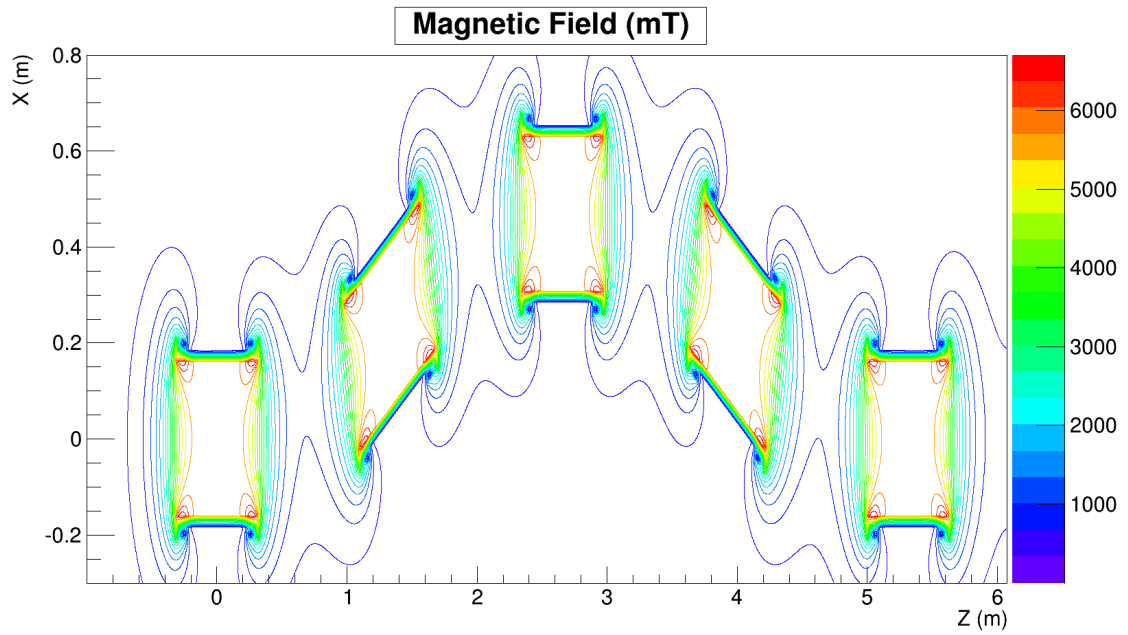
4.2.1. Non-axial Electric Fields

The potential and electric field calculated for the DPS are presented in figure 4.5.

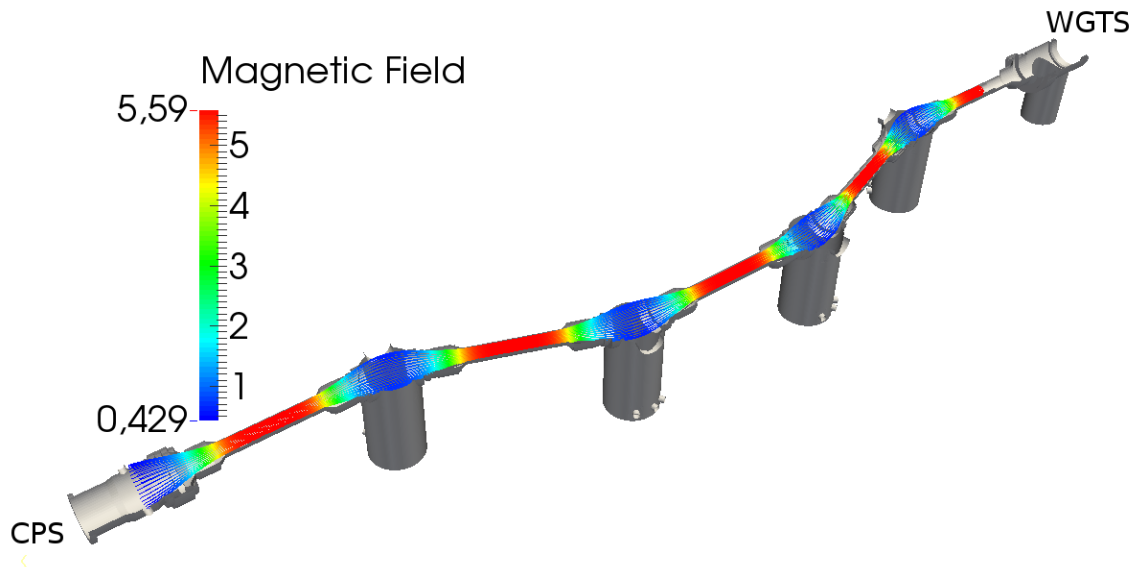
The high potential/field regions than can be seen on figure 4.5a and 4.5c are the electrode regions of the DPS. As the azimuthal dimension of the electrode is far bigger as its thickness, we can spot on figure 4.5d the well-known edge effect as being the very high field regions.

4.2.2. Magnetic Field

The magnetic field in and around the DPS in presented in figure 4.6a. We can easily spot on this graph the coils, as well as their border, as being the high gradient regions. As expected the high field region can be found in the middle of the coils, whereas the region between two coils has a lower field. One can also remark that all the coils create the same field as they are identical. With a simulation, we also were able to compute the flux tube



(a) Magnetic field along the xz plane in and around the DPS



(b) 191 T.cm² flux tube in the DPS

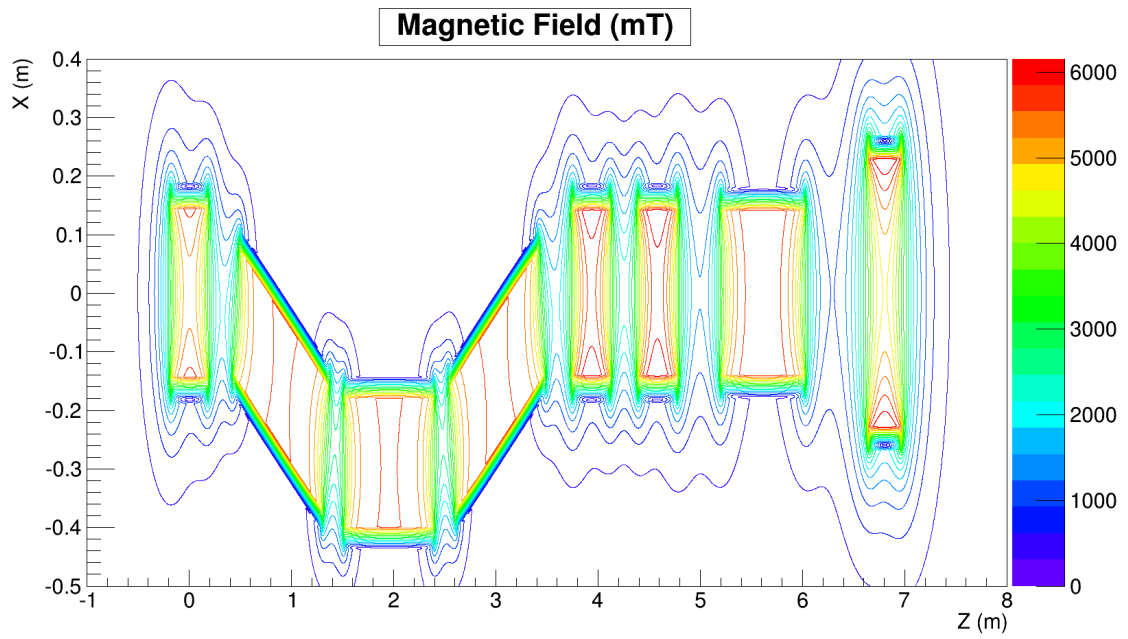
Figure 4.6.: Magnetic configuration of the DPS

corresponding to a 191 T cm² flux in the DPS. The result of this simulation can be seen in figure 4.6b. We can find again the same pattern on this plot as on the above one.

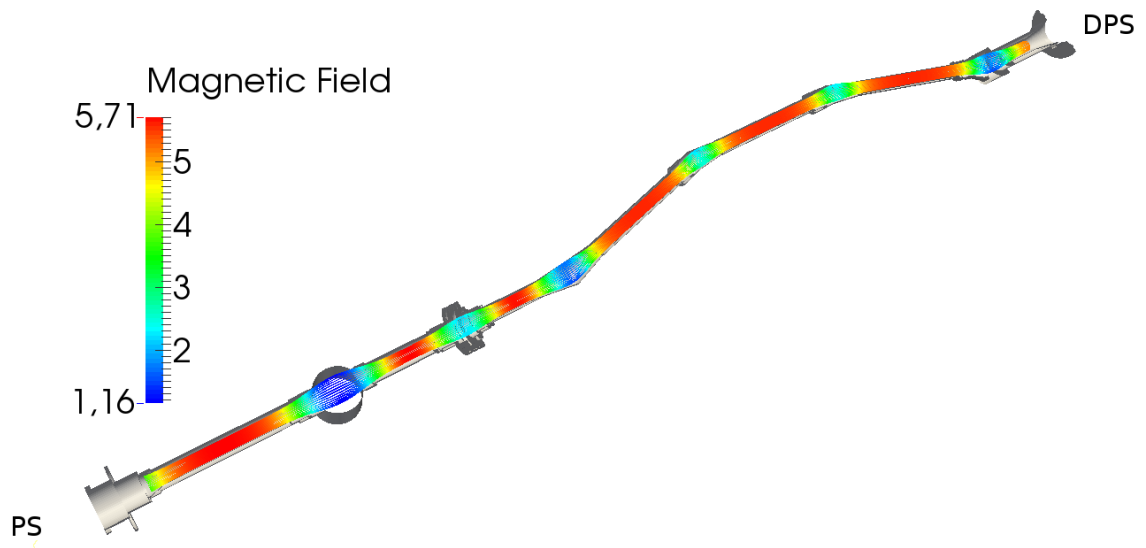
4.3. Magnetic Field computation within the CPS

As for the DPS, the magnetic field in and around the CPS as well as the flux tube have been computed. The corresponding graphics are figures 4.7a(a) and 4.7a(b). Once again we can find the high field gradient region at the border of the coils. We can see that the CPS coils are not the same, which induced a different field for each one. However, the field decrease quickly by half an order of magnitude between two coils.

In the course of this section have been compared the two most important field solver of KEMField, the direct solver and the fast multipole solver, in term of speed and precision. We found as expected the fast multipole solver to be faster but less precise. We also computed the electrostatic configuration of the DPS with the direct solver as well as the magnetic configuration of the design DPS and of the design and as-built CPS. This now allows us to compute the margin between the flux tube and the geometry as well as to make a simulation of particles in this sections.



(a) Magnetic field along the xz plane in and around the CPS



(b) 191 T.cm² flux tube in the CPS

Figure 4.7.: Magnetic configuration of the CPS

5. Evaluation of flux tube margins in the CPS/DPS beamtubes

This chapter deals with the computation of the flux tube geometry in both DPS and CPS with Kassiopeia and our ability to measure the distance between those flux tubes and the geometric boundaries of our setup. This calculation is of particular importance in the KATRIN experiment to prevent the loss of particles in the transport section because of collisions with it. The Distance Tester tool we created to calculate this distance will be introduced in section 5.1. In order to be able to compute this distance in a reasonable amount of computation time, we had to make some simplifications with respect to the real geometry. Some of them were already shortly motivated in section 3 but we will expand the list in section 5.2. Finally, the results of the calculation will be presented and discussed in section 5.3.

5.1. Distance Testing and Margin Computation with Kassiopeia

The principle of the distance testing is simple. For Kassiopeia, we created a terminator which measures the distance between the current point and the surfaces given as arguments. This terminator works as follows:

- At the creation of the terminator, we pass as arguments the surfaces we want to measure the distance to.
- At each step of the simulation, we compute the nearest point to the current point for each surface.
- We calculate the distance between these points and the current point.
- The distance saved is the smallest distance computed.
- If the distance is smaller than the one passed as an argument at the creation of the terminator, a termination signal is sent to the simulation.

We also attached a function to the terminator in order to be able to extract the minimal distance at each step to the output file.

This distance terminator allows us to compute the margin between the flux tube and our geometry using the flux tube simulation mentioned in sections 4.2.2 and 4.3. The distance was added as an output parameter, and it allowed us to compute the aforementioned margin as well as the distance to the center of the beam line as a reference.

5.2. Approximations Used for the Distance Measurement in the DPS/CPS

In order to achieve a compromise weighing computation time against precision, the Distance Tester tool described in the previous section makes use of the following approximations:

- The pump ports using the port housing surface were not added to the terminator as the way they are created conflicts with the distance testing.
- The DPS pump ports were modeled as described in section 3.2: they are composed of two port housings surface in order to produce the inner and outer ports. The caps at both ends of the port were also given up as they will not interact with the electrons (figure A.4 in appendix).
- The clips, the screws and their holes were not implemented to the geometry, as they are punctual elements and can be expected to influence the electron flux only marginally.
- The bellows were simplified as mentioned in section 3.2, as their real, more complex geometry is irrelevant for the investigation at hand.
- The fixation elements were also not added as they are positioned outside of the beamtube.
- The small cut on the outer border of the DPS flange (figure B.10 in appendix) was not implemented as it does not contribute to the distance.
- The design of the cold valve was simplified to the best with respect to the drawings at our disposal (figure B.3 in appendix).
- As already mentioned in section 3.3, the first pump port of the CPS (figure B.4 in appendix) was simplified as a simple cut cylinder in order to respect the asymmetry of the element. Its end cup was symmetrized and integrated to the second beamtube.
- The electron shield has been simplified as mentioned in section 3.3: the holes pierced in it as well as the empty part comprised between it and the beamtube have not been implemented since they will not interact with the electron flux.
- As mentioned in section 3.3, the heating and cooling circuits were not implemented.
- The cones of the CPS beamtubes (figure B.9 in appendix) have been simplified as mentioned in section 3.3 in order to be modeled by a beam element.
- Already mentioned too, the second CPS pump port (figure B.7 in appendix) had to be simplified to be modeled with a port housing surface. The lateral port was given up as it is too close from the other to be modeled with a port housing surface. The upper part of the pump port was also given up as it will not interact with the electrons.

- The first and last DPS pump ports were modeled as mentioned in section 3.2 from CAD models rather than from technical drawings.
- As described in section 3.2.1, the DPS dipole electrodes (figure A.9 in appendix) were modeled with shell surfaces as half cylinders completed with a half cut cone at each end.
- The DPS FT-ICR modules (figure A.7 in appendix) were modeled as a bi-cylindrical element and their electrodes were symmetrized as mentioned in section 3.2.
- The precision of our geometric model is 10^{-4} m for the dimensions and 0.1° for the angles.

5.3. Margins for the DPS/CPS

Having described the method and the geometry of the distance testing in section 5.1 and 5.2, we will now discuss the outcome of the calculations and their implications on the future design of the DPS and CPS details.

5.3.1. Margin for the DPS

The margin for the DPS as designed is presented in figure 5.1. As we can see, with a distance smaller than 2 mm, there could be a collision of the flux tube and the second FT-ICR module if the alignment of the as-built DPS is different from the one of the design DPS. The FT-ICR modules were optimized for the previous DPS design, which had a smaller inner radius together with a smaller flux tube radius. We are currently thinking of removing the second module to replace it with a simpler reflection electrode with a larger radius. Another idea that has been brought up in order to resolve this problem would be to build a new FT-ICR module with a larger radius.

5.3.2. Margin for the CPS

We made two calculations for the CPS as we plan to add NEG pumps in the 7th beamtube [Jan15]. The calculation is made with the CPS as built. We observed that the CPS was built with the second magnet shifted by more than 1 mm in the vertical direction. The results corresponding to the calculation without the NEG pumps are presented on figure 5.2. The results with the NEG pumps are presented on figure 5.3.

As can be seen, the only part worth worrying is the 7th beamtube. With 2 mm for the as-built version of the CPS, the margin without the NEG pumps is sufficient but, because of the shift of the second magnet that cannot be compensated, the NEG pumps intercept the flux tube. We are currently investigating a way to rectify the flux tube in order to prevent this collision.

Anyway, the NEG pumps as currently foreseen are too long for the 191 T.cm² flux tube. It is then planned to rectify the design of the NEG pumps with probably less, shorter NEG pumps. This subject has been investigated more in detail in [Jan15].

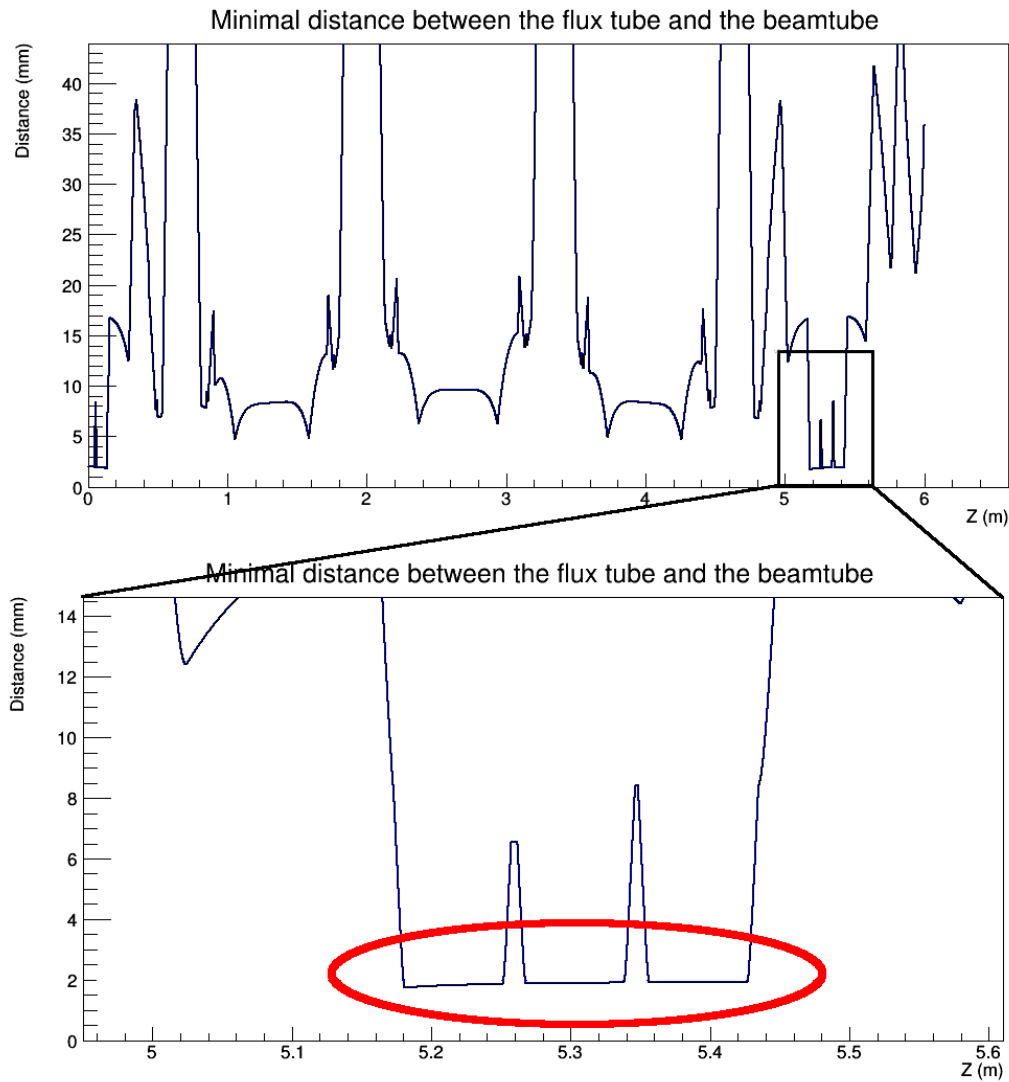


Figure 5.1.: Distance between the flux tube and the beamtube of the DPS with a zoom onto the FT-ICR region

All of the above results underline the usefulness of the Distance Testing tool developed in this work. For the first time, it allows convenient and automatic checks of the flux tube margins throughout all relevant parts of the KATRIN beam line based on the geometry and magnetic field configuration, without having to perform extra calculations case by case. Following the result obtained in the course of this thesis, amendments will be made to the original design of essential components of the transport section according to the elements highlighted above.

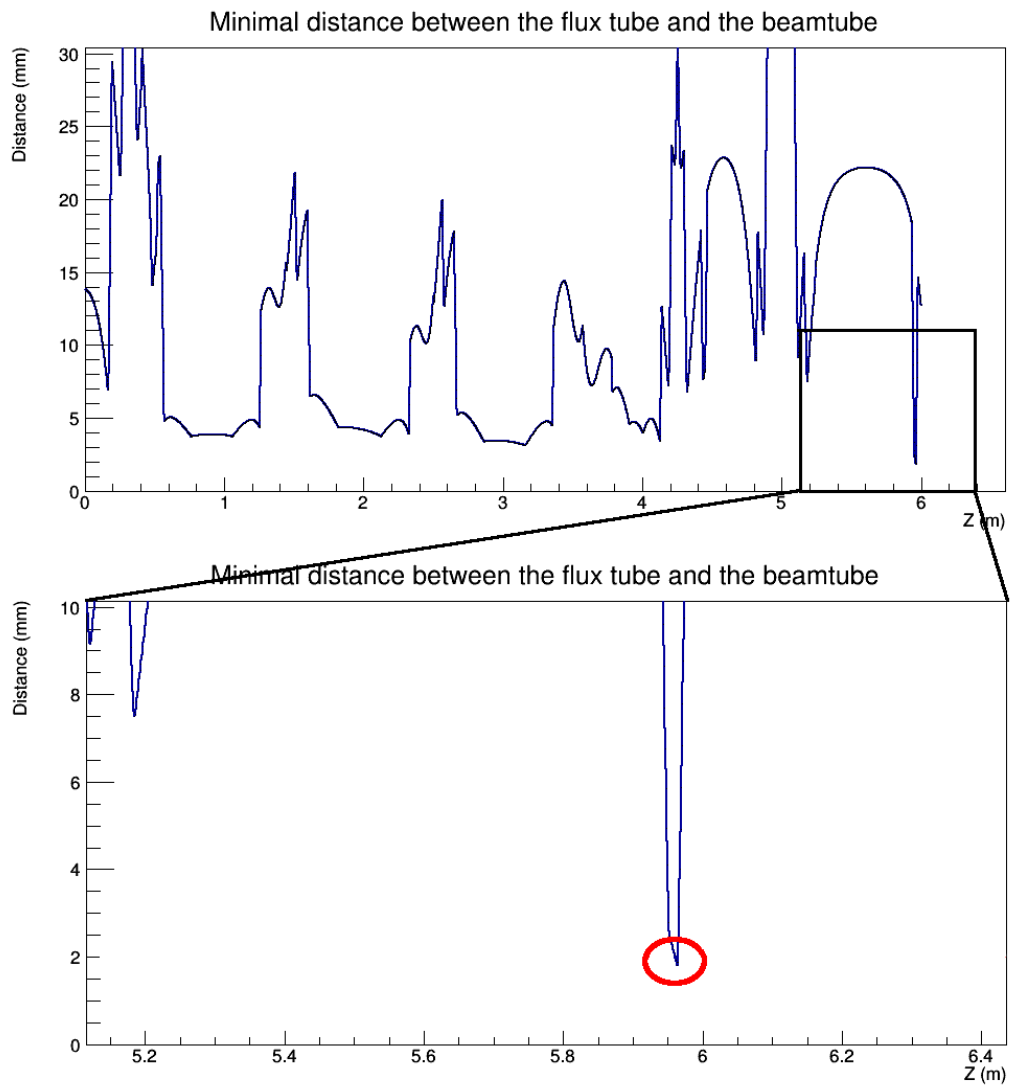


Figure 5.2.: Distance between the flux tube and the beamtube of the CPS with a zoom onto the 7th beamtube region

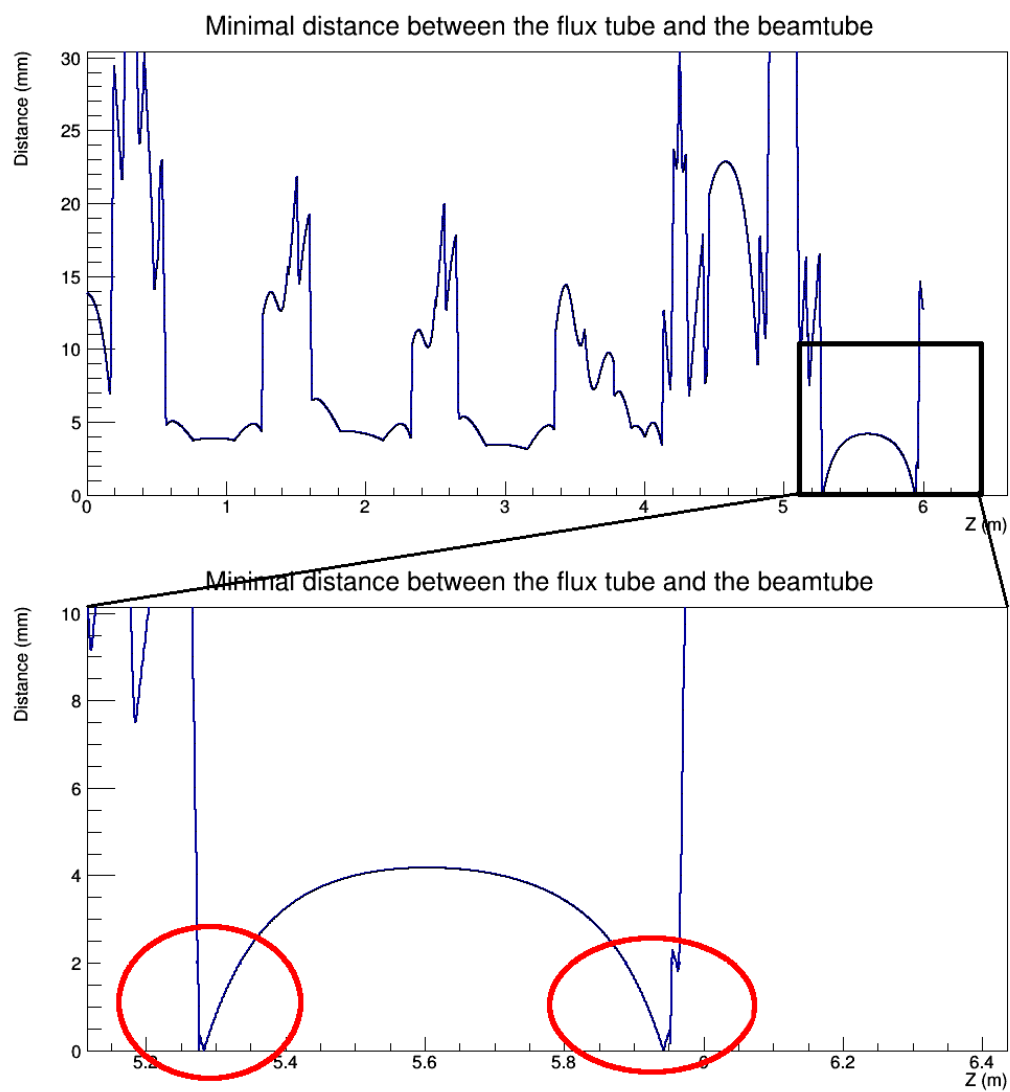


Figure 5.3.: Distance between the flux tube and the beamtube of the CPS with a zoom onto the NEG pumps region

6. Reduction Factor of the Tritium Ions in the DPS

The final goal of this work was to be able to simulate the behavior of the tritium ions issued from the WGTS into the DPS, where they are supposed to be eliminated. This simulation is very important as every tritium ion will induce a contamination of the main spectrometer and a huge source of background as a secondary electrons emitter. Furthermore, once blocked by the reflection electrode, the tritium ions have to be quickly eliminated in the DPS to prevent the accumulation of a space-charge that would create a potential which is strong enough to disturb the neutrino mass measurement or even worse counteract the blocking potential, inducing a fast and irreversible contamination of the main spectrometer. We then have to simulate the behavior of the ions as precisely as possible. This chapter will begin with an introduction into the simulation of particles with Kassiopeia (see 6.1). Our simulation was realized with ions types for which spectra have been identified in [Win11]. This calculation was reproduced in order to find a way to numerically approximate this spectrum for our simulation (see 6.2). The final part of this chapter will present first results of this simulation and their interpretation in terms of reduction factor and time of elimination (see 6.3).

6.1. Tracking of Ions with Kassiopeia

Kassiopeia is the Particle Tracking simulation library for Kasper. It includes bindings to KGeoBag and KEMField, allowing for a single geometry to initialize a complete simulation of various components of KATRIN, as well as VTK ¹ and ROOT ² visualization and output options. Kassiopeia is written primarily in C++, and is comprised of modules for particle generation, simulation of the tritium source, particle tracking in electric and magnetic fields, and particle detection. A variety of different particle generators and different tracking methods are available. Physical processes like synchrotron radiation and scattering can be taken into account. The particle detection module includes backscattering of electrons off the detector surface as well as a comprehensive number of physical phenomena of low-energy electrons in silicon. The user interfaces via XML configuration files and output can be written into ROOT, VTK and text files.

The Kassiopeia configuration files are structured as follows:

- The geometry of the simulation is created. One can add it from an external file:

¹www.vtk.org/

²<http://root.cern.ch>

```
1 <include name="[DPS_config_path]/NonAxialDPSModel.xml"/>
```

or directly write it into the simulation file (see 3.1).

- The simulation part of the file is placed between `<kassiopeia>` tags:
 - It begins with the field calculation. This is the part of the code used by *SimpleElectricFieldCalculator* and *SimpleMagneticFieldCalculator* (see 4.2). The magnetic field calculator is placed between `<ksfield_electromagnet>` tags:

```
1 <ksfield_electromagnet
2   name="DPS_magnetic_field"
3   file="DPSMagnets_test.kbd"
4   spaces="world/DPS_magnets/@magnet_tag"
5 >
6   <zonal_harmonic_field_solver
7     .
8     .
9     .
10  />
11 </ksfield_electromagnet>
```

The file parameter corresponds to the cache file where the parameters of the magnetic field will be saved. The spaces parameter corresponds to the sources of the magnetic field, which means the geometry elements whose magnetic parameters have been defined, that will contribute to the calculation of the magnetic field of the system (see 4.2).

The electric field calculator is placed between `<ksfield_electrostatic>` tags:

```
1 <ksfield_electrostatic
2   name="DPS_electric_field"
3   file="DPSElectrodes_test.kbd"
4   surfaces="world/DPS_world/@electrode_tag"
5   symmetry="none"
6 >
7   <robin_hood_bem_solver
8     .
9     .
10    .
11  />
12
13  <integrating_field_solver
14    use_opengl="false"
15  />
16 </ksfield_electrostatic>
```

The file parameter corresponds to the cache file where the parameters of the magnetic field will be saved. The surfaces parameter correspond to the sources of the electric field, which means the geometry elements whose electric parameters have been defined, that will contribute to the calculation of the magnetic field of the system (see 4.2). One can also define the symmetry for our electric system as being axial, discrete_axial or none. An axial or discrete axial symmetry will allow speeding up calculations. In the simulation described here, however, we were not able to use this option, as the DPS setup lacks a suitable symmetry.

- The generators are placed between **<ksgen_generator_composite>** tags:

```

1 <ksgen_value_formula name="radius" value_min="0.0"
  value_max="3.4e-2" value_formula="sqrt(x)"/>
2
3 <ksgen_value_formula name="energy_T+" value_min="0.0"
  value_max="0.5" value_formula="TMath::Landau
  (19800,0.042,0.00269)"/>
4 <ksgen_generator_composite name="T+_entrance_uniform"
  pid="31">
5   <energy_composite energy="energy_T+"/>
6   <position_cylindrical_composite surface="world/
  entrance_disk" r="radius">
7     <phi_uniform value_min="0." value_max="360."/>
8     <z_fix value="1."/>
9   </position_cylindrical_composite>
10  <direction_spherical_composite surface="world/
  entrance_disk">
11    <theta_spherical angle_min="0." angle_max="50."/>
12    <phi_uniform value_min="0." value_max="360"/>
13  </direction_spherical_composite>
14  <time_composite>
15    <time_fix value="0."/>
16  </time_composite>
17 </ksgen_generator_composite>

```

The pid of a generator defines the generated particle. Various types of particles, such as neutrons or electrons, can be generated. The particle corresponding to the pid 31 is the T^+ ion.

A generator needs an energy, a position, a direction and a time. Each one of these parameters can be user-defined or drawn from a random distribution. A parameter can be defined as:

- * fix, with a defined value
- * spherical, which means it will be uniformly distributed in a segment of a sphere

- * formula, which means it will be distributed according to a user-defined PDF
- * gauss, which means it will be distributed according to a Gaussian of defined parameters
- * list, with a given list of values
- * cylindrical, which means it will be uniformly distributed in a segment of a cylinder
- * set, with defined limits and number of elements
- * uniform, which means it will be uniformly distributed between the defined limits

Our energy is distributed according to the tritium ion spectrum approximated in 6.2. Our radius is distributed to the approximation used for the simulation of the KATRIN experiment. The direction is restricted into a cone of 50° of aperture corresponding to the angular selectivity of the WGTS.

- We must choose a method to compute the trajectory out of the following options:
 - * adiabatic, which make uses of the *adiabatic guiding center* approximation that only considers the motion of the charged particle along the magnetic field line without computing the exact cyclotron trajectory
 - * exact, which computes the exact trajectory
 - * magnetic, which considers that our particle follow the magnetic field lines
 - * linear, which considers that our trajectory is linear between two steps

We can choose between different integrators, i.e. different Runge-Kutta methods. We can define a step of the trajectory calculation by specifying a fraction of cyclotron turn, an energy loss or an interval of length or time between two steps. We chose to use the exact trajectory as the behavior of the ions inside the dipole field would not be correctly described by the adiabatic or the magnetic trajectory. We chose a step of the trajectory calculation to be 1/64th of a cyclotron turn.

- We can implement the particle to interact with other particles or a material. The two main types of interaction in Kassiopeia are scattering and interaction with a surface.

```
1 <ksint_scattering name="int_scattering" split="true">
2 <density_constant temperature="300." pressure="3.e0"/>
3 <calculator_constant cross_section="1.e-18"/>
4 </ksint_scattering>
5
6 <ksint_surface_diffuse name="int_surface_diffuse"
  probability=".3" reflection_loss="0." transmission_loss="
  1."/>
```

For the scattering, we have to specify the density of the other element and the cross-section. For the surface interaction, we have to specify the probability to cross the surface and the energy lost in case of transmission and reflection. We did not use any interaction for our simulation as our ions are supposed to propagate undisturbed except by the dipole field.

- The navigator is used to verify if we are crossing surfaces or leaving the current space to enter another one. We can define a tolerance to verify if we do this at the next step when the distance to the geometry element is smaller than the tolerance.
- We can define a variety of terminators, whose purpose is to stop the simulation for this particle. We can define a terminator for a geometry element, for a maximal or a minimal value of a parameter, or for a maximal number of turns to consider the particle to be trapped.
- The writers define in which format will be made the output file.

```
1 <kswrite_root name="write_root_T+" base="
    DPSSimulation_direct_64_T+.root"/>
2 <kswrite_vtk name="write_vtk_T+" base="
    DPSSimulation_direct_64_T+.vtp"/>
```

Kassiopeia can create output in Paraview ³, ROOT and text format. The base parameter corresponds to the name of the output file.

- The outputs belong to two main categories: the step output and the track output.

```
1 <ks_component_member name="
    component_track_initial_particle" field="initial_particle"
    parent="track"/>
2 <ks_component_member name="
    component_track_final_particle" field="final_particle"
    parent="track"/>
3 <ks_component_group name="component_track_world">
4   <component_member name="creator_name" field="
    creator_name" parent="track"/>
5   .
6   .
7   .
8 </ks_component_group>
9
10 <ks_component_member name="
    component_step_final_particle" field="final_particle" parent="
    step"/>
```

³<http://www.paraview.org>

```

11 <ks_component_member name="efield" field="electric_field"
    parent="component_step_final_particle"/>
12 <ks_component_group name="component_step_world">
13   <component_member name="step_id" field="step_id"
    parent="step"/>
14   .
15   .
16   .
17 </ks_component_group>
18
19 <ks_component_member name="
    component_step_final_position" field="position" parent="
    component_step_final_particle"/>
20 <ks_component_member name="
    component_step_final_polar_angle_to_b" field="
    polar_angle_to_b" parent="component_step_final_particle"/
    >
21
22 <ks_component_member name="electric_strength" field="
    magnitude" parent="efield"/>

```

At the beginning, we have to create a component_member for the particle at each step and the particle in its initial and final state. We can also create component_member for the Paraview output. A component_group is a list of observables that will be printed to the output file. We define one for the output for each step and one for the output for each track. The field corresponds to desired information. The parent corresponds to the object which owns the information.

- All the names we created so long are finally put to use in this section. We have to create here the architecture of our simulation.

```

1 <ksgeo_space name="space_world" spaces="world">
2   <command parent="write_root_T+" field="add_track_output
    " child="component_track_world"/>
3   <command parent="write_root_T+" field="add_step_output"
    child="component_step_world"/>
4   <command parent="write_vtk_T+" field="set_step_point"
    child="component_step_final_position"/>
5   <command parent="write_vtk_T+" field="set_step_data"
    child="electric_strength"/>
6   <command parent="root_terminator" field="add_terminator
    " child="term_min_z"/>
7   <command parent="root_terminator" field="add_terminator
    " child="term_max_z"/>

```

```

8  <command parent="root_terminator" field="add_terminator
   " child="term_min_distance"/>
9  <command parent="root_terminator" field="add_terminator
   " child="term_max_steps"/>
10 <geo_surface name="surface_entrance" surfaces="world/
    entrance_disk">
11   <command parent="root_terminator" field="
    add_terminator" child="term_entrance_death"/>
12 </geo_surface>
13 <geo_surface name="surface_exit" surfaces="world/
    exit_disk">
14   <command parent="root_terminator" field="
    add_terminator" child="term_exit_death"/>
15 </geo_surface>
16 <geo_surface name="collision_exit" surfaces="world/
    DPS_world/#">
17   <command parent="root_terminator" field="
    add_terminator" child="collision_death"/>
18 </geo_surface>
19 </ksgeo_space>

```

Everything is placed between `ksgeo_space` tags defining the simulation system. Every simulation element is added with a `command` specifying its name with `parent`, the type of action performed on it with `field` and the object of the action with `child`. We can even create subspaces with special rules with `geo_space` and assign an action to surfaces with `geo_surface`.

- Finally, we only have to specify the parameters of our simulation.

```

1  <ks_simulation
2    run="1"
3    seed="112383"
4    events="2"
5    magnetic_field="DPS_magnetic_field"
6    electric_field="DPS_electric_field"
7    space="space_world"
8    generator="T+_entrance_uniform"
9    trajectory="trajectory_exact"
10   space_navigator="nav_space"
11   surface_navigator="nav_surface"
12   writer="write_root_T+"
13   writer="write_vtk_T+"
14 />

```

The `run` parameter is only an identification number. The `seed` is the one of the random number generator, which will allow us to do the same simulation

or another one with the same parameters, only by changing it. The event parameter denotes the number of times we run the generator.

The tracking of the ions is then a simulation of ions within the DPS with a terminator denoting the collision of an ion on the electrode.

6.2. Energy Spectrum of the Ions in the KATRIN Experiment

In order to generate realistic ions, we had to approximate their exact spectrum. The calculation of the spectrum was made by Alexander Windberger [Win11]. We reproduced his results with a simple ROOT program, which allowed us to fit the histogram with different PDFs. The formulas for the spectrum are the following:

$$w(p_{x,y}) = \left(\frac{1}{\sqrt{2\pi m k_B T}} \right) e^{-\frac{p_{x,y}^2}{2m k_B T}}, \quad w(p_z) = \left(\frac{1}{\sqrt{2\pi m k_B T}} \right) e^{-\frac{(p_z - m \bar{v}_{\text{gas}}(r))^2}{2m k_B T}} \quad (6.1)$$

The program was made as follows:

```

1 double E,px,py,pz;
2 TF1 *fx = new TF1("density_px", "1/sqrt(2*TMath::Pi()*2.8E9*8.6E-5*70)*exp(-x*x
  /(2*2.8E9*8.6E-5*70))",-4E4,4E4);
3 TF1 *fy = new TF1("density_py", "1/sqrt(2*TMath::Pi()*2.8E9*8.6E-5*70)*exp(-x*x
  /(2*2.8E9*8.6E-5*70))",-4E4,4E4);
4 TF1 *fz = new TF1("density_pz", "1/sqrt(2*TMath::Pi()*2.8E9*8.6E-5*70)*exp(-(x-2.8E9
  * [0])*(x-2.8E9*[0])/(2*2.8E9*8.6E-5*70))",-4E4,4E4);
5 TF1 *vgaz = new TF1("gaz_speed", "(-154.59*x*x+169.75)/3E8",0,1);
6 TH1F h("hist","Ion_Energy",1000,0.,0.5);
7 for (int i=0; i<1000000; i++) {
8   fz->SetParameter(0, vgaz->Eval(gRandom->Rndm()));
9   px = fx->GetRandom();
10  py = fy->GetRandom();
11  pz = fz->GetRandom();
12  E = (px*px + py*py + pz*pz)/(2*2.8E9);
13  h.Fill(E);
14 }
15 h.Draw();

```

The example presented here corresponds to T^+ ions, their mass is 2.8×10^9 eV. The numerical values for the gas speed as a function of radius are taken from [Win11]. We currently do not know the temperature of the ions at the end of the WGTS, so the assumed temperature of the tritium ions of 70 K might be modified in future works. The spectra given by the program are presented in figure 6.1.

The typical mean of the distribution is 9.7 meV and with a typical width of 7.75 meV. As the ions get heavier, the mean value of their spectrum gets only a little more energetic. The tritium ions are of very low energy compared to the β -electrons, which have keV energies. However, this still implies that our ions have a speed smaller than one km/s. We tried several usual probability function to fit them and we found the best agreement with

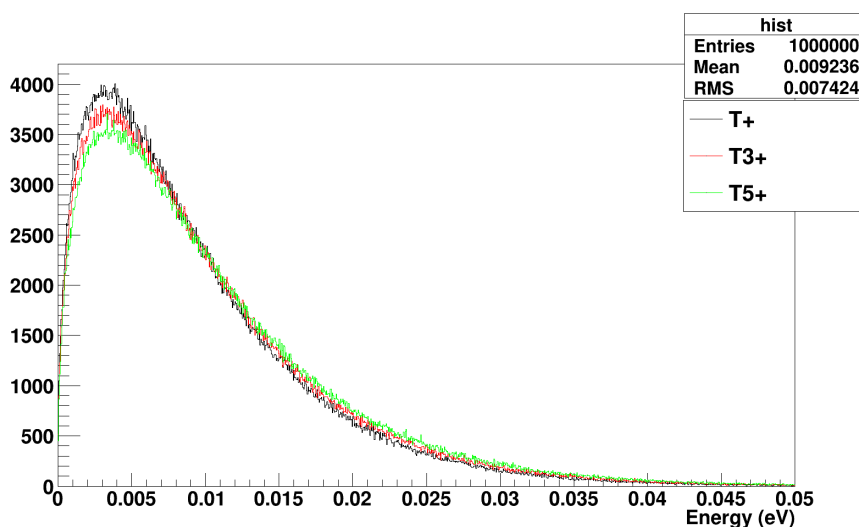


Figure 6.1.: Energy spectrum of the different tritium ions

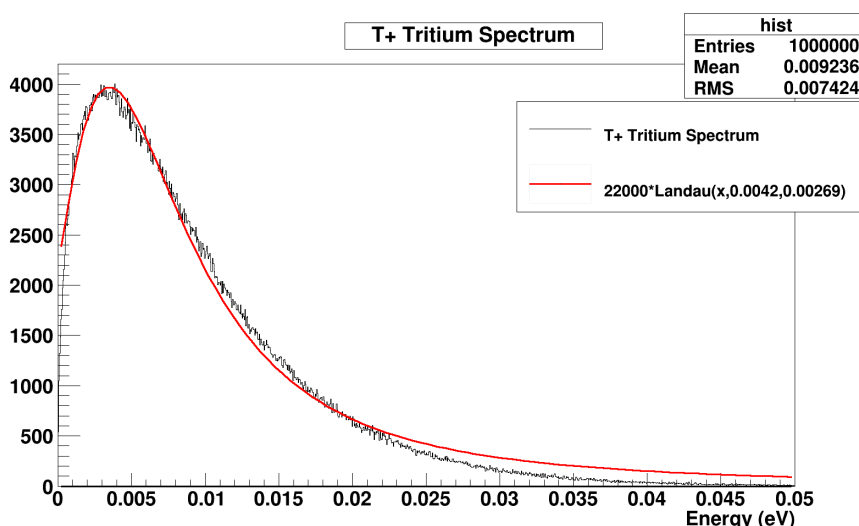


Figure 6.2.: Fit of the T^+ ion energy spectrum with a Landau function

a Landau function scaled to our histogram, as can be seen in figure 6.2. This fit is only a first attempt at approximating our spectrum and would have to be refined in future works.

As can be seen, the typical most probable value of the Landau curve is 4.2 meV and its typical sigma 2.7 meV. As mentioned in 6.1, the fit function will be used in the generator of the Kassiopeia simulation. This will allow us to produce some ions from the end of the spectra that could not be blocked by the reflection electrode.

Apart from the spectrum, the relative concentration of ions in the DPS is also of interest. From [Win11], we get the current and relative concentration (table 6.1).

Table 6.1.: Current and relative concentration of ions at the end of the WGTS

| Ion type | Current (nA) | Flux Φ (ion/s) | Relative concentration |
|----------|--------------|-----------------------|------------------------|
| T^+ | 1 | 6.25×10^9 | 3.5% |
| T_3^+ | 19 | 1.19×10^{11} | 66.7% |
| T_5^+ | 6.5 | 4.06×10^{10} | 22.8% |
| T^- | 2 | 1.25×10^{10} | 7% |

6.3. Reduction Factor and Time of Elimination

As explained in 2.3.3.1 and 3.2.1, we aim to prevent the tritium ions from entering the main spectrometer by means of a reflection electrode placed at end of the DPS coupled with the dipole electrodes placed within the central section of the DPS. This electrode will create a dipole electric field, inducing a $\vec{E} \times \vec{B}$ drift of the tritium ions. The first result of our simulation gives us a reduction factor of $100 \pm 2\%$ and a time of elimination of $(4 \pm 2) \times 10^{-3}$ s, which is an improvement by a factor 3 in comparison to [Win11]. The high uncertainty results from our lack of statistics as we only had the time to simulate 57 ions corresponding to the relative concentration of ions in the DPS in the presence of two T^+ ions. Unfortunately, through the inspection of the trajectory of the ions from the simulation, we discovered that they seem not to behave as expected, as they appear to be trapped in the electrode region. We suppose this phenomenon to be caused by a loss of adiabaticity of the ions or numerical errors in the simulation. This point will have to be investigated in detail in future works.

Given this open issue, we made the following analytic calculation for untrapped ions. The space charge potential created inside the DPS for an uniform density of ions ρ is equal to

$$V = \frac{\rho}{4\epsilon_0} R^2. \quad (6.2)$$

The charge created by a flux ϕ of ions is equal to

$$Q = \phi e \frac{L}{v}, \quad (6.3)$$

with L the length of the DPS and v the speed of the ions. This leads to a density of

$$\rho = \frac{\phi e}{v\pi R^2}. \quad (6.4)$$

The speed of the ions is greater in the electrode region as in the null-potential region. The typical speed of a T_3^+ in the electrode region is 14 km/s, whereas its speed in the null-potential region is typically 300 m/s. By taking into account this phenomenon, we found a density of 3×10^{-8} C/m³ corresponding to a space-charge potential of 1.8 V. This is the result for ions passing one time through the DPS. We can easily see that for trapped ions, we have to multiply these results by the number of times the ions go back and forth in the DPS. We thus have to neutralize the ions quickly in order to prevent a rise of the space-charge potential.

In the course of this chapter, we have developed a simulation to investigate the behavior of tritium ions in the DPS. We calculated the spectra of the different species of ions and found an approximate analytic description required for the implementation into the simulation. We created the simulation and computed first trajectories of tritium ions. We obtained preliminary results for the reduction factor and the time of elimination, however with high uncertainties because of the lack of statistics. This simulation is still to be improved in order to gain speed and precision. Nevertheless we were able to compute analytically the space charge and related potential created by untrapped ions, giving us a first insight on the maximal number of times we can allow the ions to go back and forth in the DPS.

7. Summary and outlook

In the course of this thesis, important milestones for the simulation of the KATRIN components DPS (Differential Pumping Section) and CPS (Cryogenic Pumping Section) have been achieved. The geometry of the new KATRIN transport section has been implemented into the KATRIN simulation and analysis framework *Kasper*. In order to model the geometry of the dipole electrodes of the DPS, a new kind of geometry elements, the shell surfaces, have been implemented, and are currently being used for the model of the DPS and of the inner electrode system of the main spectrometer. After the implementation of the new geometry, electromagnetic fields of the CPS and the DPS have been computed with the program *KEMField*.

The precise computation of magnetic fields in realistic models is indispensable to study the margin between the magnetic flux and the corresponding inner components of CPS and DPS, respectively. For this purpose a special algorithm which computes the flux tube margin with highest reliability and precision has been developed and integrated into the KATRIN simulation program for particle tracking (*Kassiopeia*). As an outcome of this study, tight margins have been identified which will have to be addressed in near future by the corresponding task groups. We discovered that the nominal margin between the flux tube and the second FT-ICR module of the DPS, 2 mm, may be too small to prevent a collision. This particular FT-ICR module was actually supposed to measure the suppression efficiency of tritium ions in the DPS. Unfortunately, the dimensions of the FT-ICR had been optimized for a previous, now obsolete layout of the DPS and do not accommodate the flux tube of the new DPS anymore. Potential solutions to this problem are currently under investigation. For instance, a bigger FT-ICR module could be designed; alternatively, we could remove the module and only leave a simple ring electrode for the reflection. Secondly, we discovered that the 1 mm shift of the second CPS magnet causes a collision between the flux tube and the NEG pumps planned to be installed in the 7th section of the CPS beam tube. However, the margin without the NEG pumps is big enough to prevent the collision. This discovery implies two points that are currently under investigation. First, one has to find a way to shift back the flux tube inside, at least, the 7th section of the CPS to compensate for the shift induced by the second magnet. Secondly, the dimension and number of NEG pumps have to be corrected accordingly to the results of the aforementioned investigation as has been specified in [Jan15].

Finally, a first simulation of the behavior of the tritium ions inside the DPS was performed with *Kassiopeia*. The final goal of this simulation is to reproduce the blocking and elimination of the ions in the DPS in the most realistic way possible. This simulation is important as non-blocked tritium ions reaching the main spectrometer from the DPS will lead to a contamination, and their subsequent decay may yield a huge source of background as a secondary electron emitter. Furthermore, if these ions cannot be eliminated fast enough, there is a risk that they will create space charges, modifying the effective

blocking potential, and a contamination of the main spectrometer could be induced. In order to perform this simulation, the spectrum of the tritium ions was computed from the formulas given in [Win11]. An approximation of this spectrum was found and implemented in our simulation. An improvement of the approximation of the distribution will have to be developed in the future as well as the implementation of the dependence of the gas speed on the radial position [MH12]. The first results of the simulation indicate a complete elimination of the tritium ions (with an efficiency of $100 \pm 2\%$) and a mean time of elimination of 4 ± 2 ms. We also found the density of charge and the space-charge potential created by untrapped ions to be equal to $3 \times 10^{-8} \text{ C/cm}^3$ and 1.8 V, respectively. The results of the simulation have to be put into perspective as the influence of the field solver on the result of the simulation has not yet been investigated. In the future an algorithm counting the number of reversals of the ions in the DPS should be implemented in order to allow further interpretation of the results of the simulation. The simulation currently suffers from a severe lack of statistics owed to the typical very long computation times. Gathering higher statistics by lowering the computation time will be necessary. Taking advantage of the so-called `death_terminator` in order to stop the simulation in the case when ions collide with a surface can speed up the simulation and furthermore yield information on the collision point of the ion with the surface. Once higher statistics will be collected, performing a more precise computation of the space-charge potential within the volume of the new DPS allows us afterwards to improve the understanding of the effect on the measurement of the neutrino mass in more detail.

Appendix

A. The DPS Geometry

Contents

| | |
|------------------------------|----|
| A.1. DPS Beamtube | 71 |
| A.2. DPS Magnets | 74 |
| A.3. DPS Pump port | 77 |
| A.4. FT-ICR module | 80 |
| A.5. DPS Electrode | 82 |

A.1. DPS Beamtube

```
1 <!--Code corresponding to the drawing 316-DWG-0-0027-01-->
2
3 <rotated_poly_loop_surface name="beamtube_middle"
4   rotated_mesh_count="64">
5   <poly_loop>
6     <start_point x="-0.517" y="0.118"/>
7     <next_line x="-0.515" y="0.118"/>
8     <next_line x="-0.515" y="0.092"/>
9     <next_line x="-0.5006" y="0.09"/>
10    <next_line x="-0.5006" y="0.1005"/>
11    <next_line x="-0.475" y="0.1005"/>
12    <next_line x="-0.475" y="0.092"/>
13    <next_line x="-0.433" y="0.092"/>
14    <next_line x="-0.433" y="0.0955"/>
15    <next_line x="-0.324" y="0.0955"/>
16    <next_line x="-0.3087" y="0.0865"/>
17    <next_line x="-0.3087" y="0.08"/>
18    <next_line x="-0.2782" y="0.054"/>
19    <next_line x="0.2782" y="0.054"/>
20    <next_line x="0.3087" y="0.08"/>
21    <next_line x="0.3087" y="0.0865"/>
22    <next_line x="0.324" y="0.0865"/>
23    <next_line x="0.324" y="0.0955"/>
24    <next_line x="0.433" y="0.0955"/>
25    <next_line x="0.433" y="0.092"/>
```

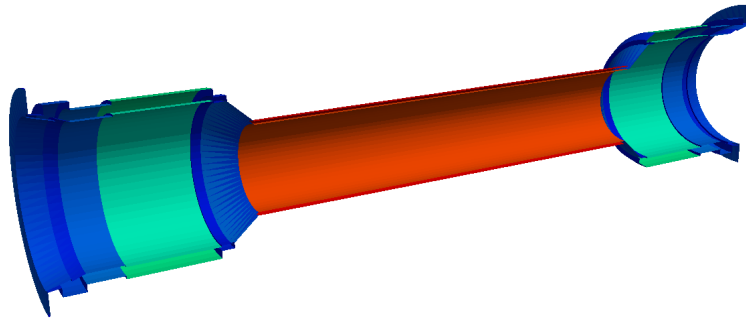


Figure A.1.: Cut of the 3D Geometry of the element beamtube_middle

```

25 <next_line x="0.475" y="0.092"/>
26 <next_line x="0.475" y="0.1005"/>
27 <next_line x="0.5006" y="0.1005"/>
28 <next_line x="0.5006" y="0.09"/>
29 <next_line x="0.515" y="0.092"/>
30 <next_line x="0.515" y="0.118"/>
31 <next_line x="0.517" y="0.118"/>
32 <next_line x="0.517" y="0.09"/>
33 <next_line x="0.490" y="0.083"/>
34 <next_line x="0.490" y="0.0855"/>
35 <next_line x="0.475" y="0.08"/>
36 <next_line x="0.433" y="0.08"/>
37 <next_line x="0.433" y="0.082"/>
38 <next_line x="0.324" y="0.082"/>
39 <next_line x="0.324" y="0.08"/>
40 <next_line x="0.312" y="0.08"/>
41 <next_line x="0.2782" y="0.05"/>
42 <next_line x="-0.2782" y="0.05"/>
43 <next_line x="-0.312" y="0.08"/>
44 <next_line x="-0.324" y="0.08"/>
45 <next_line x="-0.324" y="0.082"/>
46 <next_line x="-0.433" y="0.082"/>
47 <next_line x="-0.433" y="0.08"/>
48 <next_line x="-0.475" y="0.08"/>
49 <next_line x="-0.490" y="0.0855"/>
50 <next_line x="-0.490" y="0.083"/>
51 <next_line x="-0.517" y="0.09"/>
52 <last_line/>
53 </poly_loop>
54 </rotated_poly_loop_surface>

```

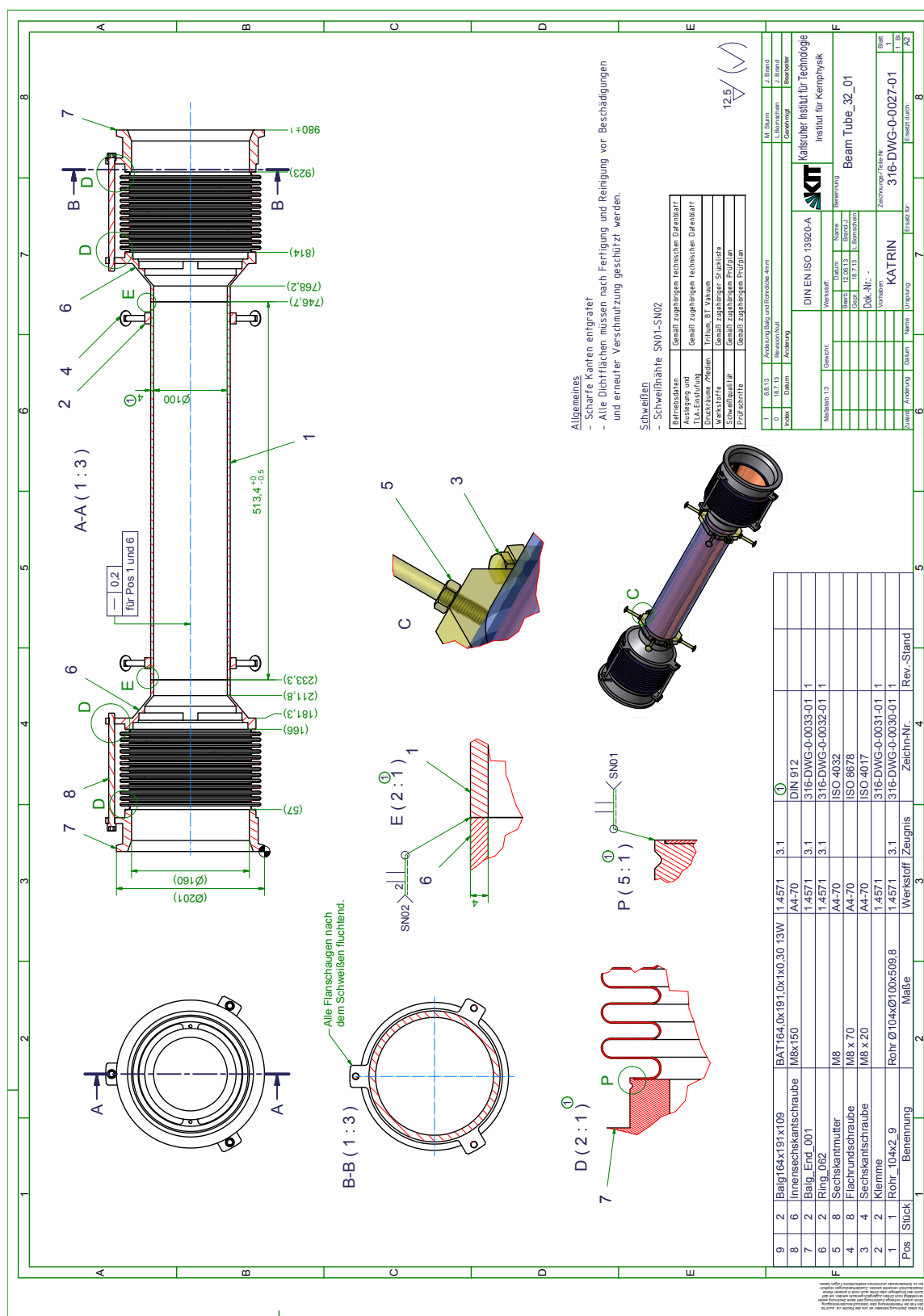


Figure A.2.: Drawing 316-DWG-0-0027-01 corresponding to the middle beamtubes

A.2. DPS Magnets

```

1 Coordinates of a DPS Magnet
2
3 current x_start y_start z_start x_end y_end z_end r_in r_out
4 1.75000000000000e+08 0.00000000000000e+00 0.00000000000000e+00
   -2.43520250000000e+01 0.00000000000000e+00 0.00000000000000e+00
   -2.42715250000000e+01 1.60000000000000e-01 2.11010000000000e-01
5 1.75000000000000e+08 0.00000000000000e+00 0.00000000000000e+00
   -2.48210250000000e+01 0.00000000000000e+00 0.00000000000000e+00
   -2.43520250000000e+01 1.60000000000000e-01 1.86160000000000e-01
6 1.75000000000000e+08 0.00000000000000e+00 0.00000000000000e+00
   -2.49015250000000e+01 0.00000000000000e+00 0.00000000000000e+00
   -2.48210250000000e+01 1.60000000000000e-01 2.11010000000000e-01

```

```

1 <!-- Code of a DPS Magnet -->
2
3 <cylinder_tube_space
4   name="dps2f_compensation_coil"
5   length="0.0805"
6   r1="0.1862"
7   r2="0.2110"
8 />
9
10 <cylinder_tube_space
11   name="dps2f_main_coil"
12   length="0.6300"
13   r1="0.1600"
14   r2="0.1862"
15 />
16
17 <!-- dps2f_1 -->
18
19 <space name="dps2f_left_compensation_coil_1" node="
   dps2f_compensation_coil">
20   <transformation rotation_euler="0,0,0" displacement="0,0,-0.2748"/>
21 </space>
22
23 <!-- dps2f_2 -->
24 <space name="dps2f_main_coil_1" node="dps2f_main_coil">
25   <transformation rotation_euler="0,0,0" displacement="0,0,0"/>
26 </space>
27
28 <!-- dps2f_3 -->

```

```

29 <space name="dps2f_right_compensation_coil_1" node="
    dps2f_compensation_coil">
30   <transformation rotation_euler="0.0.0." displacement="0.0.0.2748"/>
31 </space>
32
33 <!-- magnet_variables -->
34
35 <define name="coil_current" value="82.00"/>
36 <define name="main_coil_turns" value="35314.0"/>
37 <define name="compensation_coil_turns" value="4287.0"/>
38
39 <!-- magnets -->
40
41
42 <electromagnet
43   spaces="dps2f_magnet_assembly/dps2f_left_compensation_coil_1"
44   current="[coil_current]"
45   scaling_factor="[compensation_coil_turns]"
46   direction="counter_clockwise"
47 />
48
49 <electromagnet
50   spaces="dps2f_magnet_assembly/dps2f_main_coil_2"
51   current="[coil_current]"
52   scaling_factor="[main_coil_turns]"
53   direction="counter_clockwise"
54 />
55
56 <electromagnet
57   spaces="dps2f_magnet_assembly/dps2f_right_compensation_coil_1"
58   current="[coil_current]"
59   scaling_factor="[compensation_coil_turns]"
60   direction="counter_clockwise"
61 />

```

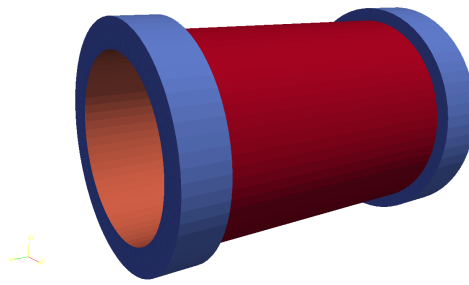


Figure A.3.: 3D Geometry of a DPS magnet

A.3. DPS Pump port

```

1 <!--Code corresponding to the drawing 316-DWG-0-0004-01-->
2
3 <port_housing_surface name="pump_port_extern">
4   <port_housing x1="0." y1="0." z1="-0.174" x2="0." y2="0." z2="0.6055"
      radius="0.165" longitudinal_mesh_count="50" axial_mesh_count="50"
      >
5     <circular_port x="{0.165*cos(10./180.*TMath::Pi())}" y="{0.165*sin
      (10./180.*TMath::Pi())}" z="0" radius="0.118"/>
6     <circular_port x="{0.165*cos(10./180.*TMath::Pi())}" y="{0.165*sin
      (10./180.*TMath::Pi())}" z="0" radius="0.118"/>
7     <circular_port x="0." y="-0.188" z="0." radius="0.076"/>
8     <circular_port x="{0.165/sqrt(2)-0.022}" y="{0.165/sqrt(2)-0.022}" z="
      0.538" radius="0.02"/>
9     <circular_port x="{0.165*sin(15./180.*TMath::Pi())-0.022}" y="{0.165*
      cos(15./180.*TMath::Pi())-0.022}" z="0.538" radius="0.02"/>
10    <circular_port x="{0.165*sin(15./180.*TMath::Pi())+0.022}" y="{0.165*cos
      (15./180.*TMath::Pi())-0.022}" z="0.538" radius="0.02"/>
11  </port_housing>
12 </port_housing_surface>
13
14 <port_housing_surface name="pump_port_intern">
15   <port_housing x1="0." y1="0." z1="-0.174" x2="0." y2="0." z2="0.6055"
      radius="0.161" longitudinal_mesh_count="50" axial_mesh_count="50"
      >
16     <circular_port x="{0.0995*cos(10./180.*TMath::Pi())}" y="{0.0995*sin
      (10./180.*TMath::Pi())}" z="0" radius="0.1085"/>
17     <circular_port x="{0.0995*cos(10./180.*TMath::Pi())}" y="{0.0995*sin
      (10./180.*TMath::Pi())}" z="0" radius="0.1085"/>
18     <circular_port x="0." y="-0.161" z="0." radius="0.076"/>
19  </port_housing>
20 </port_housing_surface>

```

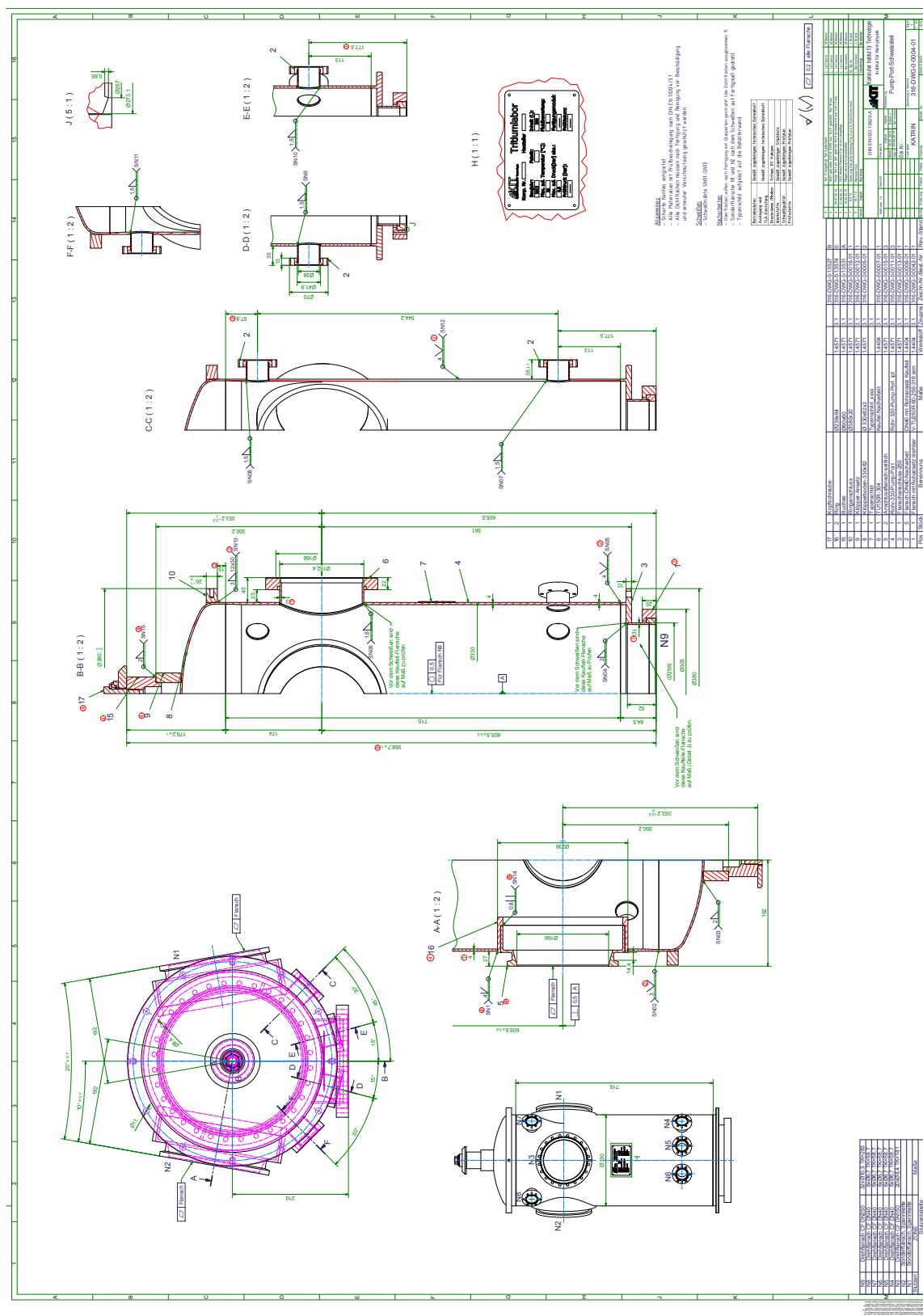


Figure A.4.: Drawing 316-DWG-0-0004-01 corresponding to the middle pump ports

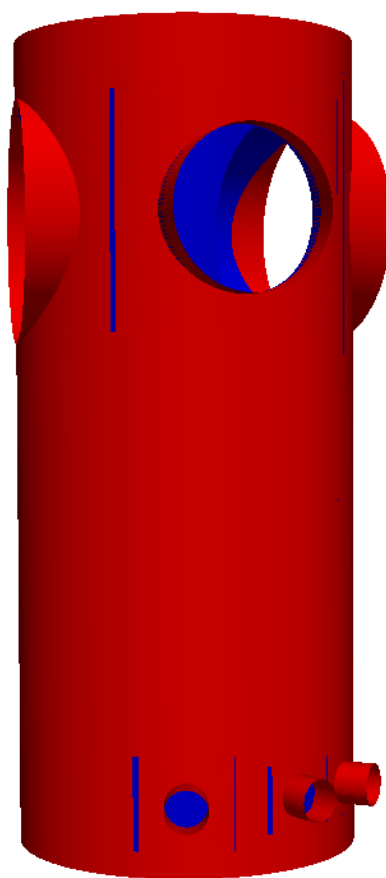


Figure A.5.: 3D Geometry of a DPS pump port

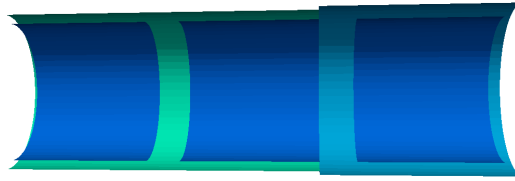


Figure A.6.: Cut of the 3D Geometry of the element FT-ICR

A.4. FT-ICR module

```

1  <!--Code corresponding to the drawing Trap-drawings-2-01-->
2
3  <rotated_poly_line_surface name="fticr_tube">
4    <poly_line>
5      <start_point x="-0.125" y="0.0397"/>
6      <next_line x="0.035" y="0.0397"/>
7      <next_line x="0.035" y="0.0415"/>
8      <next_line x="0.131" y="0.0415"/>
9    </poly_line>
10 </rotated_poly_line_surface>
11
12 <rotated_line_segment_surface name="fticr_electrode">
13   <line_segment x1="-0.035" y1="0.035" x2="0.035" y2="0.035"/>
14 </rotated_line_segment_surface>
15
16 <space name="FT-ICR">
17
18   <surface name="FT-ICR_tube" node="fticr_tube"/>
19
20   <surface name="FT-ICR_entrance_electrode" node="fticr_electrode">
21     <transformation displacement="0,0,-0.087"/>
22   </surface>
23
24   <surface name="FT-ICR_middle_electrode" node="fticr_electrode"/>
25
26   <surface name="FT-ICR_end_electrode" node="fticr_electrode">
27     <transformation displacement="0,0,0.0885"/>
28   </surface>
29
30 </space>

```



Figure A.7.: Drawing Trap-drawings-2-01 corresponding to the FT-ICR module

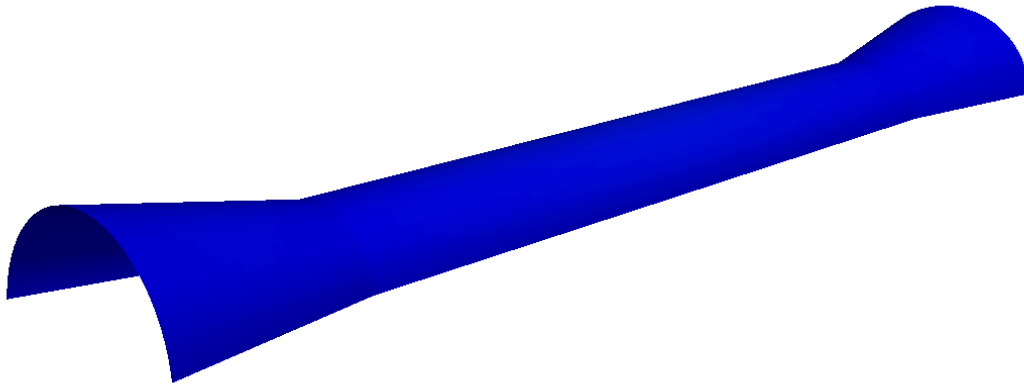


Figure A.8.: 3D Geometry of the element electrode

A.5. DPS Electrode

```
1 <!--Code corresponding to the drawing Muster-->
2
3 <shell_poly_line_surface name="electrode" angle_start="6.5" angle_stop="
  173.5" shell_mesh_count="64" shell_mesh_power="2.7">
4   <poly_line>
5     <start_point x="-0.422" y="0.0694"/>
6     <next_line x="-0.282" y="0.0445" line_mesh_count="32"
      line_mesh_power="2.7"/>
7     <next_line x="0.282" y="0.0445" line_mesh_count="32"
      line_mesh_power="2.7"/>
8     <next_line x="0.422" y="0.0715" line_mesh_count="32"
      line_mesh_power="2.7"/>
9   </poly_line>
10 </shell_poly_line_surface>
```



B. The CPS Geometry

Contents

| | |
|---------------------------------|-----|
| B.1. CPS Magnet | 85 |
| B.2. Cold Valve | 87 |
| B.3. First pump port | 91 |
| B.4. Second pump port | 94 |
| B.5. CPS beamtube | 96 |
| B.6. CPS DPS Flange | 100 |
| B.7. CPS PS Flange | 103 |

B.1. CPS Magnet

```
1 Coordinates of a CPS Magnet
2
3 current x_start y_start z_start x_end y_end z_end r_in r_out
4 1.1568E+08 0.0005 -0.0001 0.3332 0.0005 0.0005 0.6987 0.1432 0.1896
```

```
1 <!--Code of a CPS magnet-->
2
3 <cylinder_tube_space
4   name="cps_coil_1_space"
5   length="0.3655"
6   r1=".1432"
7   r2=".1896"
8 />
9
10 <cylinder_tube_space
11   name="cps_coil_1_space"
12   length="0.3655"
13   r1=".1432"
14   r2=".1896"
15 />
16
17 <define name="cps_coil_current" value="200.00"/>
18 <define name="cps_1_turns" value="9828.0"/>
```

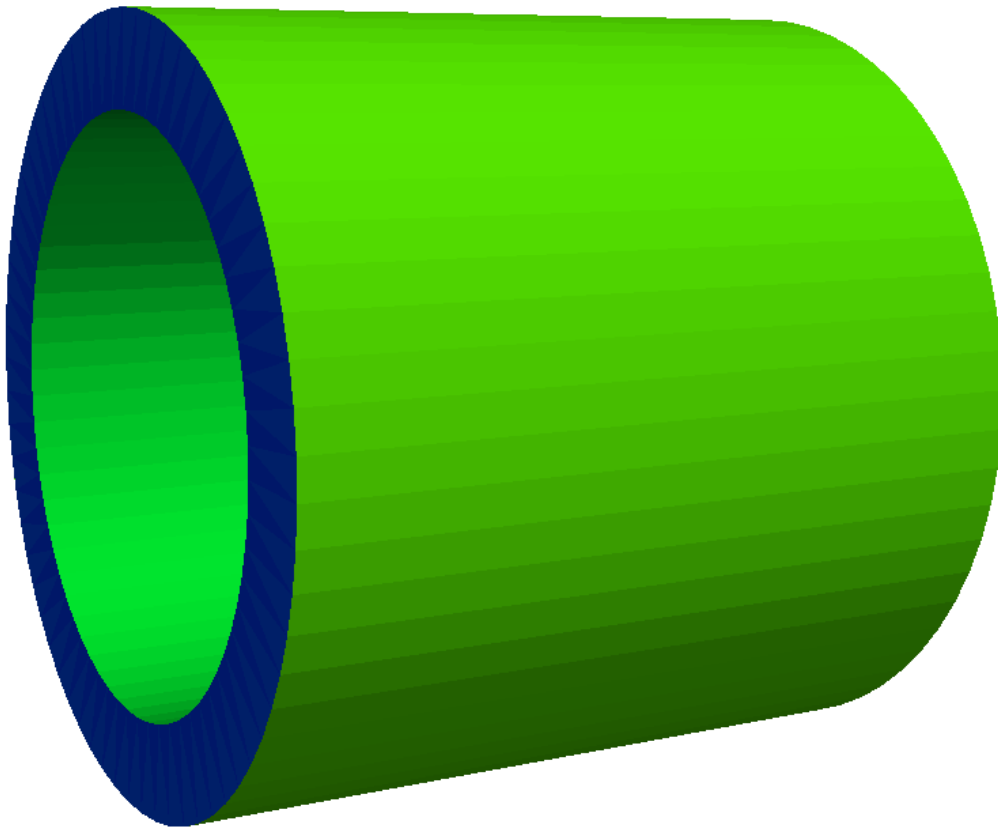


Figure B.1.: 3D Geometry of a CPS magnet

```
19  
20 <electromagnet  
21   spaces="CPS_system_assembly/cps_coil_[index]"  
22   current="[cps_coil_current]"  
23   scaling_factor="[cps_[index]_turns]"  
24   direction="counter_clockwise"  
25 />
```


B.2. Cold Valve

```

1 <!--Code corresponding to the drawing 394903-->
2 <rotated_poly_loop_surface name="cold_gate_surface"
   rotated_mesh_count="64">
3   <poly_loop>
4     <start_point x="-0.1475" y="0.065"/>
5     <next_line x="-0.1335" y="0.065"/>
6     <next_line x="-0.1335" y="0.064"/>
7     <next_line x="-0.1315" y="0.064"/>
8     <next_line x="-0.1315" y="0.065"/>
9     <next_line x="-0.1305" y="0.065"/>
10    <next_line x="-0.1305" y="0.0708"/>
11    <next_line x="-0.0731" y="0.0708"/>
12    <next_line x="-0.0731" y="0.0788"/>
13    <next_line x="-0.0698" y="0.0788"/>
14    <next_line x="-0.0688" y="0.0808"/>
15    <next_line x="-0.0678" y="0.0808"/>
16    <next_line x="-0.0668" y="0.0788"/>
17    <next_line x="-0.0638" y="0.0788"/>
18    <next_line x="-0.0638" y="0.1009"/>
19    <next_line x="-0.0479" y="0.1009"/>
20    <next_line x="-0.0479" y="0.1436"/>
21    <next_line x="-0.0339" y="0.1436"/>
22    <next_line x="-0.0339" y="0.1426"/>
23    <next_arc x="-0.0329" y="0.1416" radius="0.001" right="true" short="
      true"/>
24    <next_arc x="-0.0319" y="0.1426" radius="0.001" right="true" short="
      true"/>
25    <next_line x="-0.0319" y="0.1436"/>
26    <next_line x="-0.0289" y="0.1436"/>
27    <next_line x="-0.0289" y="0.1356"/>
28    <next_arc x="-0.0234" y="0.1411" radius="0.0055" right="false" short="
      true"/>
29    <next_line x="-0.0125" y="0.1411"/>
30    <next_line x="-0.0125" y="0.1426"/>
31    <next_line x="0.0125" y="0.1427"/>
32    <next_line x="0.0125" y="0.1412"/>
33    <next_line x="0.0234" y="0.1412"/>
34    <next_arc x="0.0289" y="0.1357" radius="0.0055" right="false" short="
      true"/>
35    <next_line x="0.0289" y="0.1437"/>
36    <next_line x="0.0319" y="0.1437"/>
37    <next_line x="0.0319" y="0.1427"/>

```

```

38 <next_arc x="0.0329" y="0.1417" radius="0.001" right="true" short="true
    ">
39 <next_arc x="0.0339" y="0.1427" radius="0.001" right="true" short="true
    ">
40 <next_line x="0.0339" y="0.1437"/>
41 <next_line x="0.0479" y="0.1437"/>
42 <next_line x="0.0479" y="0.101"/>
43 <next_line x="0.0639" y="0.101"/>
44 <next_line x="0.0639" y="0.0788" />
45 <next_line x="0.0668" y="0.0788" />
46 <next_line x="0.0678" y="0.0808" />
47 <next_line x="0.0688" y="0.0808" />
48 <next_line x="0.0698" y="0.0788" />
49 <next_line x="0.0731" y="0.0788"/>
50 <next_line x="0.0731" y="0.0708"/>
51 <next_line x="0.1628" y="0.0708"/>
52 <next_line x="0.1628" y="0.065"/>
53 <next_line x="0.1638" y="0.065"/>
54 <next_line x="0.1638" y="0.064"/>
55 <next_line x="0.1658" y="0.064"/>
56 <next_line x="0.1658" y="0.065"/>
57 <next_line x="0.1837" y="0.065"/>
58 <next_line x="0.1837" y="0.0629"/>
59 <next_line x="0.1628" y="0.0629"/>
60 <next_line x="0.1628" y="0.0559"/>
61 <next_line x="0.0681" y="0.0559"/>
62 <next_line x="0.0681" y="0.0569"/>
63 <next_line x="0.0661" y="0.0569"/>
64 <next_line x="0.0661" y="0.0589"/>
65 <next_line x="0.0681" y="0.0589"/>
66 <next_line x="0.0681" y="0.0778"/>
67 <next_line x="0.0671" y="0.0748"/>
68 <next_line x="0.0235" y="0.0748"/>
69 <next_line x="0.0235" y="0.1317"/>
70 <next_line x="0.0047" y="0.1317"/>
71 <next_line x="0.0047" y="0.1058"/>
72 <next_line x="-0.0047" y="0.1057"/>
73 <next_line x="-0.0047" y="0.1316"/>
74 <next_line x="-0.0235" y="0.1316"/>
75 <next_line x="-0.0235" y="0.0748"/>
76 <next_line x="-0.0671" y="0.0748"/>
77 <next_line x="-0.0681" y="0.0778"/>
78 <next_line x="-0.0681" y="0.0588"/>
79 <next_line x="-0.0661" y="0.0588"/>
80 <next_line x="-0.0661" y="0.0568"/>

```

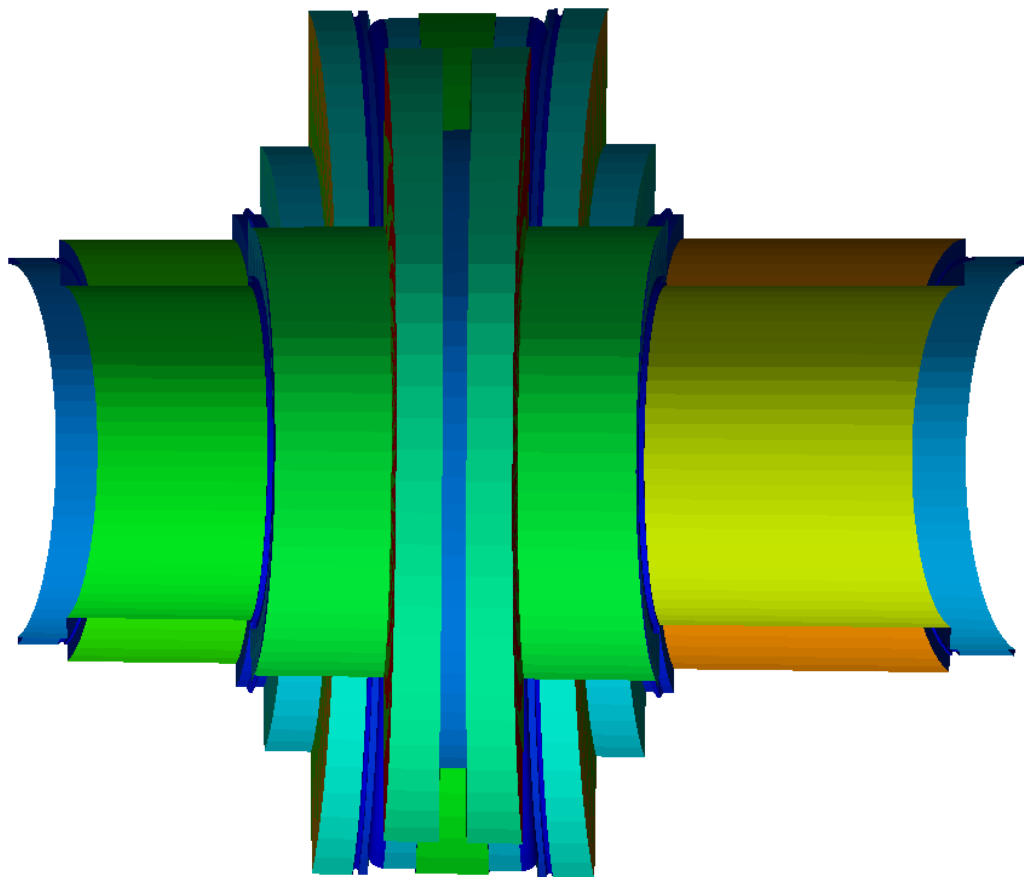


Figure B.2.: Cut of the 3D Geometry of the cold valve

```
81 <next_line x="-0.0681" y="0.0568"/>  
82 <next_line x="-0.0681" y="0.0558"/>  
83 <next_line x="-0.1305" y="0.0558"/>  
84 <next_line x="-0.1305" y="0.0628"/>  
85 <next_line x="-0.1475" y="0.0628"/>  
86 <last_line/>  
87 </poly_loop>  
88 </rotated_poly_loop_surface>
```

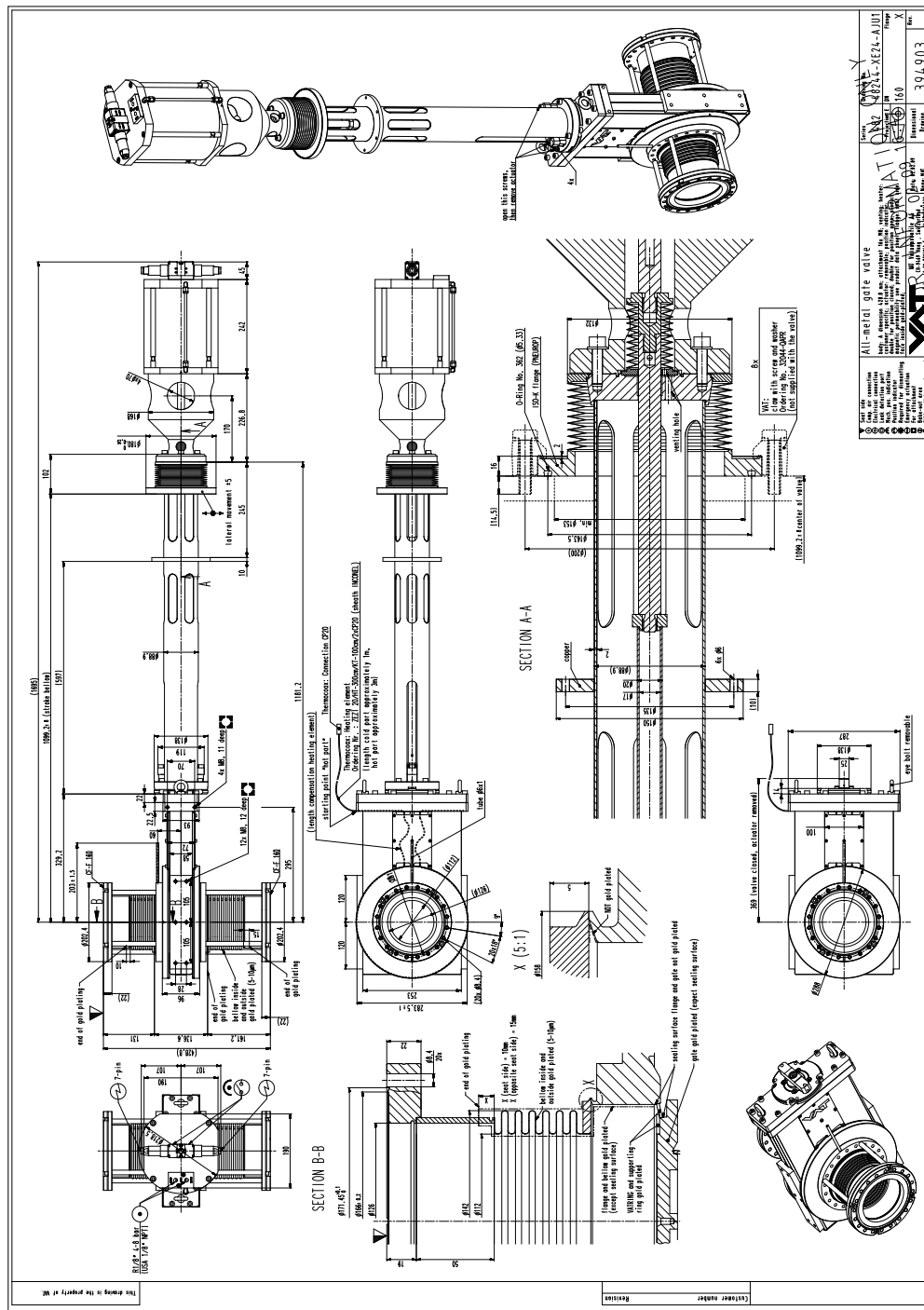


Figure B.3.: Drawing 394903 corresponding to the Cold Valve

B.3. First pump port

```

1 <!--Code corresponding to drawing 688RM12491-->
2
3 <beam_surface name="pump_port">
4   <beam longitudinal_mesh_count="60" axial_mesh_count="60">
5     <define name="z_start" value="-0.0526"/>
6     <define name="z_end" value="0.0800"/>
7     <define name="radius_start" value="0.1096"/>
8     <define name="radius_end" value="0.1059"/>
9     <define name="theta_start" value="15."/>
10    <define name="theta_end" value="0."/>
11    <define name="mesh" value="100"/>
12    <loop variable="i" start="0" end="[mesh]" step="1">
13      <start_line x1="{[radius_start]*cos(2.*TMath::Pi()*[i]/[mesh])}" y1="{[
        radius_start]*cos([theta_start]/180.*TMath::Pi())*sin(2.*TMath::Pi()*[i]/[
        mesh])}" z1="{[radius_start]*sin([theta_start]/180.*TMath::Pi())*sin(2.*
        TMath::Pi()*[i]/[mesh])+[z_start]}" x2="{[radius_start]*cos(2.*TMath::Pi
        ())*([i]+1)_mod_[mesh])/[mesh]}" y2="{[radius_start]*cos([theta_start
        ]/180.*TMath::Pi())*sin(2.*TMath::Pi()*([i]+1)_mod_[mesh])/[mesh]}" z2
        ="{[radius_start]*sin([theta_start]/180.*TMath::Pi())*sin(2.*TMath::Pi()
        *([i]+1)_mod_[mesh])/[mesh])+[z_start]}/>
14      <end_line x1="{[radius_end]*cos(2.*TMath::Pi()*[i]/[mesh])}" y1="{[
        radius_end]*cos([theta_end]/180.*TMath::Pi())*sin(2.*TMath::Pi()*[i]/[
        mesh])}" z1="{[radius_end]*sin([theta_end]/180.*TMath::Pi())*sin(2.*
        TMath::Pi()*[i]/[mesh])+[z_end]}" x2="{[radius_end]*cos(2.*TMath::Pi()
        *([i]+1)_mod_[mesh])/[mesh]}" y2="{[radius_end]*cos([theta_end
        ]/180.*TMath::Pi())*sin(2.*TMath::Pi()*([i]+1)_mod_[mesh])/[mesh]}" z2
        ="{[radius_end]*sin([theta_end]/180.*TMath::Pi())*sin(2.*TMath::Pi()*([
        i]+1)_mod_[mesh])/[mesh])+[z_end]}/>
15    </loop>
16  </beam>
17 </beam_surface>

```

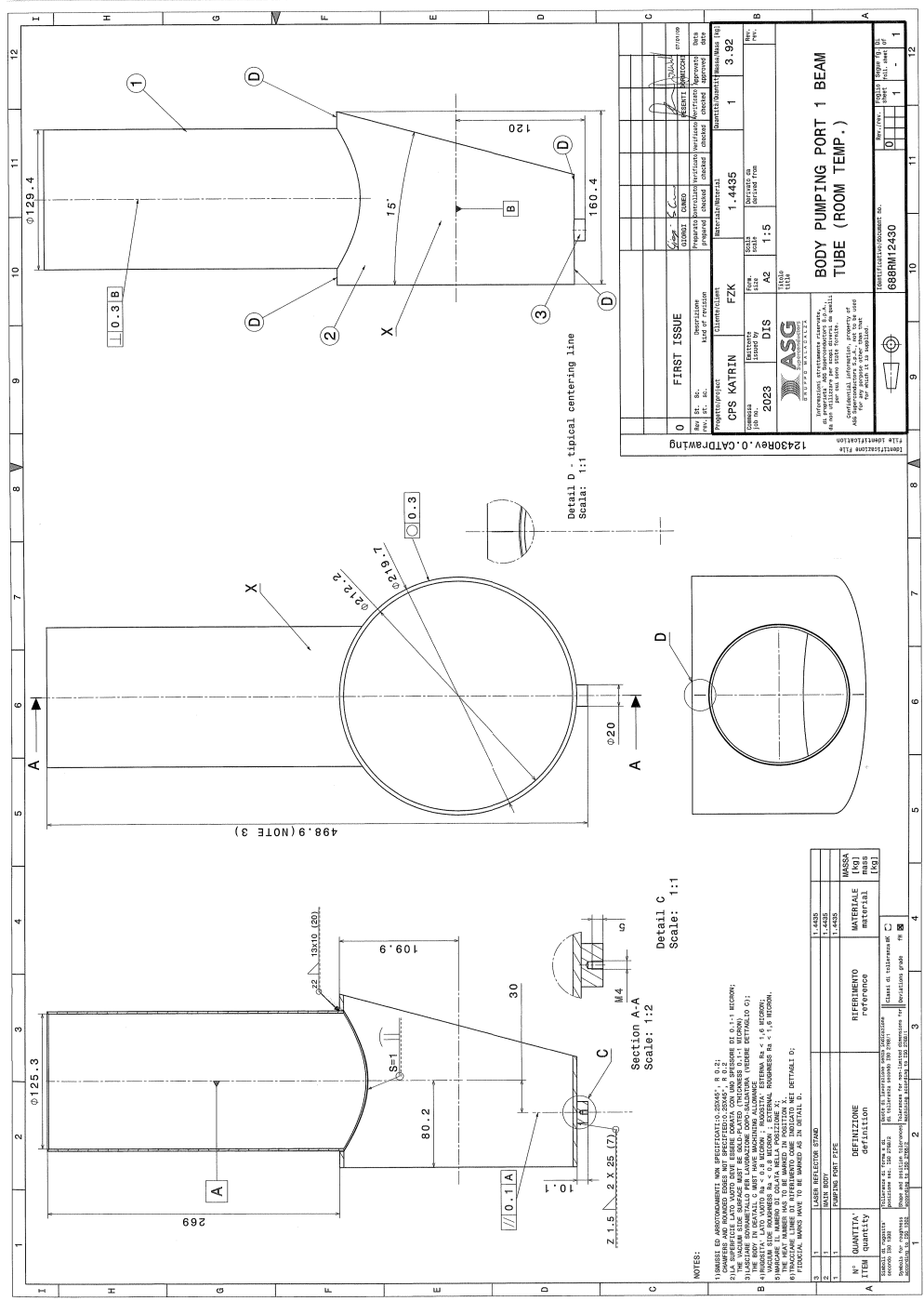


Figure B.4.: Drawing 688RM12430 corresponding to the first CPS pump port

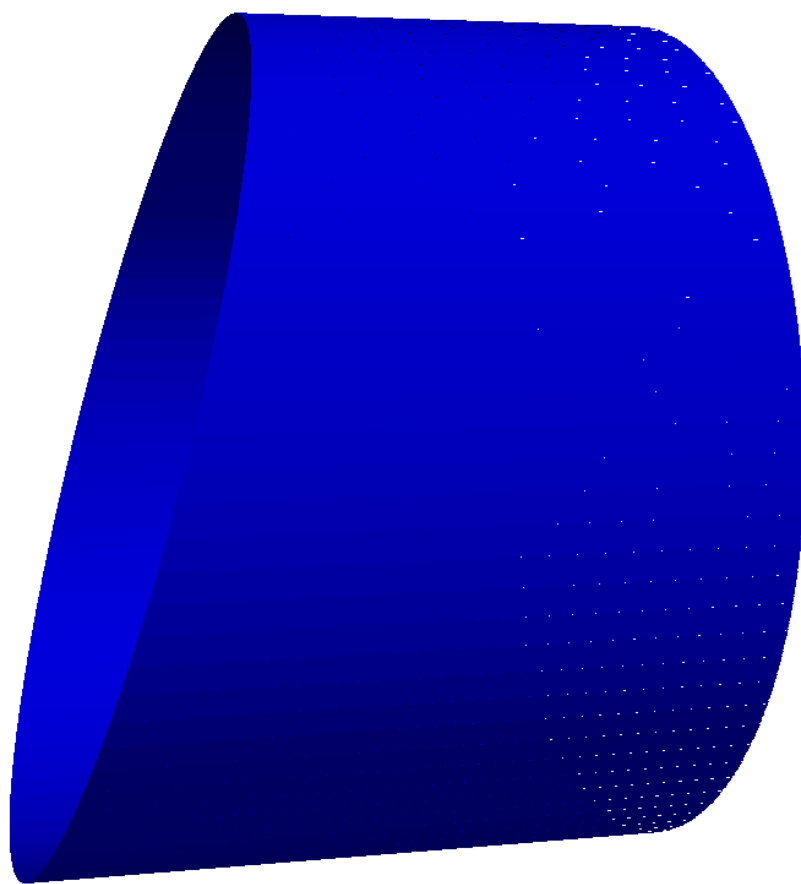


Figure B.5.: 3D Geometry of the first pump port

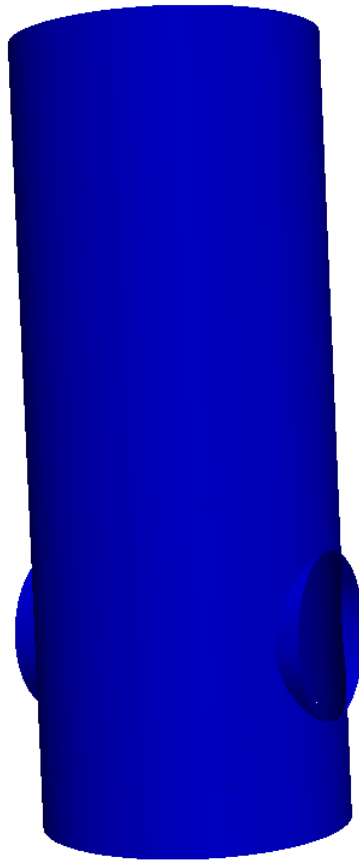


Figure B.6.: 3D Geometry of the second pump port

B.4. Second pump port

```
1 <!--Code corresponding to drawing 688RM12491-->
2
3 <port_housing_surface name="pump_port_surface">
4   <port_housing x1="0." y1="0." z1="-0.1554" x2="0." y2="0." z2="0.4886"
      radius="0.1276" longitudinal_mesh_count="50" axial_mesh_count="50"
      ">
5   <circular_port x=".1276" y="0" z="0" radius="0.0676"/>
6   <circular_port x="-0.1276" y="0" z="0" radius="0.0676"/>
7 </port_housing>
8 </port_housing_surface>
```


Figure B.7.: Drawing 688RM12491 corresponding to the second CPS pump port

B.5. CPS beamtube

```

1 <!--Code corresponding to drawing 688RM12422
2
3 <beam_surface name="beamtube_3_begin">
4   <beam longitudinal_mesh_count="60" axial_mesh_count="60">
5     <define name="z_start_2" value="-0.0397"/>
6     <define name="z_end_2" value="0.033"/>
7     <define name="radius_start_2" value="0.0646"/>
8     <define name="radius_end_2" value="0.0643"/>
9     <define name="theta_start_2" value="6."/>
10    <define name="theta_end_2" value="0"/>
11    <define name="mesh_2" value="100"/>
12    <loop variable="i" start="0" end="[mesh_2]" step="1">
13      <start_line x1="{[radius_start_2]*cos(2.*TMath::Pi()*[i]/[mesh_2])}" y1=
        "{[radius_start_2]*cos([theta_start_2]/180.*TMath::Pi())*sin(2.*
        TMath::Pi()*[i]/[mesh_2])}" z1="{[radius_start_2]*sin([theta_start_2
        ]/180.*TMath::Pi())*sin(2.*TMath::Pi()*[i]/[mesh_2])+[z_start_2]}" x2="{[
        radius_start_2]*cos(2.*TMath::Pi()*([i]+1)_mod_[mesh_2])/[mesh_2]}"
        y2="{[radius_start_2]*cos([theta_start_2]/180.*TMath::Pi())*sin(2.*
        TMath::Pi()*([i]+1)_mod_[mesh_2])/[mesh_2]}" z2="{[radius_start_2]*
        sin([theta_start_2]/180.*TMath::Pi())*sin(2.*TMath::Pi()*([i]+1)_mod_[
        mesh_2])/[mesh_2])+[z_start_2]}"/>
14      <end_line x1="{[radius_end_2]*cos(2.*TMath::Pi()*[i]/[mesh_2])}" y1="
        {[radius_end_2]*cos([theta_end_2]/180.*TMath::Pi())*sin(2.*TMath::Pi()
        *[i]/[mesh_2])}" z1="{[radius_end_2]*sin([theta_end_2]/180.*TMath::Pi
        ())*sin(2.*TMath::Pi()*[i]/[mesh_2])+[z_end_2]}" x2="{[radius_end_2]*
        cos(2.*TMath::Pi()*([i]+1)_mod_[mesh_2])/[mesh_2]}" y2="{[
        radius_end_2]*cos([theta_end_2]/180.*TMath::Pi())*sin(2.*TMath::Pi()
        *([i]+1)_mod_[mesh_2])/[mesh_2]}" z2="{[radius_end_2]*sin([
        theta_end_2]/180.*TMath::Pi())*sin(2.*TMath::Pi()*([i]+1)_mod_[mesh_2
        ])/[mesh_2])+[z_end_2]}"/>
15    </loop>
16  </beam>
17 </beam_surface>
18
19 <rotated_poly_loop_surface name="beam_tube_3and4_surface"
    rotated_mesh_count="64">
20   <poly_loop>
21     <start_point x="-0.4475" y="0.0667"/>
22     <next_line x="-0.4455" y="0.0667"/>
23     <next_line x="-0.4455" y="0.0628"/>
24     <next_line x="-0.4445" y="0.0628"/>
25     <next_line x="-0.4445" y="0.0613"/>

```

```

26 <next_line x="-0.4425" y="0.0613"/>
27 <next_line x="-0.4425" y="0.0628"/>
28 <next_line x="-0.4415" y="0.0628"/>
29 <next_line x="-0.4415" y="0.0681"/>
30 <next_line x="-0.3479" y="0.0681"/>
31 <next_line x="-0.3479" y="0.0628"/>
32 <next_line x="-0.3478" y="0.0628"/>
33 <next_line x="-0.3478" y="0.0608"/>
34 <next_line x="-0.3438" y="0.0608"/>
35 <next_line x="-0.3438" y="0.0628"/>
36 <next_line x="-0.3428" y="0.0628"/>
37 <next_line x="-0.3428" y="0.050"/>
38 <next_line x="-0.0" y="0.050"/>
39 <next_line x="0.3555" y="0.050"/>
40 <next_line x="0.3555" y="0.049"/>
41 <next_line x="0.3595" y="0.049"/>
42 <next_line x="0.3595" y="0.0475"/>
43 <next_line x="0.3565" y="0.0475"/>
44 <next_line x="0.3565" y="0.0413"/>
45 <next_line x="0.1565" y="0.0375"/>
46 <next_line x="0.0" y="0.0375"/>
47 <next_line x="-0.1496" y="0.0375"/>
48 <next_line x="-0.3495" y="0.0413"/>
49 <next_line x="-0.3495" y="0.0475"/>
50 <next_line x="-0.3575" y="0.0475"/>
51 <next_line x="-0.3575" y="0.050"/>
52 <next_line x="-0.3488" y="0.050"/>
53 <next_line x="-0.3488" y="0.0548"/>
54 <next_line x="-0.4415" y="0.0548"/>
55 <next_line x="-0.4415" y="0.0618"/>
56 <next_line x="-0.4422" y="0.0598"/>
57 <next_line x="-0.4475" y="0.0598"/>
58 <last_line/>
59 </poly_loop>
60 </rotated_poly_loop_surface>
61
62 <beam_surface name="beamtube_3_end">
63 <beam longitudinal_mesh_count="60" axial_mesh_count="60">
64 <define name="z_start_3" value="-0.0865"/>
65 <define name="z_end_3" value="0.0939"/>
66 <define name="radius_start_3" value="0.0659"/>
67 <define name="radius_end_3" value="0.0476"/>
68 <define name="theta_start_3" value="7.5"/>
69 <define name="theta_end_3" value="-1.5"/>
70 <define name="mesh_3" value="100"/>

```

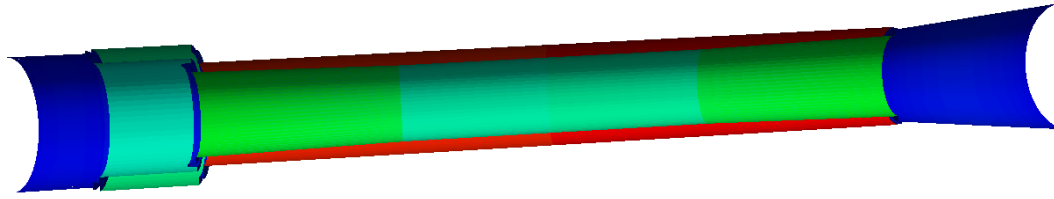


Figure B.8.: Cut of the 3D Geometry of a CPS beamtube

```

71 <loop variable="i" start="0" end="[mesh_3]" step="1">
72 <start_line x1="{[radius_start_3]*cos(2.*TMath::Pi()*[i]/[mesh_3])}" y1=
    "{[radius_start_3]*cos([theta_start_3]/180.*TMath::Pi())*sin(2.*
    TMath::Pi()*[i]/[mesh_3])}" z1="{[radius_start_3]*sin([theta_start_3
    ]/180.*TMath::Pi())*sin(2.*TMath::Pi()*[i]/[mesh_3])+[z_start_3]}" x2="{[
    radius_start_3]*cos(2.*TMath::Pi()*([i]+1)_mod_[mesh_3])/[mesh_3]}"
    y2="{[radius_start_3]*cos([theta_start_3]/180.*TMath::Pi())*sin(2.*
    TMath::Pi()*([i]+1)_mod_[mesh_3])/[mesh_3]}" z2="{[radius_start_3]*
    sin([theta_start_3]/180.*TMath::Pi())*sin(2.*TMath::Pi()*([i]+1)_mod_[
    mesh_3])/[mesh_3])+[z_start_3]}/>
73 <end_line x1="{[radius_end_3]*cos(2.*TMath::Pi()*[i]/[mesh_3])}" y1="
    {[radius_end_3]*cos([theta_end_3]/180.*TMath::Pi())*sin(2.*TMath::Pi()
    *[i]/[mesh_3])}" z1="{[radius_end_3]*sin([theta_end_3]/180.*TMath::Pi
    ())*sin(2.*TMath::Pi()*[i]/[mesh_3])+[z_end_3]}" x2="{[radius_end_3]*
    cos(2.*TMath::Pi()*([i]+1)_mod_[mesh_3])/[mesh_3]}" y2="{[
    radius_end_3]*cos([theta_end_3]/180.*TMath::Pi())*sin(2.*TMath::Pi()
    *([i]+1)_mod_[mesh_3])/[mesh_3]}" z2="{[radius_end_3]*sin([
    theta_end_3]/180.*TMath::Pi())*sin(2.*TMath::Pi()*([i]+1)_mod_[mesh_3
    ])/[mesh_3])+[z_end_3]}/>
74 </loop>
75 </beam>
76 </beam_surface>

```

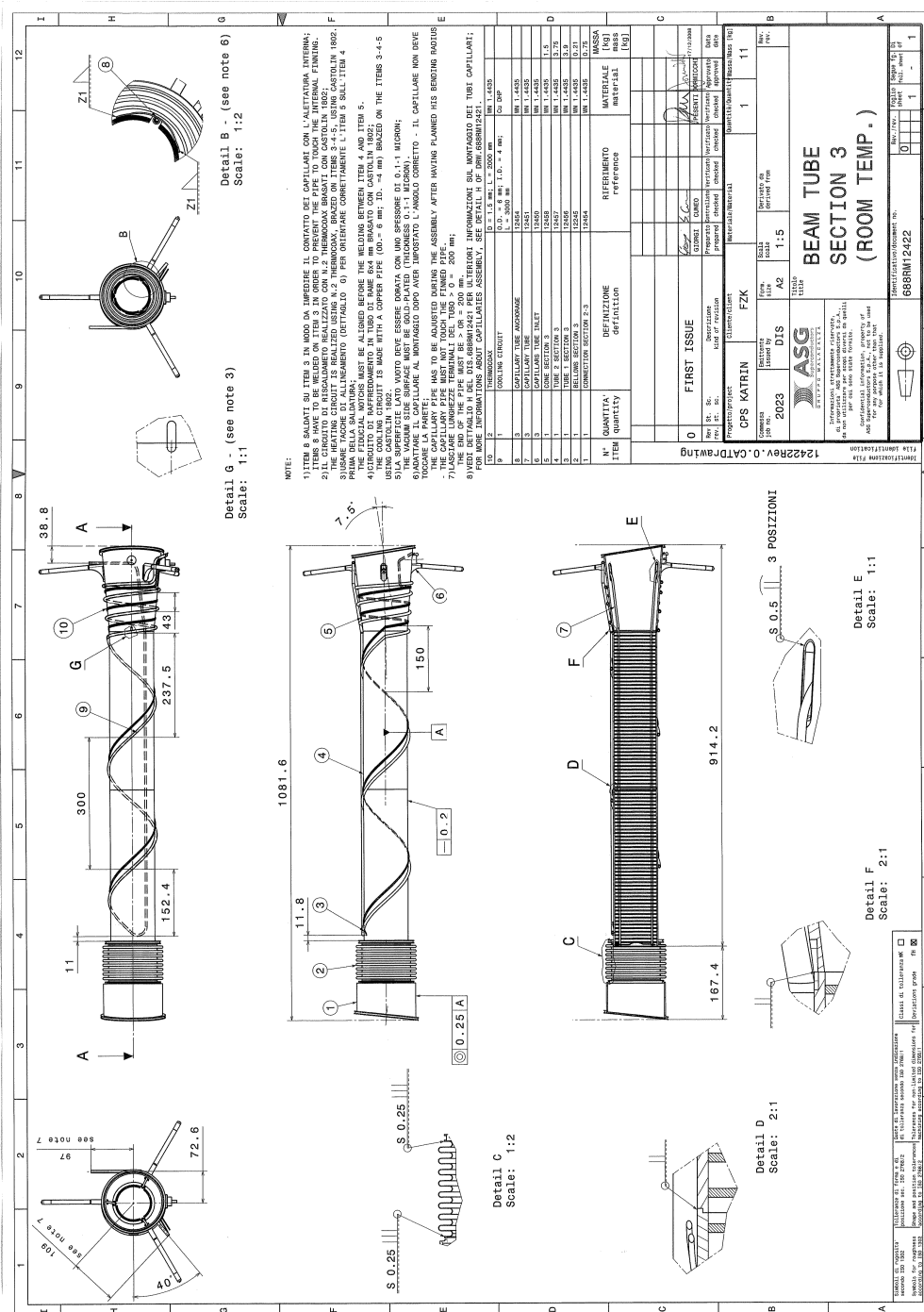


Figure B.9.: Drawing 688RM12422 corresponding to a CPS beamtube

B.6. CPS DPS Flange

```
1 <!--Code corresponding to drawing 688RM12427
2
3 <rotated_poly_loop_surface name="DPS_flange_surface"
   rotated_mesh_count="64">
4   <poly_loop>
5     <start_point x="0." y="0.1517"/>
6     <next_line x="0.01" y="0.1517"/>
7     <next_line x="0.01" y="0.1763"/>
8     <next_line x="0.014" y="0.1763"/>
9     <next_line x="0.014" y="0.1824"/>
10    <next_line x="0.01" y="0.1824"/>
11    <next_line x="0.01" y="0.1886"/>
12    <next_line x="0.0249" y="0.1886"/>
13    <next_line x="0.0249" y="0.0955"/>
14    <next_line x="0.012" y="0.0955"/>
15    <next_line x="0.012" y="0.0965"/>
16    <next_line x="0.0145" y="0.0965"/>
17    <next_line x="0.0145" y="0.0995"/>
18    <next_line x="0.012" y="0.0995"/>
19    <next_line x="0.012" y="0.1236"/>
20    <next_line x="0.0021" y="0.1236"/>
21    <next_line x="0.0021" y="0.1334"/>
22    <next_line x="0.0013" y="0.1334"/>
23    <next_line x="0.0013" y="0.136"/>
24    <next_line x="0." y="0.136"/>
25    <last_line/>
26  </poly_loop>
27 </rotated_poly_loop_surface>
```

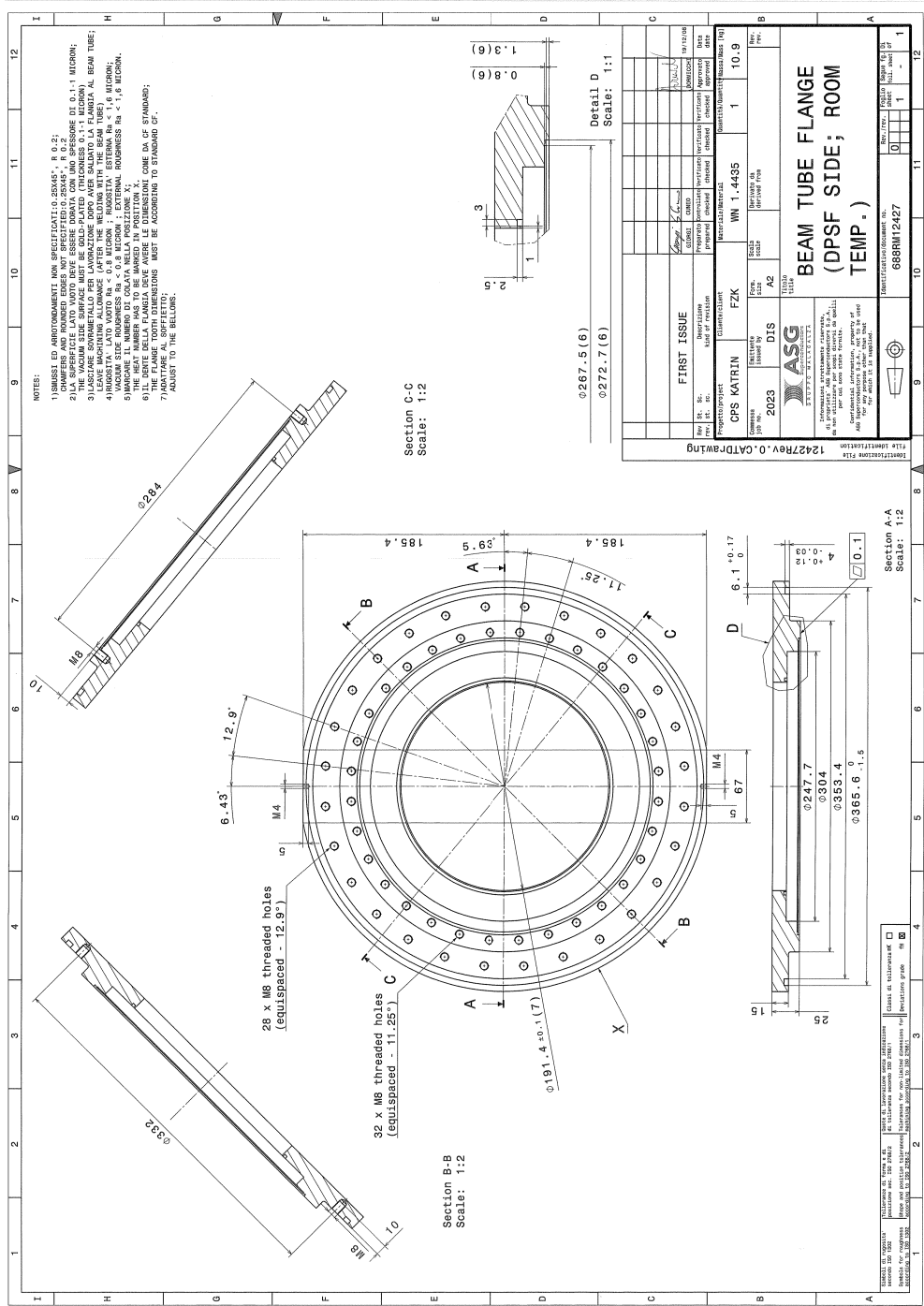


Figure B.10.: Drawing 688RM12427 corresponding to the CPS DPS flange

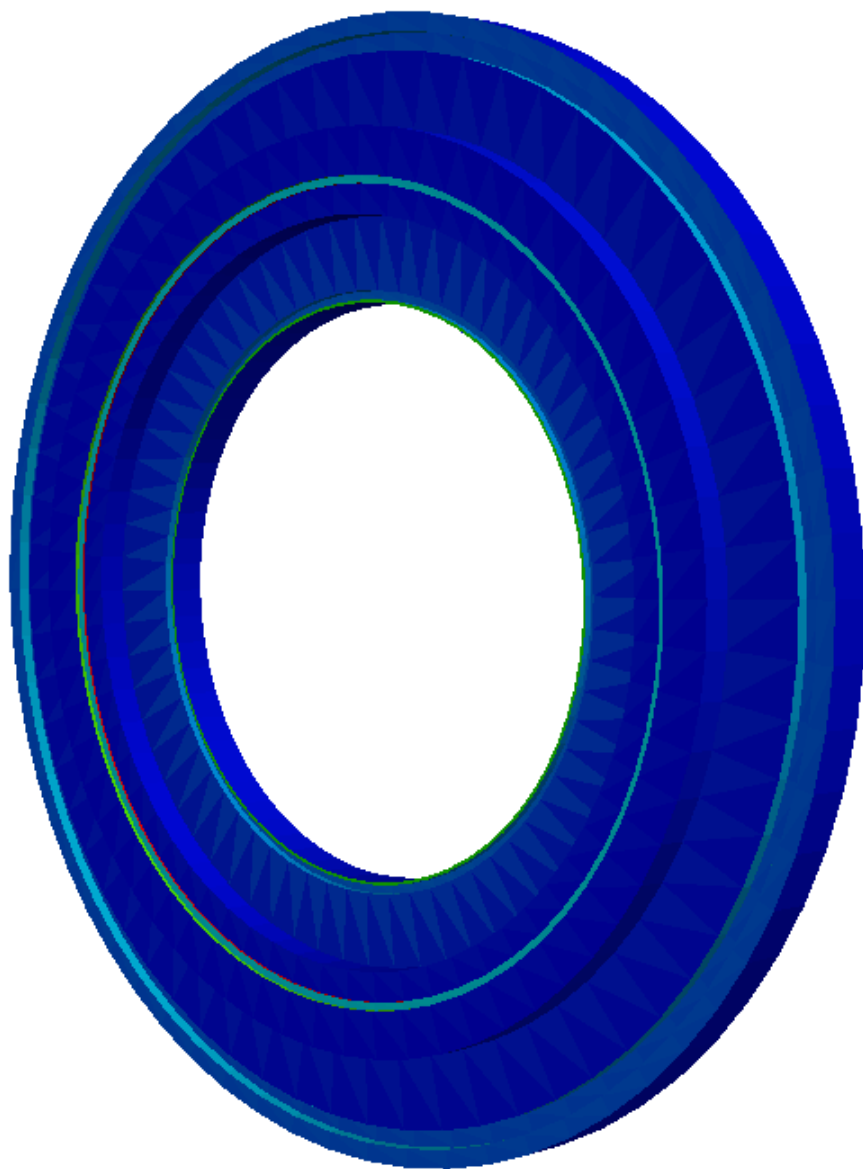


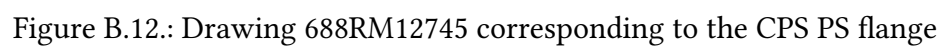
Figure B.11.: 3D Drawing of the CPS DPS flange

B.7. CPS PS Flange

```

1 <!--Code corresponding to drawing 688RM12745
2
3 <rotated_poly_loop_surface name="PS_flange">
4   <poly_loop>
5     <start_point x="-0.0643" y="0.175"/>
6     <next_line x="-0.0493" y="0.175"/>
7     <next_line x="-0.0493" y="0.1701"/>
8     <next_line x="-0.0533" y="0.1701"/>
9     <next_line x="-0.0533" y="0.164"/>
10    <next_line x="-0.0493" y="0.164"/>
11    <next_line x="-0.0493" y="0.106"/>
12    <next_line x="-0.0543" y="0.106"/>
13    <next_line x="-0.0543" y="0.105"/>
14    <next_line x="-0.0493" y="0.105"/>
15    <next_line x="0.0437" y="0.105"/>
16    <next_line x="0.0437" y="0.1266"/>
17    <next_line x="0.0683" y="0.1266"/>
18    <next_line x="0.0683" y="0.10285"/>
19    <next_line x="0.0526" y="0.10285"/>
20    <next_line x="0.0526" y="0.103"/>
21    <next_line x="-0.0543" y="0.103"/>
22    <next_line x="-0.0543" y="0.0811"/>
23    <next_line x="-0.0575" y="0.0811"/>
24    <next_line x="-0.0593" y="0.08425"/>
25    <next_line x="-0.0643" y="0.08425"/>
26    <last_line/>
27  </poly_loop>
28 </rotated_poly_loop_surface>

```



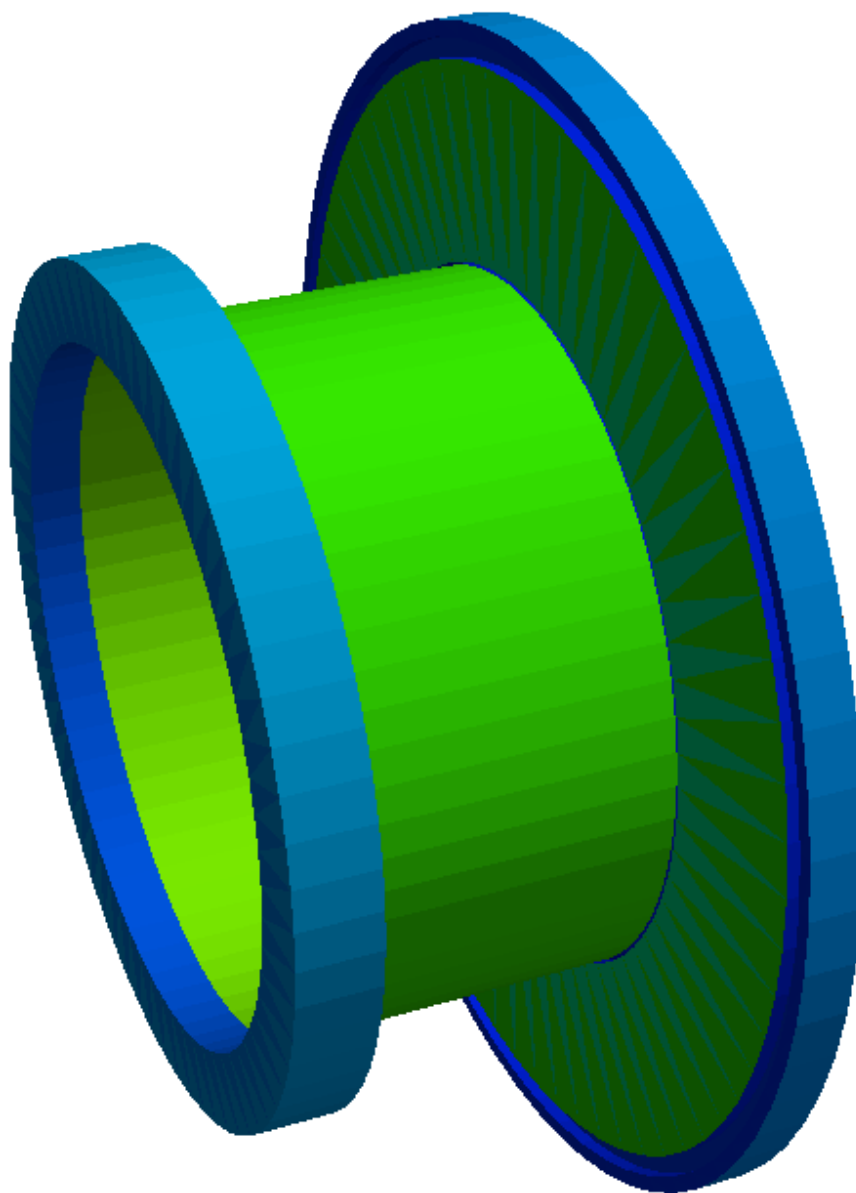


Figure B.13.: 3D Drawing of the CPS PS flange

C. Electromagnetic configuration

Contents

| | |
|--|-----|
| C.1. Electric configuration of the DPS | 107 |
| C.2. Configuration of the magnets | 111 |

C.1. Electric configuration of the DPS

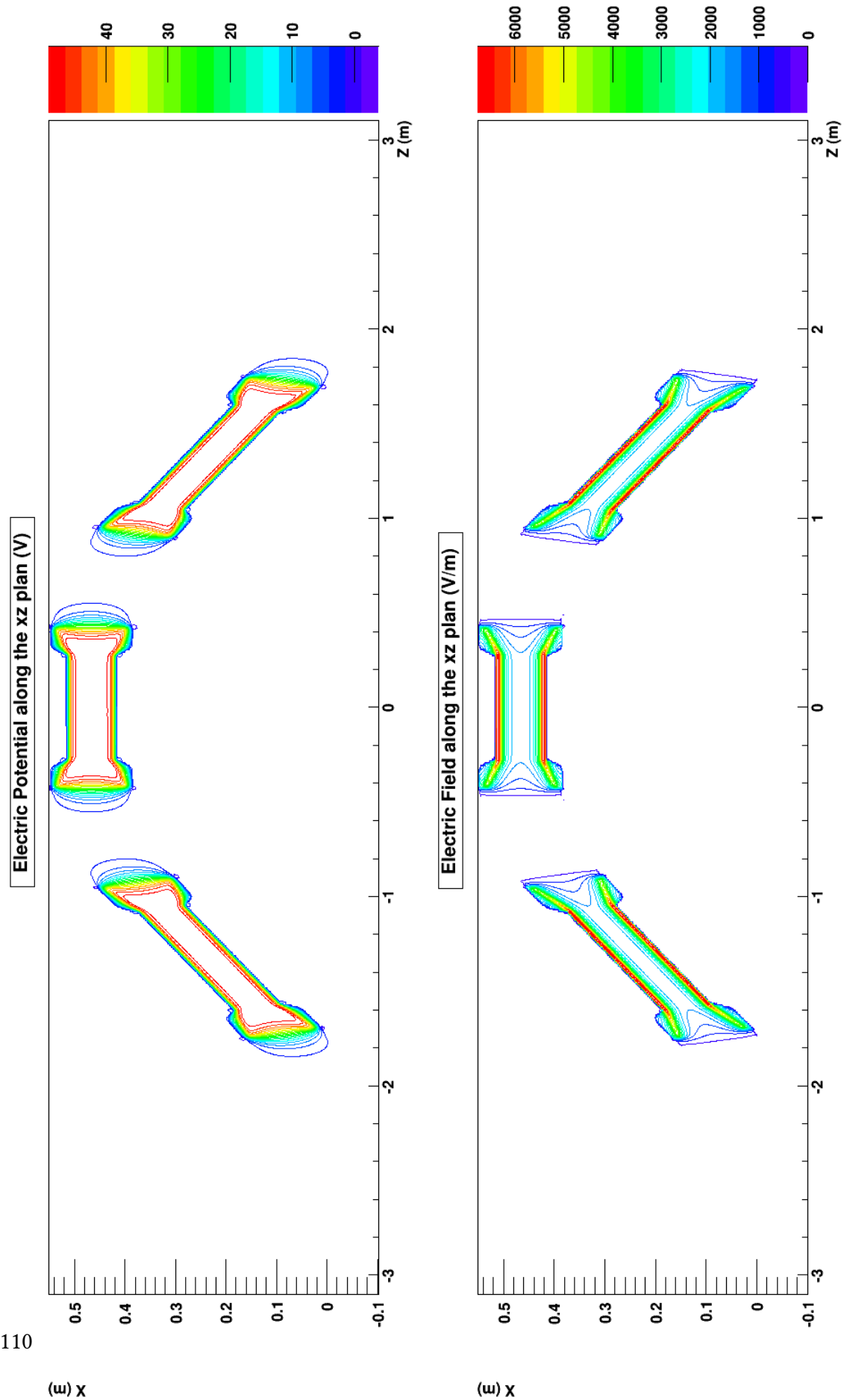
```
1 <!-- Electric configuration of the DPS -->
2
3 <!-- electric potential values -->
4 <define name="electrode_potential" value="-100."/>
5 <define name="beamtube_potential" value="0."/>
6 <define name="reflexion_potential" value="100."/>
7
8 <!-- electrodes -->
9 <loop variable="j" start="2" end="4" step="1">
10   <electrostatic_dirichlet
11     name="upper_electrode_[j]"
12     surfaces="DPS/upper_electrode_[j]"
13     value="{[electrode_potential]}"
14   />
15
16   <electrostatic_dirichlet
17     name="lower_electrode_[j]"
18     surfaces="DPS/lower_electrode_[j]"
19     value="{[beamtube_potential]}"
20   />
21 </loop>
22
23 <electrostatic_dirichlet
24   name="FT-ICR_1"
25   surfaces="DPS/FT-ICR_left/#"
26   value="{[beamtube_potential]}"
27 />
28
29 <electrostatic_dirichlet
```

```

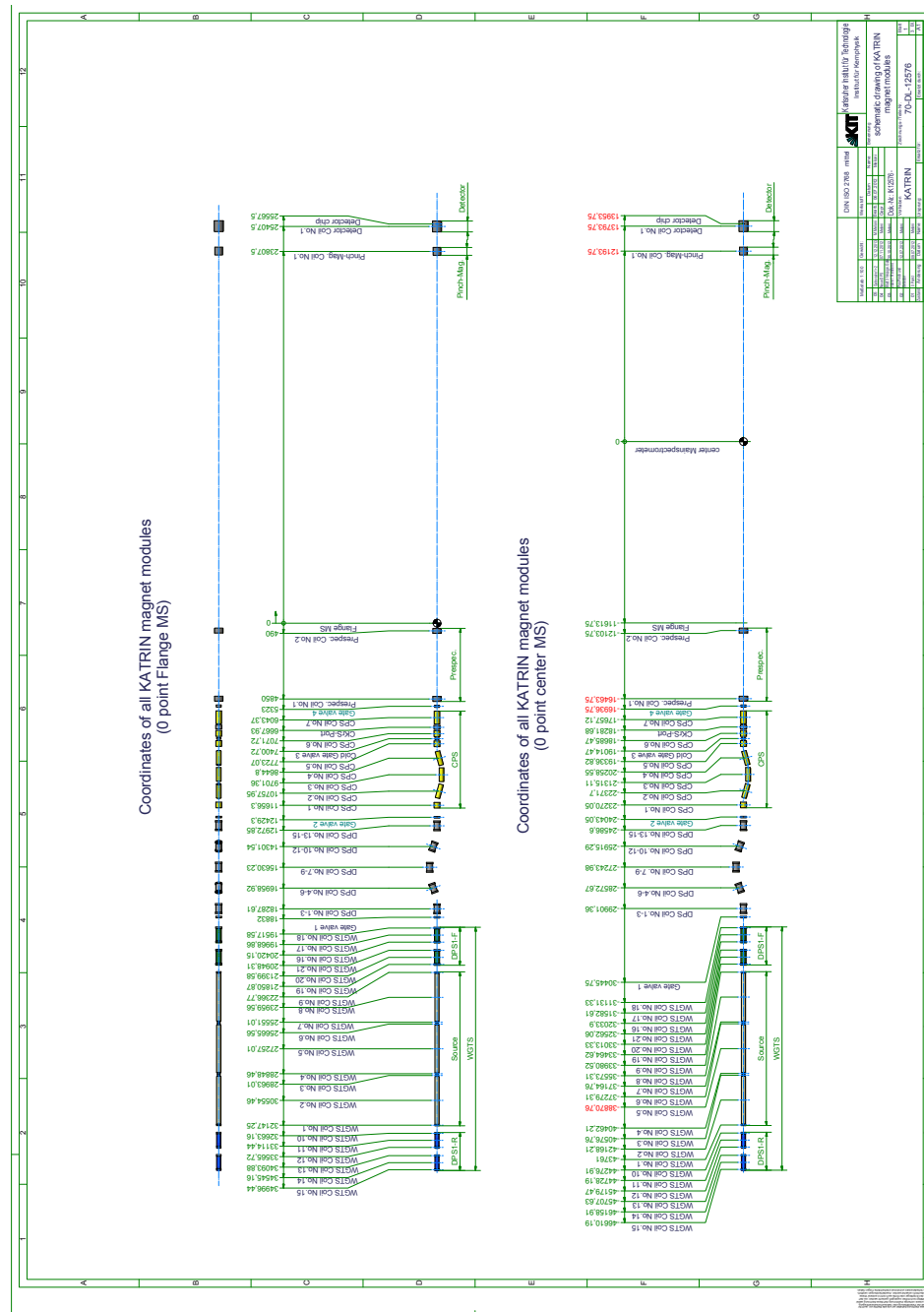
30  name="FT-ICR_2_tube"
31  surfaces="DPS/FT-ICR_right/FT-ICR_tube"
32  value="{[beamtube_potential]}"
33 />
34
35 <electrostatic_dirichlet
36  name="FT-ICR_2_entrance_electrode"
37  surfaces="DPS/FT-ICR_right/FT-ICR_entrance_electrode"
38  value="{[beamtube_potential]}"
39 />
40
41 <electrostatic_dirichlet
42  name="FT-ICR_2_middle_electrode"
43  surfaces="DPS/FT-ICR_right/FT-ICR_middle_electrode"
44  value="{[beamtube_potential]}"
45 />
46
47 <electrostatic_dirichlet
48  name="reflexion_electrode"
49  surfaces="DPS/FT-ICR_right/FT-ICR_end_electrode"
50  value="{[reflexion_potential]}"
51 />
52
53 <loop variable="i" start="1" end="5" step="1">
54
55  <electrostatic_dirichlet
56    name="beamtube[i]"
57    surfaces="DPS/beamtube_[i]"
58    value="{[beamtube_potential]}"
59  />
60
61 </loop>
62
63 <loop variable="j" start="2" end="4" step="1">
64
65  <electrostatic_dirichlet
66    name="pump_port_[j]"
67    surfaces="DPS/PP[j]_ext"
68    value="{[beamtube_potential]}"
69  />
70
71  <electrostatic_dirichlet
72    name="pump_port_[j]"
73    surfaces="DPS/PP[j]_in"
74    value="{[beamtube_potential]}"

```

```
75 />
76 </loop>
77
78 <electrostatic_dirichlet
79   name="pump_port_0"
80   surfaces="DPS/PP0/#"
81   value="{[beamtube_potential]}"
82 />
83
84 <electrostatic_dirichlet
85   name="pump_port_5"
86   surfaces="DPS/PP5/#"
87   value="{[beamtube_potential]}"
88 />
```



C.2. Configuration of the magnets



Acknowledgment

I would first like to thank Pr. Dr. Guido Drexlin for allowing me to do my internship at the great KATRIN experiment. Without him, I would not be writing this thesis.

Thank you to my two supervisors Kathrin Valerius and Daniel Hilk, whose French at the beginning, and knowledge and kindness along my whole internship helped me a lot to survive in Germany.

Thank you to the UFA/DFH for allowing me to participate to the double master program and financing me during this year.

Thank you to Judith Peters, Zahir Boulaamayl and Bernd Pilawa for helping me in the coordination of my double diploma in the two countries.

Thank you to Jan Oertling, Frank Bandeburg and Oliver Wack for having organized the Stammtisch; to Jan (again) for passing me the torch of the WAB; to Jan (still), Stefan Groh and Johannes Antoni for the pizze on Wednesday.

Thank you to Stefan Görhardt and Klaus Mehret for their cheerfulness.

Thank you to Jan Behrens, our student git sys-admin, and to Martin Babutzka, our local server admin, for keeping the network in order.

Thank you to all the IKP KATRIN students, post-docs and workers for helping me along this year in a foreign country.

Finally thank you to all the people involved in KATRIN in Germany and abroad for keeping the experiment progressing.

Bibliography

- [Ani05] I.V. Aničin : *The Neutrino - Its past, present and future*, arXiv:0503172
- [ASG14] ASG : *Attachment to TR MA140517 - AS BUILT MEASUREMENTS OF THE CM AFTER FLIPPING - rev4*, Internal communication
- [Bet39] H. A. Bethe : *Energy Production in Stars*, Phys. Rev. 55, 434 (1 March 1939)
- [BP34] H. Bethe & R. Peierls : *The Neutrino*, Nature 133, 689-690 (5 May 1934)
- [Cab67] N. Cabibbo : *Unitary Symmetry and Leptonic Decays*, Phys. Rev. Lett. 10, 531 (15 June 1963)
- [CGR99] H. Cheng, L. Greengard, and V. Rokhlin : *A Fast Adaptive Multipole Algorithm in Three Dimensions*, Journal of Computational Physics 155, 468498 (1999)
- [Cor14] T.J. Corona : *Methodology and Application of High Performance Electrostatic Field Simulation in the KATRIN Experiment*, PhD Thesis, University of North Carolina at Chapel Hill, 2014
- [CR+56] Cowan Jr., Reines, Harrison, Kruse and McGuire (1956): *Detection of the Free Neutrino: a Confirmation*, Science 124 (3212): 1034
- [DG+62] G. Danby, J-M. Gaillard, K Goulianos, L. M. Lederman, N. Mistry, M. Schwartz and Z. Steinbergert *Observation of high-energy neutrino reactions and the existence of two kinds of neutrinos*, Phys. Rev. Lett. 9, 36, 1 July 1962
- [Fer34] E. Fermi : *Versuch einer Theorie der β -Strahlen*, Zeitschrift für Physik A 88 (34): 161
- [FL*12] Formaggio, Lazič, Corona, Štefančić, Abraham and Glück : *Solving for micro- and macro-scale electro-static configurations using the robin hood algorithm*, Progress In Electromagnetics Research B, Vol. 39, 1-37, 2012
- [Gar74] The Gargamelle collaboration : *Observation of neutrino-like interactions without muon or electron in the Gargamelle neutrino experiment*, Nuclear Physics B Volume 73, Issue 1, 25 April 1974, Pages 1-22
- [GdP+13] E. Giusarma, R. de Putter, S. Ho and O. Mena : *Constraints on neutrino masses from Planck and Galaxy clustering data*, Physical Review D 88, 063515 (2013)
- [GER13] The GERDA Collaboration : *Results on neutrinoless double beta decay of ^{76}Ge from Gerda Phase I*, Phys. Rev. Lett 111 (2013) 122503

- [GH+94] Gamma, Helm, Johnson and Vlissides : *Design Patterns: Elements of Reusable Object-Oriented Software*, Addison-Wesley Professional (1994)
- [Glü11] F. Glück : *Axisymmetric magnetic field calculation with zonal harmonic expansion*, Progress In Electromagnetics Research B, Vol. 32, 351-388, 2011
- [Int] Internal communication
- [Jan15] A. Jansen : *The Cryogenic Pumping Section of the KATRIN Experiment - Design Studies and Experiments for the Commissioning*, PhD Thesis, KIT, February 13, 2015
- [JS10] J. Sempere : *Euler Projection*, Wikimedia, 1 November 2010
- [KAT05] The KATRIN Collaboration : *KATRIN Design Report 2004*, Report NPI ASCR, Řež, EXP-01/2005, FZKA Scientific Report 7090, MS-KP-0501
- [KA14] The KATRIN Collaboration : *High-voltage monitoring with a solenoid retarding spectrometer at the KATRIN experiment*, 2014 JINST 9 P06022
- [KAT14] The KATRIN Collaboration : *Focal-plane detector system for the KATRIN experiment*, arXiv:1404.2925v1
- [KIT] www.katrin.kit.edu
- [KM53] E.J. Konopinski; H.M. Mahmoud : *The Universal Fermi Interaction*, Phys. Rev. 92 (1953) 1045
- [Kos12] A. Kosmider : *Tritium Retention Techniques in the KATRIN Transport Section and Commissioning of its DPS2-F Cryostat*, PhD Thesis, KIT, July 6, 2012
- [LSA06] P. Lazič, H. Štefančić, H. Abraham : *The Robin Hood method - A novel numerical method for electrostatic problems based on a non-local charge transfer*, Journal of Computational Physics 213 (2006) 117-140
- [LY57] T.D. Lee and C.N. Yang : *Question of Parity Conservation in Weak Interactions*, Phys. Rev. 104, 254 (1956)
- [Mai05] The Mainz Collaboration : *Final Results from phase II of the Mainz Neutrino Mass Search in Tritium β Decay*, Eur. Phys. J. C40: 447-468, 2005
- [Maj37] E. Majorana : *Symmetrical Theory of Electrons and Positrons* Nuovo Cim. 14 (1937) 171
- [MH12] M. Hötzel : *Simulation and analysis of source-related effects for KATRIN*, Dissertation, KIT, 2012
- [MNS62] Maki, Nakagawa and Sakata : *Remarks on the Unified Model of Elementary Particles*, Prog. Theor. Phys. (1962) 28 (5): 870-880
- [N13] Nagualdesign : *Wu experiment*, Wikimedia, 19 December 2013

- [NA37] S.H. Neddermeyer And C.D. Anderson : *Note on the Nature of Cosmic-Ray Particles*, Phys. Rev., Vol. 51, 884 (1937)
- [OLL04] E. T. Ong, K. H. Lee, and K. M. Lim : *A fast algorithm for three-dimensional electrostatics analysis: fast Fourier transform on multipoles (FFTM)*, Int. J. Numer. Meth. Engng 2004; 61:633656
- [PB05] D. Poljak and C. A. Brebbia : *Boundary Element Methods for Electrical Engineers*, WIT Press, January 2005.
- [Pon68] B. Pontecorvo : *Neutrino Experiments and the Problem of Conservation of Leptonic Charge*, ZhETF, Vol. 53, No. 5, p. 1717 (1968)
- [PRV10] G. Pagliaroli, F. Rossi-Torres, F. Vissani : *Neutrino mass bound in the standard scenario for supernova electronic antineutrino emission*, Astroparticle Physics 33 (2010) 287291
- [Rei09] S. Reimer : *Ein elektrostatisches Dipolsystem zur Eliminierung von Ionen in der DPS2-F des KATRIN Experimentes*, Diploma Thesis, KIT, November 2009
- [SC11] S. Cebrián : *Neutrinos: an introduction*, <http://www.scienceinschool.org>, 25 May 2011
- [Sch14] J. Schwartz : *The Detector System of the KATRIN Experiment - Implementation and First Measurements with the Spectrometer*, PhD Thesis, KIT, July 18, 2014
- [T2K13] T2K Collaboration : *New Results from the T2K Experiment : Observation of ν_e Appearance from a ν_μ Beam*, EPS Conference (2013)
- [TI53] S. Tanaka and M. Itô : *On the Natural Decay of the Free Neutron*, Progress of Theoretical Physics, Vol. 9. No.2, February 1953
- [Tro11] Aseev, Belesev, Berlev, Geraskin, Golubev, Likhovid, Lobashev, Nozik, Pantuev, Parfenov, Skasyrskaya, Tkachov, and Zadorozhny : *Upper limit on the electron antineutrino mass from the Troitsk experiment*, Phys. Rev. D 84, 112003 (2011)
- [Wei67] S. Weinberg : *A Model of Leptons*, Phys. Rev. Lett. 19, 1264 (20 November 1967)
- [Win11] A. Windberger : *Berechnungen und Simulationen zum Verhalten von Ionen in der differenziellen Pumpstrecke des KATRIN-Experiments*, Diploma Thesis, KIT, January 28, 2011
- [Yuk35] H. Yukawa : *On the Interaction of Elementary Particles*, Proc.Phys.Math.Soc.Jap. 17 (1935) 48